High resolution and high efficiency time-to-space conversion of ultrafast signals

Thesis submitted for the degree of "Doctor of Philosophy"

by

Dror Shayovitz

Submitted to the Senate of the Hebrew University of Jerusalem

September / 2014

High resolution and high efficiency time-to-space conversion of ultrafast signals

Thesis submitted for the degree of "Doctor of Philosophy"

by

Dror Shayovitz

Submitted to the Senate of the Hebrew University of Jerusalem

September / 2014

This work was carried out under the supervision of:

Dan M. Marom

This work is dedicated with love to my parents,

Sara and Mordechai.

For all their love, care and encouragement over the years…

Abstract

Ultrashort optical pulses are widely and increasingly used in many diverse fields of science and technology. By providing high temporal resolution they enable investigation and measurement of fundamental physical, chemical and biological phenomena that occur on picosecond time scales or shorter. In addition ultrashort pulses are an essential enabling tool for high speed optical communications and data processing technologies, as well as in advanced manufacturing and photomedicine applications. In all of these areas precise measurement and control of ultrashort optical pulses is vital - advances in ever shorter pulse generation must be accompanied by new methods to characterise and manipulate them.

This thesis presents work on the ongoing development of an ultrashort pulse measurement and manipulation technique known as time-to-space conversion. Time-to-space conversion uses sum-frequency generation between spectrally resolved ultrashort pulses to transfer information from the time domain to the space domain; in other words to create the real-time spatial image of an ultrashort pulse. Mapping the pulse temporal intensity envelope and phase onto a quasi-static spatial image allows high resolution measurement of these quantities, overcoming the difficulty of optoelectronic detection of ultrashort pulses directly in the time domain. Furthermore, the spectrally resolved nature of time-to-space conversion results in a large time window of operation. This enables a series of ultrashort pulses to be simultaneously transferred to spatially separated locations via interaction with a single reference pulse, thereby performing an all-optical demultiplexing operation.

The two main developments introduced in this thesis are: a) greater feasibility of time-to-space conversion for all-optical demultiplexing of a high speed optical communications channel by demonstrating the technique in a planar nonlinear waveguide and b) the demonstration of full-field characterisation of ultrashort pulses by using interferometric detection after the time-to-space conversion. The practicality of time-to-space conversion for all-optical demultiplexing depends on minimising its optical power consumption. This can be achieved by implementation of the conversion process in the guided-wave regime, as opposed to the free-space regime in which it has previously been demonstrated. The first three papers presented in this thesis describe the preliminary steps towards this goal, namely the demonstration of

non wavelength-degenerate and background-free collinearly phase-matched time-to-space conversion and the demonstration of time-to-space conversion in a planar nonlinear waveguide. Full-field characterisation of ultrashort pulses by time-to-space conversion is enabled by the quasi-monochromaticity of the output sum-frequency signal, a feature which follows from the unique geometry of the oppositely dispersed waves of the pulse to be measured and the reference pulse. The quasi-monochromatic converted signal can be mixed with a narrow linewidth local oscillator for interferometric measurement of the ultrashort pulse field amplitude and phase. The final two papers included here describe the first time demonstration of full-field measurement of bandwidth-limited and chirped pulses by time-to-space conversion and of single-shot coherent detection of a phase modulated ultrashort pulse train. Taken together, the work presented in this thesis has achieved an increase in the utility of time-to-space conversion as an ultrashort optical pulse measurement and manipulation technique, with potential applications in optical communications and data processing and in the field of ultrashort pulse measurement.

Acknowledgments

First and foremost I would like to thank Professor Dan Marom, my supervisor, for his guidance, help and encouragement from the start to the finish. Over the course of this project I have benefited enormously both from his technical advice on the various diverse areas of optics which this research has touched and also, more importantly, from his constant interest and support. His professional ability and knowledge is matched only by his enthusiasm and readiness to help. I have learnt a great deal from him and consider myself very fortunate to have been his student.

I would also like to acknowledge and thank all the students at our lab that I have worked with and whose company I have enjoyed over the years:

David, Yaron, Yoram, Asael, Yoni, Amitay, Yiska, Moran, Yedidya, Miri, Noam, Ori, Leonid, Roy, Yisrael and Avishag.

It was a pleasure to be a part of this warm and supportive group where discussions, advice and mutual assistance are a daily occurrence. I have learnt something from each one (and many things from David). Thanks also to Noam Meyuhas for helping to build the PPLN crystal temperature control. I would also like to thank my collaborators at the University of Paderborn in Germany, in particular Harald Herrmann and Wolfgang Sohler, for providing the PPLN crystals used in part of these experiments and especially for the fruitful discussions and helpful guidance.

Finally I would like to dedicate this thesis to my parents, Motti and Sara, since it is only thanks to them and their love and encouragement that I arrived at the start of this project and also reached the end.

Letter concerning joint authorship of articles

This thesis contains four peer-reviewed papers published in academic journals and one paper which has been submitted for publication at the time of presentation of this thesis. This document specifies the contributions of the listed authors[1] for each paper, where the primary author in all of them was Dror Shayovitz.

Chapter 2A: D. Shayovitz and D. M. Marom, "High-resolution, background-free, time-to-space conversion by collinearly phase-matched sum-frequency generation," Opt. Lett. **36**, 1957-1959 (2011).

Additional author: Dan M. Marom

Chapter 2B: D. Shayovitz, H. Herrman, W. Sohler, R. Ricken, C. Silberhorn and D. M. Marom, "High resolution time-to-space conversion of sub-picosecond pulses at 1.55μm by non-degenerate SFG in PPLN crystal," Opt. Exp. **24**, 27388-27395 (2012).

Primary author: Dror Shayovitz

Contribution: designing and building the optical setup, performing all the measurements and writing the article.

1st additional author: Harald Herrmann, Department of Applied Physics, University of Paderborn, Germany.

Contribution: design and fabrication of the PPLN nonlinear crystal used in the experiment.

2nd additional author: Wolfgang Sohler, Department of Applied Physics, University of Paderborn, Germany.

Contribution: design and fabrication of the PPLN nonlinear crystal used in the experiment.

3rd additional author: Raimund Ricken, Department of Applied Physics, University of Paderborn, Germany.

Contribution: fabrication of the PPLN nonlinear crystal used in the experiment.

4th additional author: Christine Silberhorn, Department of Applied Physics, University of Paderborn, Germany.

Contribution: design and fabrication of the PPLN nonlinear crystal used in the experiment.

5th additional author: Dan M. Marom, Department of Applied Physics, Hebrew University of Jerusalem, Israel.

Chapter 3A: D. Shayovitz, H. Herrman, W. Sohler, R. Ricken, C. Silberhorn and D. M. Marom, "Time-to-space conversion of ultrafast waveforms at 1.55 μm in a planar periodically poled lithium niobate waveguide," Opt. Lett. **38**, 4708-4711 (2013).

Primary author: Dror Shayovitz

[1] Except for Prof. Dan M. Marom who is the final listed author on all papers and who was the supervisor for this PhD project.

Contribution: designing and building the optical setup, performing all the measurements and writing the article.

1st additional author: Harald Herrmann, Department of Applied Physics, University of Paderborn, Germany.

Contribution: design and fabrication of the PPLN nonlinear crystal waveguide used in the experiment.

2nd additional author: Wolfgang Sohler, Department of Applied Physics, University of Paderborn, Germany.

Contribution: design and fabrication of the PPLN nonlinear crystal waveguide used in the experiment.

3rd additional author: Raimund Ricken, Department of Applied Physics, University of Paderborn, Germany.

Contribution: fabrication of the PPLN nonlinear crystal waveguide used in the experiment.

4th additional author: Christine Silberhorn, Department of Applied Physics, University of Paderborn, Germany.

Contribution: design and fabrication of the PPLN nonlinear crystal waveguide used in the experiment.

5th additional author: Dan M. Marom, Department of Applied Physics, Hebrew University of Jerusalem, Israel.

Chapter 4A: D. Shayovitz, H. Herrman, W. Sohler, R. Ricken, C. Silberhorn and D. M. Marom, "Full-field reconstruction of ultrashort waveforms by time to space conversion interferogram analysis," Opt. Exp. **22**, 20205-20213 (2014).

Primary author: Dror Shayovitz

Contribution: designing and building the optical setup, performing all the measurements and writing the article.

1st additional author: Harald Herrmann, Department of Applied Physics, University of Paderborn, Germany.

Contribution: design and fabrication of the PPLN nonlinear crystal used in the experiment.

2nd additional author: Wolfgang Sohler, Department of Applied Physics, University of Paderborn, Germany.

Contribution: design and fabrication of the PPLN nonlinear crystal used in the experiment.

3rd additional author: Raimund Ricken, Department of Applied Physics, University of Paderborn, Germany.

Contribution: fabrication of the PPLN nonlinear crystal used in the experiment.

4th additional author: Christine Silberhorn, Department of Applied Physics, University of Paderborn, Germany.

Contribution: design and fabrication of the PPLN nonlinear crystal used in the experiment.

5th additional author: Dan M. Marom, Department of Applied Physics, Hebrew University of Jerusalem, Israel.

<u>Chapter 4B:</u> D. Shayovitz, H. Herrman, W. Sohler, R. Ricken, C. Silberhorn and D. M. Marom, "Real-time coherent detection of ultrashort pulses after time-to-space conversion and spatial demultiplexing," (not published).

Primary author: Dror Shayovitz

Contribution: designing and building the optical setup, performing all the measurements and writing the article.

1st additional author: Harald Herrmann, Department of Applied Physics, University of Paderborn, Germany.

Contribution: design and fabrication of the PPLN nonlinear crystal used in the experiment.

2nd additional author: Wolfgang Sohler, Department of Applied Physics, University of Paderborn, Germany.

Contribution: design and fabrication of the PPLN nonlinear crystal used in the experiment.

3rd additional author: Raimund Ricken, Department of Applied Physics, University of Paderborn, Germany.

Contribution: fabrication of the PPLN nonlinear crystal used in the experiment.

4th additional author: Christine Silberhorn, Department of Applied Physics, University of Paderborn, Germany.

Contribution: design and fabrication of the PPLN nonlinear crystal used in the experiment.

5th additional author: Dan M. Marom, Department of Applied Physics, Hebrew University of Jerusalem, Israel.

Contents

List of figures

List of publications

1. D. Shayovitz and D. M. Marom, “High-resolution, background-free, time-to-space conversion by collinearly phase-matched sum-frequency generation,” Opt. Lett. **36**(11), 1957–1959 (2011).

2. D. Shayovitz, H. Herrmann, W. Sohler, R. Ricken, C. Silberhorn, and D. M. Marom, “High resolution time-to-space conversion of sub-picosecond pulses at 1.55μm by non-degenerate SFG in PPLN crystal,” Opt. Exp. **20**(24), 27388-27395 (2012).

3. D. Shayovitz, H. Herrmann, W. Sohler, R. Ricken, C. Silberhorn, and D. M. Marom, “Time-to-space conversion of ultrafast waveforms at 1.55μm in a planar periodically poled lithium niobate waveguide,” Opt. Lett. **38**(22), 4708-4711 (2013).

4. D. Shayovitz, H. Herrmann, W. Sohler, R. Ricken, C. Silberhorn, and D. M. Marom, “Full-field reconstruction of ultrashort waveforms by time to space conversion interferogram analysis,” Opt. Exp. **22**(17), 20205-20213 (2014).

Abbreviations

AR	**A**nti-**R**eflection
AWG	**A**rrayed **W**aveguide **G**rating
BBO	**B**eta **B**arium **B**orate
CD	**C**hromatic **D**ispersion
CW	**C**ontinuous **W**ave
DFG	**D**ifference-**F**requency **G**eneration
FWHM	**F**ull **W**idth **H**alf **M**aximum
FWM	**F**our **W**ave **M**ixing
IL	**I**nsertion **L**oss
LO	**L**ocal **O**scillator
MLL	**M**ode **L**ocked **L**aser
OPO	**O**ptical **P**arametric **O**scillator
OSA	**O**ptical **S**pectrum **A**nalyzer
OTDM	**O**ptical **T**ime **D**ivision **M**ultiplexing
PLC	**P**lanar **L**ightwave **C**ircuit
PM	**P**olarisation **M**ultiplexing
PMD	**P**olarisation **M**ode **D**ispersion
PPLN	**P**eriodically-**P**oled **L**ithium **N**iobate
QPM	**Q**uasi **P**hase-**M**atching
QPSK	**Q**uadrature **P**hase **S**hift **K**eying
SDM	**S**pace **D**ivision **M**ultiplexing
SFG	**S**um-**F**requency **G**eneration
SHG	**S**econd **H**armonic **G**eneration
SNR	**S**ignal-to-**N**oise **R**atio
SPM	**S**elf-**P**hase **M**odulation
WDM	**W**avelength **D**ivision **M**ultiplexing
XPM	**C**ross-**P**hase **M**odulation

Chapter 1: Introduction

1.1 Ultrafast optical signals:

Enabling fundamental science and technology

Since the generation of the first sub-picosecond (ps) optical pulses in the 1970's [1] the field of ultrafast optics has developed continually, with ever shorter pulse durations being attained including the recent demonstration of sub-100 attosecond pulses [2]. Today ultrashort pulses are an essential investigative and enabling tool in a wide variety of scientific disciplines and technology platforms. As the shortest controllable events that mankind has produced, these pulses offer unprecedented temporal resolution for time domain measurements of ultrafast physical phenomena and also for data processing and communications technologies. A number of advances in fundamental science have been made possible by ultrashort optical pulse technology, for example time-resolved studies of molecular interactions [3, 4], advanced microscopy techniques in biophotonics [5] and optical frequency combs for metrology applications [6]. At the same time many areas of technology utilise ultrashort pulses, for example optical communications [7], photonically-assisted data processing [8] and the increasingly significant field of photomedicine [9].

With ever shorter optical pulse durations being achieved, new manipulation and measurement techniques must be developed. The physical mechanism on which these techniques are based must have a response time least as short as the pulse itself; otherwise the necessary temporal resolution is lacking. For 100 femtosecond (fs) pulses this implies that the control mechanism should have an operating bandwidth of greater than 10 THz. State of the art electronic circuits are limited to bandwidths of ~100 GHz and so lack the temporal resolution needed to directly control sub-ps duration pulses. In the absence of readily available alternatives, the mechanisms generally used to manipulate sub-ps pulses are based on nonlinear optical interactions between the pulses themselves.

Nonlinear optics serves as a means to control light by using light, providing the key to ultrashort pulse control and measurement. Fortuitously, but not surprisingly, the fields of ultrafast optics and nonlinear optics have developed hand in hand. The high peak powers of fs pulses enable strong nonlinear interactions, and in turn these interactions can be used to generate, characterise and control these pulses. We can understand how nonlinear optics comes into play by looking at the induced polarisation *P(t)* due to the electric field of an optical wave propagating inside a medium:

$$P(t) = \varepsilon_0 \left(\chi^{(1)} E(t) + \chi^{(2)} E^2(t) + \chi^{(3)} E^3(t) + \ldots \right) \tag{1.1}$$

where ε_0 is the permittivity of free space, *E(t)* is the time-varying electric field and $\chi^{(1)}$, $\chi^{(2)}$ and $\chi^{(3)}$ are the linear susceptibility and second and third order nonlinear susceptibilities respectively. These χ terms determine the strength of the induced linear and nonlinear polarisation by the electric field. Since the magnitude of the susceptibilities decreases rapidly with each successive higher order, the nonlinear terms are negligible as long as the electric field strength (or in other words the optical intensity) is low. In this linear regime light propagates inside a medium subject to the familiar laws of refraction, scattering and absorption. However when the light intensity is such that the higher order terms become significant, nonlinear optical effects can be observed. For this reason the nonlinear phenomenon of frequency doubling was first observed [10] just in one year after the invention of the laser in 1960, with the whole field of nonlinear optics undergoing a period of rapid growth in the following years.

One of the most widely used nonlinear optics phenomena is wavelength conversion. In the linear optics regime the induced polarisation of atoms or molecules results in a dipole oscillation at the same frequency as the impinging electric field. The light radiated by this dipole is then also at the same frequency as the original light wave. However, when the higher order terms of Eqn 1.1 are taken into account we can see that the radiated light includes new frequency components. Writing the time-varying (optical frequency) electric field as:

$$E(t) = A \exp(-j\omega t) + c.c. \tag{1.2}$$

where *A* is the field amplitude, ω is the angular frequency and *c.c.* stands for complex conjugate, and looking only at the 2nd order term from Eqn 1.2 we have [11]:

$$P^{(2)}(t) = 2\varepsilon_0 \chi^{(2)} A^2 + \varepsilon_0 \chi^{(2)} A^2 \exp(-j2\omega t) + c.c. \tag{1.3}$$

The first term is DC and represents optical rectification, which is the induction of a static electric field in the propagation medium and of no particular interest to us here.

What is immediately noticeable in the second term is that the induced dipole is oscillating at 2ω i.e. twice the original optical frequency. Therefore light at doubled frequency is radiated and we now have the phenomenon of second harmonic generation (SHG). In the example above we assume a single optical wave entering the nonlinear medium, however the general case is given by the interaction of two waves at different frequencies:

$$E(t) = A_1 \exp(-j\omega_1 t) + A_2 \exp(-j\omega_2 t) + c.c \tag{1.4}$$

The waves at frequencies ω_1 and ω_2 could be two different beams of light propagating together inside a nonlinear medium. Taking the 2nd order term from Eqn 1.1 we now have:

$$\begin{aligned} P^{(2)}(t) = 2\varepsilon_0 \chi^{(2)}\left(A_1^2 + A_2^2\right) + \varepsilon_0 \chi^{(2)}(A_1^2 \exp(-j2\omega_1 t) + A_2^2 \exp(-j2\omega_2 t) \\ + 2A_1 A_2 \exp(-j(\omega_1 + \omega_2)t) + 2A_1 A_2^* \exp(-j(\omega_1 - \omega_2)t) + c.c) \end{aligned} \tag{1.5}$$

In addition to the DC term and the two SHG terms from each wave individually, we also have two cross terms at the sum and difference frequencies of the two waves representing sum-frequency generation (SFG) and difference-frequency generation (DFG). Here we can see a significant aspect of nonlinear optics generally, and the most important one for the work presented here. This is the interaction of different light waves inside the nonlinear medium, which jointly generate a new light wave whose complex amplitude and frequency depends on that of the original waves. This

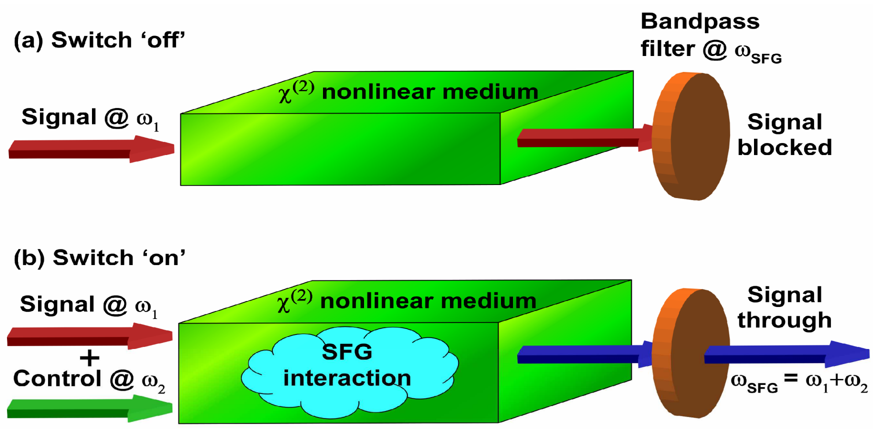

Fig. 1.1. Generic all-optical switch based on SFG and spectral filtering. (a) A signal beam at frequency ω_1 passes through the (transparent) nonlinear medium and is blocked by a bandpass filter, in this case the switch is 'off'. (b) To open the switch a control beam at frequency ω_2 is sent into the nonlinear medium together with the signal. The SFG light generated at frequency ω_{SFG} = $\omega_1 + \omega_2$ is now transmitted by the bandpass filter, so the switch is 'on'.

is the nonlinear optics mechanism which enables the control of light with light. An example of a generic all-optical switch is shown in Figure 1.1.

By examining the 3rd order term from Eqn 1.1 we could also see third harmonic generation and four wave mixing (FWM). Another important 3rd order nonlinear phenomenon is the Kerr effect, which is a nonlinear refractive index responsible for a number of phenomena including self-phase modulation (SPM) in the temporal domain and self-focusing in the spatial domain.[2] High harmonic generation (4th harmonic and upwards) is also possible, however this requires extremely high optical intensities in order to achieve reasonable conversion efficiency and is not relevant to the work presented here.

[2] Although the term 'nonlinear optics' specifically refers to the higher order nonlinear terms in the induced dipole (Eqn 1), it also elucidates the fundamental principle of this field which is: light propagating through a medium is not only altered by the medium but also alters the medium itself. The example of self-focusing due to the nonlinear refractive index is instructive. An intense beam of light propagating through a nonlinear medium (note that with enough optical power any medium, including air, is 'nonlinear') will cause an increase in refractive index via the 3rd order Kerr effect. This nonlinear refractive index will be largest on the optical axis where the optical intensity is highest and will get progressively smaller at greater radial distance away from the axis. In fact the nonlinear refractive index spatial profile will match the intensity profile of the beam. Since most laser beams have a Gaussian spatial profile, the induced refractive index profile will approximate a parabola (at least close to the optical axis). In other words the beam will create a 'lens' in the medium through which it is propagating. This lens will tend to focus the beam inwards, resulting in higher intensity on-axis, which will cause a larger induced nonlinear refractive index. Further focusing will follow and so on. The result is a positive feedback loop which will only end either when enough of the light is absorbed, causing a drop in optical power and weakening of the effect, or when the electric field strength increases to the point where it causes dialectric breakdown of the medium. This accelerating dynamic behaviour is characteristic of nonlinear systems.

An alternative approach to pulse manipulation is to work in the spectral domain, taking advantage of the extremely large bandwidths of ultrashort pulses. The temporal pulse duration and spectral bandwidth of a light pulse are Fourier transform related; the shorter the pulse, the broader the bandwidth. For sub-picosecond bandwidth-limited pulses, the spectral bandwidth is of the order of a few THz (equivalent to some 10's of nanometres in wavelength space). In order to modulate the individual frequency components which comprise this bandwidth, the pulse's spectrum must be dispersed in space and this is achieved as follows [12].

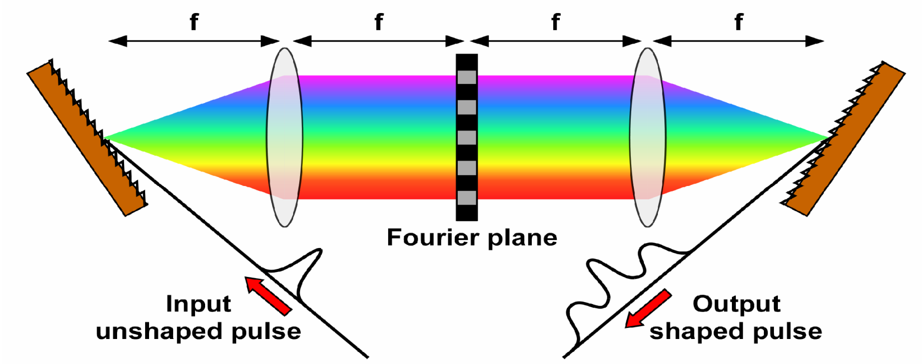

Fig. 1.2: Spectral processor used for pulse shaping. The input ultrashort pulse is angularly dispersed by a diffraction grating. A Fourier lens converts this angular dispersion to a linear spatial dispersion at the Fourier plane, so that each frequency component of the pulse is focused to a different position along the plane. This allows direct amplitude and / or phase modulation of each spectral component individually, usually by a static mask or liquid crystal based spatial modulator. The spatial dispersion is then reversed by a second Fourier lens – grating pair, resulting in a shaped pulse at the output. Arbitrary temporal waveforms can be generated in this way, limited by the spectral resolution of the processor.

The pulse is first incident onto a diffraction grating which separates the frequencies into different angles (see Fig. 1.2). A lens placed at a distance of one focal length from the grating then performs a spatial Fourier transform on this dispersed light, converting the angular dispersion into a linear spatial dispersion at the focal plane. At this plane each spectral component is focused to a unique position in space allowing amplitude and phase modulation of each frequency independently. The modulation is typically performed using an amplitude or phase mask or by a spatial light modulator. The modulated light then undergoes a reverse process of spatial Fourier transform and is incident on a second diffraction grating, removing the spatial and angular dispersion and resulting in a collimated output beam. This setup, as shown in Fig. 1.2, is known as a 4f 'spectral processor' or 'pulse shaper', since the total distance between the gratings is 4 times the lenses' focal length. Since the time and frequency domains are linked by a Fourier transform (a corollary to the time-energy uncertainty principle mentioned above), various temporal waveform shapes can be generated by such spectral domain manipulations. A significant advantage of the spectral processor is that the modulation occurs in the spatial domain with a far higher resolution than that which can be achieved in the temporal domain.

An intriguing possibility is to combine nonlinear optics and spectral processing in order to achieve new ultrashort pulse manipulation and measurement capabilities. The two fields have complementary characteristics which can mutually compensate for each other's deficiencies. On the one hand spectral processing allows high resolution amplitude and phase modulation in the frequency domain, by providing access to the individual spectral components of light dispersed in space. However the liquid crystal based spatial modulators typically used for pulse shaping have a maximum frame rate of around 100 Hz, making them unsuitable for processing non-repetitive temporal waveforms such as are used, for example, in optical data transmission (see Chapter 1.3) . On the other hand nonlinear optics can provide the fast gating mechanism, effectively instantaneous compared with sub-picosecond pulse durations, needed to obtain high temporal resolution control. However nonlinear interactions between broadband ultrashort pulses often suffer from the effects of chromatic dispersion (CD) and group velocity mismatch (GVM) in the nonlinear medium. This causes temporal walkoff between the fundamental and generated SHG pulses, which may have widely separated central wavelengths, resulting in a low optical power and temporally distorted SHG pulse. By performing the nonlinear interaction inside a spectral processor the interacting pulses' bandwidth at each point in space is narrowed. This effectively transforms the interaction from one between ultrashort pulses into one between multiple quasi-monochromatic beamlets of light, each centred at a different frequency, which experience negligible chromatic dispersion. An example of this combination of nonlinear optics with spectral processing is time-to-space conversion by spectrally-resolved SFG, which is introduced in section 1.2 below.

1.2 Time-to-space conversion

Time-to-space (T-S) conversion is a technique designed to transfer time domain information to the space domain; or in other words, to generate the spatial image of a temporal waveform. It is based on sum-frequency generation between a spatially dispersed signal waveform and reference pulse inside a spectral processor, producing a narrow bandwidth SFG wave which then forms a spatial image of the signal waveform.

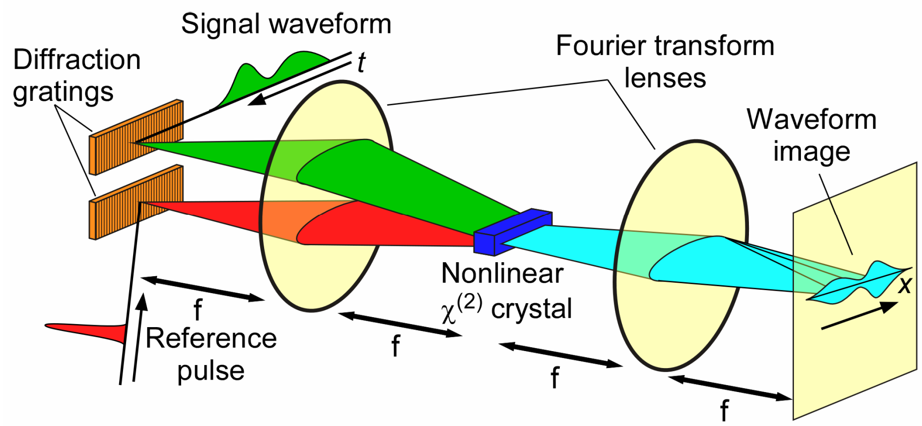

Fig. 1.3: Time-to-space conversion concept. Time domain information is converted to a spatial image with the temporal coordinate *t* mapped linearly to a spatial coordinate *x*. Note that in the experimental setups described in this thesis the signal and reference beams propagate collinearly in the nonlinear crystal, whereas here they are shown at crossed angles for clarity.

The principle of operation of T-S conversion [13-18] is summarised here with the main stages described mathematically. The physical arrangement of the optical elements and the beam paths in a time-to-space converter is shown schematically in Fig. 1.3. The signal and reference pulses both enter the time-to-space converter and are incident on diffraction gratings from opposite angles. This causes each pulse to be angularly dispersed in mutually opposite directions. The signal and reference fields immediately after the gratings are (assuming a Gaussian beam spatial profile and Gaussian pulse envelope):

$$E_S^{in}(x,y;t) = A_S \exp\left[-\frac{x^2}{w_x^2}\right]\exp\left[-\frac{y^2}{w_y^2}\right]\exp\left[-\frac{1}{\tau^2}\left(t-t_0-\frac{\rho_S}{c}x\right)^2\right]\exp[j\omega_S t] \qquad (1.2.1)$$

$$E_R^{in}(x,y;t) = A_R \exp\left[-\frac{x^2}{w_x^2}\right]\exp\left[-\frac{y^2}{w_y^2}\right]\exp\left[-\frac{1}{\tau^2}\left(t+\frac{\rho_R}{c}x\right)^2\right]\exp[j\omega_R t] \qquad (1.2.2)$$

where $A_{S,R}$ are the signal and reference field amplitudes, $w_{x,y}$ are the ($1/e^2$ radius) beam sizes projected on to the gratings (the beam sizes can be different in the x and y

directions and are assumed here to be identical for signal and reference beams), 2τ is the pulse duration full-width measured at $1/e^2$ intensity points (assumed here to be identical for signal and reference pulses), t_0 is the relative time delay between the signal and reference pulses, c is the speed of light, $\omega_{S,R}$ are the signal and reference pulses' central angular frequencies and $\rho_{S,R}$ are the signal and reference pulse dispersion parameters. Note that t_0 represents the temporal information which must be transferred to the spatial domain by time-to-space conversion. The angularly dispersed signal and reference pulses then pass through a Fourier lens, resulting in equal but opposite linear spatial dispersions at the focal plane (Fourier plane). The dispersed signal pulse field at the Fourier plane is found by performing a spatial Fourier transform on Eqn. 1.2.1:

$$
\begin{aligned}
E_S^{FP}(u,v;t) = -j\frac{\pi A_S w_x w_y}{\lambda_S f_1\sqrt{1+N^2}} \exp\left[-\frac{(t-t_0)^2}{\tau^2}\cdot\frac{1}{1+N^2}\right] \exp\left[-\left(\frac{\pi w_x u}{\lambda_S f_1}\right)^2\cdot\frac{1}{1+N^2}\right] \\
\times\exp\left[-\left(\frac{\pi w_y v}{\lambda_S f_1}\right)^2\right] \exp\left[-j(t-t_0)\frac{2\pi c}{\lambda_S f_1 \rho_S}\cdot\frac{N^2}{1+N^2}\cdot u\right] \exp[j\omega_S t]
\end{aligned}
\tag{1.2.3}
$$

where λ_S is the signal pulse central wavelength and f_1 is the Fourier lens focal length. Here a factor N, known as the serial-to-parallel resolution factor, has been used to collect various constants in order to simplify the equation. The N factor is defined as $N = \dfrac{w_x \rho_S}{c\tau}$ and determines the number of signal pulses that can be simultaneously time-to-space converted by a single reference pulse. Looking at the first exponential term in Eqn. 1.2.3 above, it can be seen that the temporal duration of the pulse has increased by a factor $(1+N^2)$ and of course the field amplitude has decreased by the same factor. This is due to the pulse being spectrally resolved at the Fourier plane, so that its spectral bandwidth at each point in space is a $1/(1+N^2)$ fraction of the total bandwidth. The dispersed reference field has the same form except that the spatio-temporal phase term (in the fourth exponential term shown in Eqn. 1.2.3) is positive, t_0 is zero and the central frequency and wavelength are equal to ω_R and λ_R respectively.

A temporal Fourier transform is now performed on Eqn. 1.2.3 in order to represent the linearly dispersed signal pulse in the frequency domain:

$$\tilde{E}_S^{FP}(u,v;\omega) = -j\frac{\pi^{3/2}A_S\tau w_x w_y}{\lambda_S f_1}\exp\left[-\left(\frac{\tau}{2}\right)^2\left(1+N^2\right)\left(\omega-\omega_S+\frac{2\pi cu}{\lambda_S f_1\rho_S}\cdot\frac{N^2}{1+N^2}\right)^2\right]$$
$$\times\exp\left[-\left(\frac{\pi w_x u}{\lambda_S f_1}\right)^2\cdot\frac{1}{1+N^2}\right]\exp\left[-\left(\frac{\pi w_y v}{\lambda_S f_1}\right)^2\right]\exp\left[-j(\omega-\omega_S)t_0\right] \quad (1.2.4)$$

where $\tilde{E}_S^{FP}$ represents the dispersed signal pulse field in the frequency domain. We can now see that the temporal information t_0 is carried on the spectral phase term given by the last exponential in Eqn. 1.2.4 above. Crucially, this spectral phase is distributed throughout space on the dispersed frequency components of the signal pulse, thus providing the spatial-temporal link which is the central working principle of the time-to-space converter. The dispersed reference wave equation is identical to Eqn. 1.2.4 expect that the spatial dispersion term (in the first exponential) has a negative sign and the last exponential vanishes since $t_0 = 0$ for the reference pulse. At the Fourier plane the signal and reference pulse spectra overlap each other in space, with equal magnitude but opposite direction linear dispersions.

By placing a $\chi^{(2)}$ nonlinear crystal at the Fourier plane an SFG interaction occurs between each pair of overlapping signal and reference frequency components. The second order nonlinear polarisation P_{NL} excited in the crystal is given in the frequency domain by the convolution of the dispersed signal pulse shown in Eqn. 1.2.4 and the corresponding dispersed reference pulse frequency domain representation [11]:

$$P_{NL}(u,v,z;\omega) = 2\varepsilon_0 d_{eff}\int_{-\infty}^{\infty}\tilde{E}_S^{FP}(u,v;\varpi)\tilde{E}_R^{FP}(u,v;\omega-\varpi)$$
$$\times\exp\left[j\left(k_S(\varpi)+k_R(\omega-\varpi)\right)z\right]d\varpi \quad (1.2.5)$$

where ε_0 is the permittivity of free space, d_{eff} is the effective second order nonlinearity, ϖ is an integration variable and $k_{S,R}$ are the signal and reference wavevectors. Due to the frequency dependence of the signal and reference wavevectors (via chromatic dispersion), GVM can result in temporal walkoff between the signal and reference pulses inside the nonlinear crystal resulting in spectral distortion of the output SFG wave. However, both signal and reference pulses have increased temporal durations inside the time-to-space processor (as noted above in relation to Eqn. 1.2.3). In addition the signal and reference pulse wavelengths can be close together if we choose, for example both can be in the near IR. Considering the time-to-space converter optical arrangement used in the experiments detailed in this thesis, the temporal walkoff was estimated to be less than 1% of the signal or reference stretched pulse duration. Therefore temporal walkoff over the signal and reference beam interaction length in the nonlinear crystal is neglected here. This assumption holds as long as the signal and reference beams are propagating in free-space and the nonlinear medium is a bulk crystal. Since temporal walkoff increases with the SFG interaction length, this assumption may not be valid for time-to-space conversion in long waveguides. The SFG wave generated by the induced nonlinear polarisation is:

$$\frac{\partial}{\partial z}\tilde{E}_{SFG}(u,v,z;\omega)=\frac{j\omega_{SFG}^{2}\mu_{0}}{2k(\omega_{SFG})}P_{NL}(u,v,z;\omega)\exp[-jk_{SFG}(\omega)z] \tag{1.2.6}$$

where $\omega_{SFG}=\omega_S+\omega_R$ is the SFG wave angular frequency, μ_0 is the permeability of free space and k_{SFG} is the SFG wavevector. Due to the equal magnitude but opposite direction dispersions, each pair of frequency components adds up to the same sum-frequency. Therefore the SFG wave generated has the same frequency at each spatial location on the crystal aperture. In other words a quasi-monochromatic[3] and spatially coherent SFG wave is generated all along the nonlinear crystal. The SFG field at the output of the crystal is found by integrating Eqn. 1.2.6 over the crystal length L_C, assuming that the SFG field at the crystal input face is zero. Substituting in Eqns. 1.2.4 (and the corresponding dispersed reference pulse representation) and 1.2.5 and performing the integration and convolution results in:

[3] The extent to which the generated SFG wave is really quasi-mononchromatic (i.e. has a bandwidth much narrower than that of the incoming signal pulse) depends on the spectral resolution of the time-to-space processor. See the discussion on the time window of operation below.

$$
\begin{aligned}
\tilde{E}_{SFG}(u,v;\omega) = {} & -j\frac{2^{3/2}\pi^{9/2}d_{eff}L_C A_S A_R \tau w_x^2 w_y^2}{n_{SFG}\lambda_{SFG}\lambda_S\lambda_R f_1^2\sqrt{1+N^2}} \\
& \times \exp\left[-\left(\omega_S^2+\omega_R^2\right)\left(\frac{w_y v}{2cf_1}\right)^2\right]\exp\left[-\left(\omega_S^2+\omega_R^2\right)\left(\frac{w_x u}{2cf_1}\right)^2\frac{1}{1+N^2}\right] \\
& \times \exp\left[-\frac{t_0^2}{2\tau^2\left(1+N^2\right)}\right]\exp\left[-j\frac{\omega_{SFG}t_0 u}{2f_1\rho}\cdot\frac{N^2}{1+N^2}\right] \\
& \times \exp\left[-\left(\frac{\tau}{2}\right)^2\cdot\frac{1+N^2}{2}\left(\omega-\omega_{SFG}+\left(\omega_S-\omega_R\right)\frac{u}{f_1\rho}\frac{N^2}{1+N^2}\right)^2\right] \\
& \times \mathrm{sinc}\left[\frac{\left(\omega-\omega_{SFG}\right)}{2}\cdot\beta L_C\right]\exp\left[-j\frac{\left(\omega-\omega_{SFG}\right)}{2}\cdot\left(\beta L_C+t_0\right)\right]
\end{aligned}
\tag{1.2.7}
$$

where n_{SFG} is the refractive index of the nonlinear crystal at the SFG wavelength, $\beta = \frac{1}{v_g^{SFG}} - \frac{1}{v_g}$ is the is the inverse GVM between the SFG wave (with group velocity v_g^{SFG}) and the signal and reference waves (each with the same group velocity v_g, according to the assumption of zero GVM between the signal and reference pulses as mentioned earlier). Since the fundamental (signal and reference) waves and the generated (SFG) wave have widely spaced wavelengths their mutual GVM can no longer be neglected and will influence the generated SFG wave for sufficiently long interaction lengths.

Equation 1.2.7 shows the field of the SFG wave at the output face of the nonlinear crystal. By looking at the various terms we can discern several relevant facts about the SFG wave. The first two Gaussian exponential terms show the spatial extent of the field at the crystal output face. The third exponential shows the decrease in SFG output power with increasing time delay between the signal and reference pulses. The fourth exponential is a linear spatial phase term carrying the time delay information t_0; this is the important part of the above equation, showing the time-to-space converted information. The fifth exponential shows the Gaussian shaped spectrum centred at the SFG frequency, with however an additional spatial-spectral coupling term which drops out in the wavelength degenerate case (where $\omega_S \approx \omega_R$). The sinc term shows the spectral filtering effect of GVM between the fundamental (signal and reference) and generated (SFG) waves.

As can be seen in Eqn. 1.2.7 the generated light carries a spatial phase which varies linearly across the SFG beam aperture. Another lens of focal length f_2 performs a spatial Fourier transform on the SFG beam, focusing it to the output image plane and converting the spatial phase into a transverse shift of the focused image:

$$
\begin{aligned}
\tilde{E}_{out}(x', y'; \omega) = & \frac{2^{3/2}\pi^{11/2} d_{eff} L_C A_S A_R \tau w_x w_y}{n_{SFG} \lambda_S \lambda_R f_2} \\
& \times \exp\left[-2\left(\frac{f_1}{f_2} \cdot \frac{y'}{w_y} \right)^2 \right] \\
& \times \exp\left[-\left(\frac{f_1}{f_2} \cdot \frac{\sqrt{2(1+N^2)}}{w_x} \right)^2 \left(x' + \frac{f_2}{f_1} \cdot \frac{c}{2\rho} \cdot \frac{N^2}{1+N^2} \cdot t_0 \right)^2 \right] \\
& \times \exp\left[-\left(\frac{\tau}{2} \right)^2 \frac{1+N^2}{2} (\omega - \omega_{SFG})^2 \right] \\
& \times \exp\left[-\frac{{t_0}^2}{2\tau^2 (1+N^2)} \right] \\
& \times \sin c\left[\frac{(\omega - \omega_{SFG})}{2} \cdot \beta L_C \right] \exp\left[-j \frac{(\omega - \omega_{SFG})}{2} \cdot (\beta L_C + t_0) \right]
\end{aligned}
\tag{1.2.8}
$$

For the sake of simplicity this final step assumes that $\omega_S \approx \omega_R$ i.e. the wavelength degenerate case where both signal and reference pulses have the same central wavelength. Equation 1.2.8 gives the output field of the SFG light at the image plane showing a spatial image of the signal temporal waveform. The extent of the focused image in the vertical and horizontal directions is given in the first and second exponentials respectively. It can be seen that the vertical extent of the image is determined by the input beam size and by the ratio of the input and output Fourier lens focal lengths f_1 and f_2; in other words the time-to-space processor simply operates as a telescope in the vertical direction and no transfer of information from the temporal to spatial domains occurs (since there is no spatial dispersion in the vertical direction). The horizontal width of the focused pulse image is also determined by these same factors and in addition by the N factor which represents the spectral resolution of the time-to-space processor.

The essential point in Eqn. 1.2.8 is that the transverse position of the focused image on the output image plane is proportional to the time delay between the signal and reference pulses, as can be seen in the second exponential. Therefore a one-to-one mapping of the temporal coordinate t to one spatial dimension x is obtained; that is 'time-to-space conversion'. This spatial image can then be detected by a camera or by an array of optoelectronic photodetectors, thus measuring the original temporal pulse envelope.

A significant feature of T-S conversion is that not only the time-dependent intensity envelope but also the time-dependant phase of the signal waveform is converted to spatial phase on the output SFG wave. For example if the signal waveform has a linear frequency chirp (in other words a quadratic phase) the generated SFG light will also have a quadratic spatial phase, causing a defocus of the output spatial image [13, 14]. As mentioned above the SFG light is quasi-monochromatic, a fact which can enable measurement of the phase information by interferometric detection using a narrow linewidth local oscillator (LO). This has important implications for the two main proposed applications of time-to-space conversion, namely optical communications and ultrashort waveform measurement (see sections 1.3 and 1.4 below).

Since time-to-space conversion is proposed as tool for manipulating and measuring ultrashort pulses, it is important to consider its various performance parameters. The two principle ones are the time window of operation and time-to-space conversion efficiency. These two parameters are determined by the spatial characteristics of the input signal and reference beams, the type of nonlinear medium used and the spectral processor geometry. Furthermore they are interdependent; a fact which has had an impact on the previous development of the T-S conversion technique and also on the research goals of this project.

The time window determines the maximum temporal duration of the signal waveform that can be spatially imaged. It is limited by the decrease in strength of the SFG interaction with greater signal pulse-to-reference pulse time delay. Maximum SFG power is obtained when there is complete temporal overlap between the two pulses at the nonlinear crystal, whereas for large delays the generated SFG power is negligible and no T-S conversion takes place (see Fig. 1.4). The typical time window obtained in the T-S experiments presented in this thesis is around 35 ps to 50 ps FWHM. The time window can be widened by increasing the spectral resolution of the dispersed light at the Fourier plane inside the spectral processor; this increased spectral resolution can be obtained by increasing the input beam size on the diffraction gratings (note that the spectral resolution is represented in the above equations by the *N* factor). Increased spectral resolution at the Fourier plane also leads to the SFG wave being generated with a narrower bandwidth, since each signal and reference frequency component pair will interact more completely with itself and less with adjacent frequency components (which causes spectral broadening of the SFG light). In fact the time window duration and the bandwidth of the SFG output light are inversely linked; another example of the Fourier transform relation of the time and frequency domains.

The time-to-space conversion efficiency is defined as the SFG output power divided by the input signal power. Clearly this should be as high as possible in order to achieve a good signal-to-noise ratio (SNR) at the photodetector array or camera located at the output image plane. Since the SFG power is proportional to the signal and reference pulse energies, one immediate way to increase the conversion efficiency is to use a more intense reference pulse. However for real-world applications this may not be possible or desirable. Generally speaking we would like the time-to-space converter to consume the minimum possible optical power. Therefore a more useful measure of T-S power consumption is the conversion efficiency slope, which is defined as the conversion efficiency per watt of reference beam power.

The conversion efficiency slope depends on the choice of nonlinear crystal since different nonlinear materials have stronger or weaker $\chi^{(2)}$ coefficients. Also, the SFG power generated depends on the interaction length of the frequency component pairs

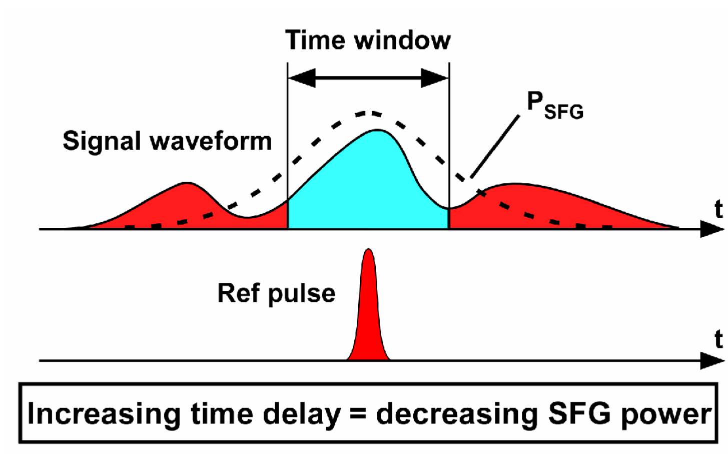

Fig. 1.4: Time window of operation. As the temporal overlap between the reference pulse and any part of the signal waveform increases, the instantaneous SFG power decreases resulting in a weaker output signal. For large time delays the SFG power is negligible and no time-to-space conversion occurs. The blue indicates the part of the signal waveform which falls within the FWHM time window (FWHM is used as an arbitrary limit for the time window; other definitions can be used, for example $1/e^2$ intensity points).

within the nonlinear crystal; longer interaction length results in higher SFG power. The interaction length can be increased by less tight focusing of the spectral components at the Fourier plane, in other words by reducing the resolution of the spectral processor. Here we can already see the main design problem of a time-to-space processor – in order to increase the conversion efficiency we must settle for a smaller time window and vice versa. This trade-off between the two main performance parameters is inherent in free-space T-S conversion as described above and as shown in Fig. 1.3; part of the work presented here is an effort to break this invariance by performing guided wave T-S conversion (see Chapter 3).

Time-to-space conversion using a parametric (i.e. non-resonant) optical nonlinearity was first demonstrated using SHG between signal and reference pulses at 1.06 μm in a lithium niobate nonlinear crystal [13]. A greatly increased conversion efficiency of 58% was then achieved using a potassium niobate nonlinear crystal in a different spectral processor geometry, however with a rather small time window of 4 ps [15]. Finally time-to-space conversion was demonstrated using signal and reference pulses at 1560 nm in periodically-poled lithium niobate (PPLN) nonlinear crystal [18]; this wavelength is significant for optical communications applications of T-S conversion (see section 1.3 below).

1.3 Applications of time-to-space conversion I: Optical communications

The current reach and scale of global communications networks would not be possible without fibre optics data transmission, which forms the backbone of modern long distance communications. Optical communications technology must keep pace with the trend for ever increasing data capacity demands, a trend which shows no sign of slowing [19]. As an example, Figure 1.5 shows an exponential growth in global data traffic on mobile networks from 2007-2012. Installing new fibre is costly and inefficient, so a variety of multiplexing and modulation degrees of freedom are typically exploited to increase the data capacity of existing links. Among the optical multiplexing techniques available are wavelength division multiplexing (WDM) with each wavelength comprising a separate data channel, polarisation multiplexing (PM) where data is encoded on two orthogonal polarisations per wavelength, space division multiplexing (SDM) with multi-core or few-mode fibres carrying spatially orthogonal (i.e. separable) channels and finally optical time division multiplexing (OTDM) where multiple low bit rate tributaries are temporally interleaved into a single high bit rate serial channel. Advanced modulation schemes offer a means to transmit more bits of data on each symbol, for example quadrature phase shift keying (QPSK) in which information is encoded on the phase of the electric field [20]. In order to reach high bit rates a number of these techniques are typically combined. For example current industry standard 100 Gbit/s links employ polarisation multiplexing and 2 bits-per-

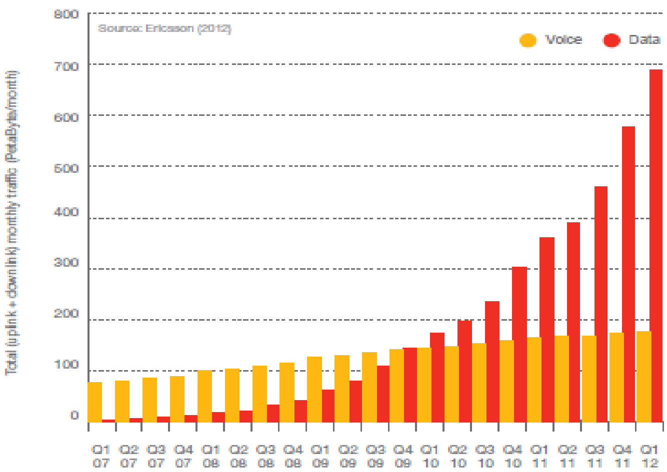

Fig. 1.5: Global total traffic in mobile networks 2007-2012. As an example of the trend for increasing communications network data capacity demands, an exponential growth rate can be seen for data traffic on mobile networks. (*Traffic and Market Report*, Ericsson (June 2012))

symbol modulation of an electronically generated 25 Gbaud/s serial channel on a single wavelength. A record single source 43 Tbit/s transmission rate has been demonstrated by combining five multiplexing and modulation spaces (WDM, SDM, PM, OTDM and QPSK), showing the potential of using several multiplexing and modulation techniques simultaneously [21].[4]

Optical time division multiplexing offers a means to increase the data capacity on a fibre optics network whilst lowering the number of wavelength channels; in other words to increase the spectral efficiency, defined as bits transmitted per second per Hz of bandwidth. This is significant since each additional WDM channel requires a separate and highly stable laser source, increasing the power requirements and complexity of the network. OTDM works by combining multiple low symbol rate tributaries, all at the same wavelength, into a single high symbol rate serial channel. In addition to optical communications, OTDM has applications in other areas such as photonically-assisted analogue-to-digital conversion [22, 23]. By combining OTDM with polarisation multiplexing and advanced modulation formats high spectral efficiencies of ~6 bits/s/Hz have been attained [7]. Generating an OTDM channel is relatively straightforward; passive optical delay lines are used to interleave the pulses from each tributary into their respective time slots on a frame-by-frame basis, as shown in Fig. 1.6. The time slot in which each pulse is placed therefore identifies the tributary to which it belongs. The necessity for using picosecond or sub-picosecond pulses in a high bit rate OTDM channel is problematic due to linear distortions, such as chromatic dispersion and polarisation mode dispersion, and nonlinear distortions, such as SPM, XPM and FWM, which occur during transmission in the optical fibre. However these distortions can, at least partially, be compensated for electronically by using coherent detection combined with digital signal processing [24].

[4] Baud/s is the single wavelength symbol rate, which in the case of optical communications is equivalent to the repetition rate of the optical pulses. For on-off keying modulation (i.e. 'zeros' and 'ones') the bit rate is simply equal to the baud rate. For advanced modulation formats such as QPSK, several bits are modulated onto each symbol resulting in a bit rate which is a multiple of the baud rate.

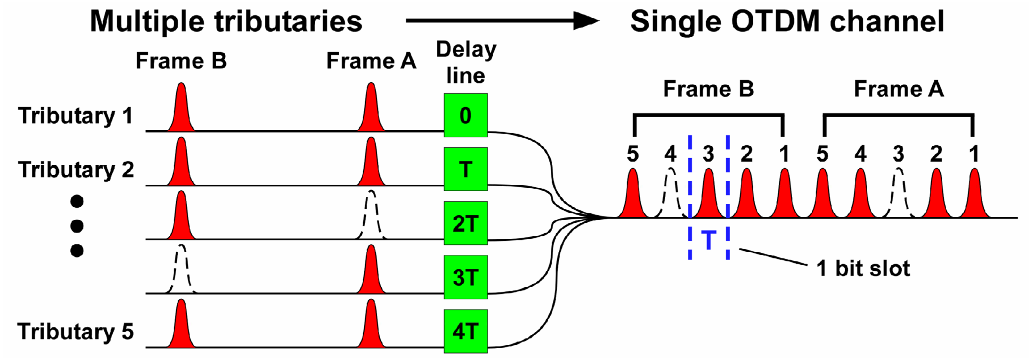

Fig. 1.6: Optical time division multiplexing. Separate low symbol rate tributaries are temporally interleaved by applying successively larger time delays into a single high symbol rate serial channel. In the example shown here five tributaries are multiplexed into an OTDM channel, resulting in a factor five increase in symbol rate. The empty dashed lines represent the absence of a pulse in a particular time slot, i.e. a 'zero' bit.

Receiving and detecting an OTDM channel is challenging since a >100 Gb/s OTDM pulse stream cannot be detected by an optoelectronic receiver, which is limited by device physics to a maximum bandwidth of around 100 GHz. In order to convert the lightwave data to an electrical signal a demultiplexing operation must be performed, in which the tributaries comprising the OTDM channel are separated back out into their original low symbol rates. This demultiplexing cannot be done optoelectronically, for this same reason of limited electrical bandwidth. Therefore demultiplexing is generally performed all-optically, taking advantage of the effectively instantaneous (attosecond) timescale of nonlinear optical phenomena.

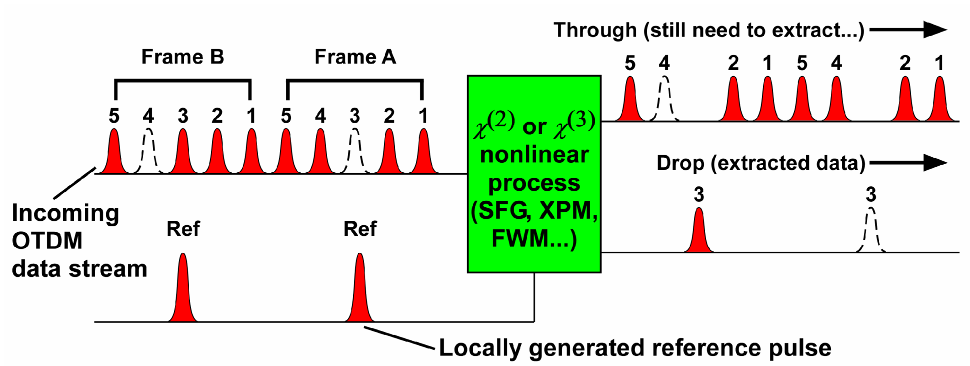

Fig. 1.7: Single-bit extraction OTDM demultiplexing. One frame of the transmitted OTDM bit stream and a single locally generated reference pulse undergo an nonlinear interaction, such as XPM or FWM, resulting in a single bit being extracted and separated out from the OTDM channel (bit number 3 in the example above). The specific tributary which is extracted depends on the time delay between the OTDM frame and the reference pulse. The remaining pulses continue to propagate in the OTDM serial channel and must be demultiplexed by further copies of the same device downstream.

A variety of nonlinear optics based techniques have been investigated for OTDM demultiplexing, among them the nonlinear optical loop mirror (NOLM) [25, 26], the cross-phase modulation Mach-Zehnder interferometer (XPM-MZI) [27, 28] and FWM-based spectral filtering extraction [29, 30]. As shown conceptually in Fig. 1.7 these techniques use a locally generated reference pulse to provide the temporal gating necessary to extract a signal pulse from the OTDM bit stream. Each of these methods has been successfully demonstrated for high bit rate OTDM demultiplexing, with both the NOLM [31] and FWM-based extraction [30] being used for 1.28 Tbaud/s demultiplexing. However they are all limited to single bit extraction, necessitating multiple cascaded devices in order to completely demultiplex the OTDM bit stream. Since power consumption and overall complexity increase with each additional device, the scalability of these techniques to higher baud rates is limited. In addition the task of inter-device clock synchronisation, necessary in order to extract the correct tributary at each device, becomes very challenging for high bit rates.

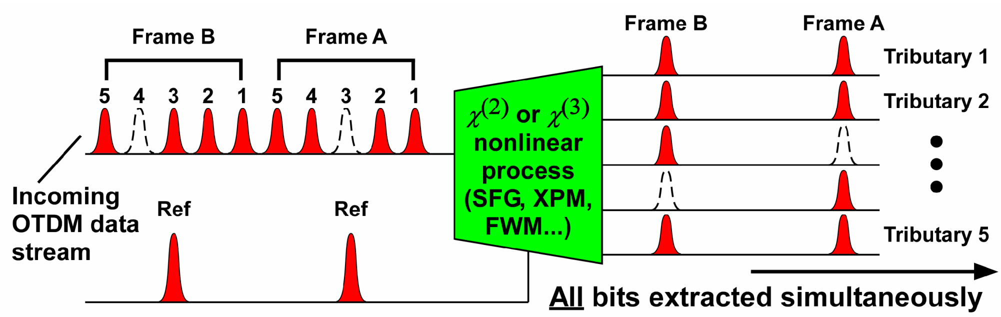

Fig. 1.8: Serial-to-parallel OTDM demultiplexing. A single reference pulse simultaneously extracts all tributaries from an OTDM channel, performing the inverse of the multiplexing operation shown in Fig. 1.6. Since only a single device is needed, power consumption, system complexity and clock synchronisation demands are all reduced, allowing scalability to higher OTDM bit rates.

Serial-to-parallel demultiplexing can overcome these problems by simultaneously extracting all the bits in an OTDM frame (Fig. 1.8). With a single reference pulse performing the entire demultiplexing operation the problem of inter-device clock synchronisation, as for single-bit extraction, becomes one of synchronising the reference pulse to the OTDM frame, a less onerous task. One example of serial-to-parallel demultiplexing is time-to-frequency conversion, where the temporal pulse pattern is imprinted on the spectrum of a generated FWM wave [32, 33]. However, with the demultiplexed data being carried on a spectrally broad FWM wave spanning many nanometers of bandwidth, coherent detection of phase information is less practical. Without the option of coherent detection, time-to-frequency conversion is less attractive for OTDM demultiplexing applications.

By transferring time domain information to the spatial domain, time-to-space conversion is able to perform the serial-to-parallel demultiplexing required to detect a high bit rate OTDM channel. Since the time delay between each signal pulse in the OTDM frame and a reference pulse is mapped to the transverse spatial position of each pulse image at the output plane, each OTDM pulse is demultiplexed to a unique position in space (see Fig. 1.9). An array of optoelectronic photodetectors placed at the output image plane can then detect each tributary individually. The spatial image refresh rate is equal to the inverse of the T-S time window duration and so is typically on the order of a few 10's of GHz, within the bandwidth of state of the art photodetectors. Alternatively the SFG light can be mixed with a narrowband local oscillator (LO) for coherent detection of phase information, enabling compatibility of time-to-space demultiplexing with advanced modulation formats.

Time-to-space conversion can satisfy many OTDM demultiplexing requirements, for example serial-to-parallel demultiplexing by a single device, a wide time window enabling scalability to high bit rate OTDM, coherent detection of phase information for compatibility with advanced modulation formats and operation at 1550 nm (in the optical communications c-band). Previously however time-to-space conversion has only been demonstrated using bulk optics elements such as lenses and diffraction gratings in a free-space setup. This arrangement is reasonable for laboratory experiments, but not for real-world applications of time-to-space conversion. One of the main goals of the research presented here is to implement guided wave time-to-space conversion using components such as nonlinear waveguides, eventually

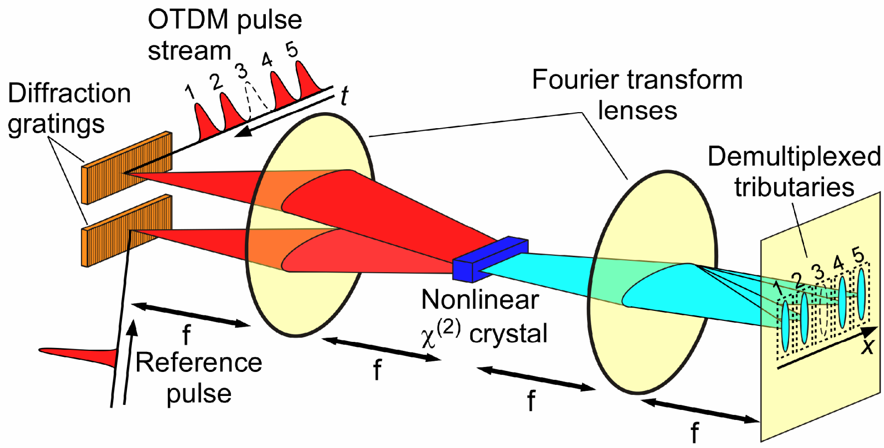

Fig. 1.9: OTDM demultiplexing by time-to-space conversion. The time-serial OTDM channel is demultiplexed to multiple space-parallel tributaries. An array of photodetectors (represented here by dashed boxes) can be placed at the output image plane to detect each tributary individually. Whilst direct intensity measurement of the pulse images discards phase information, coherent detection with a narrow linewidth local oscillator (not shown here) can instead be used to measure the field amplitude and phase.

integrating all the optical functionalities of the T-S convertor into a single planar lightwave circuit on a chip (see Chapter 3). This will have the additional effect of significantly lowering the optical power consumption of the time-to-space conversion process, another important requirement for OTDM applications.

1.4 Applications of time-to-space conversion II: Ultrashort pulse measurement

Accurate time domain measurements are essential for understanding the dynamics of ultrashort optical pulse generation and also for their successful utilisation in various scientific and technology fields, for example coherent control of atomic and molecular states by shaped femtosecond pulses [34] and high harmonic generation of x-rays [35]. Whereas some measurement techniques record the pulse intensity envelope, important information is also contained in the temporal phase. For example, phase measurements can be used to determine whether a pulse is bandwidth-limited or has undergone chromatic dispersion or nonlinear phase distortions. Whereas a bandwidth-limited pulse has a flat phase, a chirped pulse is defined by a quadratic phase in time (see Fig. 1.10). Full-field (amplitude and phase) measurement enables complete temporal characterisation of the pulse. Commonly used pulse measurement techniques such as autocorrelation give an estimate of the temporal duration of a pulse (without, however, being able to resolve fine temporal details in the pulse envelope structure), but are unable to make phase measurements.

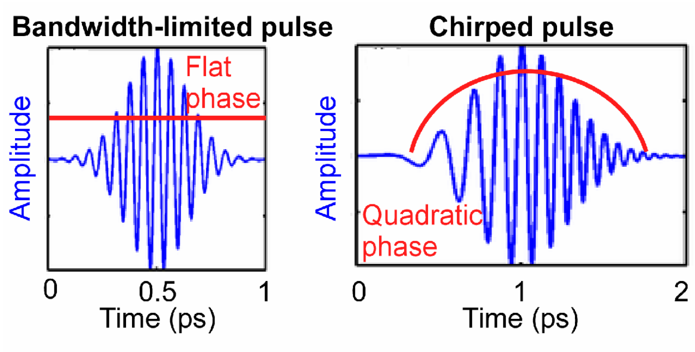

Fig. 1.10: Bandwidth-limited and chirped pulses. A bandwidth-limited pulse has the shortest possible temporal duration for a given spectral bandwidth and is characterised by a flat phase (shown in red). A chirped pulse has a longer temporal duration since the various frequency components have different group delays. This linear frequency chirp is equivalent to a quadratic phase across the pulse and arises from chromatic dispersion of the pulse during propagation in a dispersive medium.

There a number of requirements for a successful full-field characterisation technique for complex waveforms. Unambiguous measurement of the intensity envelope is necessary for accurate representation of complex and non-symmetric pulses. Single-shot operation (i.e. without the need for repetitive sampling) is also desirable in order to enable measurement of non-repetitive waveforms. A high record length-to-resolution ratio allows characterisation of long waveforms which also include sharp temporal features (in other words, with a high time-bandwidth product). Algorithm-free phase recovery is advantageous in order to minimise off-line processing and eliminate the problem of algorithm non-convergence.

Among the full-field measurement techniques that have been investigated, spectrally resolved measurements such as frequency-resolved optical gating (FROG) and its variants such as polarisation gating FROG and second-harmonic generation FROG [36-39] are popular, simultaneously yielding the pulse intensity and spectrum as functions of time. An iterative algorithm can then be applied to the spectrograms of many repeated measurements to determine the field amplitude and spectral phase. However this requirement for an iterative algorithm to recover amplitude and phase information means that FROG is not generally suitable for continual real-time measurements of non-repetitive waveforms. Another widely used class of techniques for ultrashort pulse measurement is spectral interferometry [40-42] where the signal pulse to be measured is interfered with a time-delayed reference pulse, with the resulting spectral interference pattern yielding the spectral phase. Spectral interferometry has the advantage of being very sensitive due to the absence of nonlinear gating, but the record length is limited by spectrometer resolution.

The temporal magnification or time lens approach to pulse measurement, which relies on the analogy between short pulse propagation and free-space diffraction [43], has been used to stretch optical waveforms to enable direct detection by conventional photodetectors [44, 45]. Additionally, phase recovery by heterodyne detection of the stretched signal pulse has been demonstrated [46]. However this technique is limited to a time window set by the stretched reference pulse duration. A recently developed technique know as optical arbitrary waveform measurement uses spectral slicing and digital coherent detection to achieve an extremely high record length-to-resolution ratio (>300,000) [47]. However the rather complicated arrangement requires a stable optical frequency comb as a reference and high resolution spectral filters.

Time-to-space conversion can achieve full-field measurement of ultrashort optical pulses by transferring the pulse's amplitude and phase information from the temporal domain to the spatial domain on a quasi-monochromatic SFG output wave. By performing the waveform measurement in the spatial domain much higher resolution can be obtained than is possible with a direct time domain measurement. The SFG wave can then be interfered with a narrow linewidth plane wave at the same centre wavelength to generate an interferogram, from which the time-dependant field amplitude and phase of the original pulse can be extracted. Time-to-space conversion has a number of attractive features for ultrashort pulse measurement, including single-shot operation, unambiguous and algorithm-free amplitude and phase measurement and a high record length to resolution ratio. In order to demonstrate the viability of time-to-space conversion for ultrashort pulse measurement, full-field measurement experiments performed on ultrashort pulses are presented in Chapter 4.

1.5 Laboratory apparatus and measurement techniques

The research conducted in this project involved measurement and manipulation of light in the time, frequency and spatial domains. The methods and equipment that were used can therefore be divided into three groups as follows.

1.5.1 Time domain

Implementation of time-to-space conversion experimentally required measurement of the relative time delay between the signal and reference pulses (100 fs duration) arriving at the spectral processor. This was done to ensure sufficient temporal overlap between the pulses at the nonlinear crystal in order to generate a detectable level of SFG power. A 125 MHz bandwidth InGaAs photodetector (sensitive to IR light) connected to a 12 GHz bandwidth oscilloscope was used to view the signal pulse to reference pulse separation and to optimise the temporal overlap.

In the full-field measurment experiments the SFG light carrying the time-to-space converted signal was mixed with a narrowband local oscillator (LO) to allow interferometric phase detection. Since the LO used did not come from a CW laser source, but instead was generated by spectrally filtering of the MLL residual pump pulses, it was necessary to achieve temporal overlap between the SFG and LO pulses at the camera or balanced photodetector in order to obtain intereference between them. A 9 GHz bandwidth GaAs photodetector (sensitive to near-IR light) was used together with the 12 GHz oscilloscope for this purpose.

For the real-time coherent detection experiment a free-space electro-optic phase modulator based on a KTP crystal was used to phase-modulate the signal pulses at 1550 nm with a sine wave at approximately 550 kHz. By homodyne mixing of the SFG light at 810 nm with the LO, this phase modulation was converted to a time-varying intensity incident on a 350 MHz bandwidth Si balanced photodetector. The 12 GHz oscilloscope was used view the phase-demodulated signal.

1.5.2 Frequency domain

The main instrument used for frequency domain measurements was an optical spectrum analyser (OSA), which displays the spectral power at each wavelength of the light under measurement. This is based on a diffraction grating and Fourier lens to spatially disperse the input light and a narrow slit which allows one spectral component to pass. Behind the slit is a photodiode which responds to light over the entire working range of the OSA. By continuously rotating the diffraction grating, one wavelength at a time passes through the slit and is incident on the photodiode. The photocurrent generated is proportional to the optical power incident on the photodiode and so the spectral power at each wavelength in turn is measured. In this way the spectrum of the input light is obtained.

Spectral measurements were made of the dispersed signal and reference light at the Fourier plane of the time-to-space spectral processor, in order to align the frequency components and ensure equal and opposite spatial dispersions, a prerequisite for time-to-space conversion. This was done by positioning the connecter end of a single mode fibre mounted on a micrometer stage at the Fourier plane and scanning transversely. The light entering the fibre was coupled into the OSA and so the spatial location of each frequency component was determined. The spectral resolution of the time-to-space processor (and hence the Rayleigh length of the focused spectral components) was also measured in this way.

The OSA was also used to record the spectrum of the narrow linewidth SFG light exiting the time-to-space convertor, as well as that of the local oscillator generated by spectral filtering of the MLL residual pump pulse. Finally the OSA was used to check for spatio-temporal coupling (angular dispersion and spatial chirp) of the signal pulses exiting the 4-pass pulse stretcher in the chirped pulse measurement experiment.

1.5.3 Spatial domain

For both the free-space and planar waveguide time-to-space conversion experiments, measurement and manipulation of the spatial modes of the signal, reference, SFG and LO beams were important in order to control the time-to-space conversion system parameters (i.e. time window and conversion efficiency) and to optimise performance.

Since the signal and reference beams were at wavelengths of 1550 nm and 1697 nm respectively an InGaAs camera was used for measurement of their spatial profiles. These were altered as necessary by beam expanders or condensers to obtain the required beam size at the input to the spectral processor. A CMOS camera was used for imaging the SFG light (and in particular the focused pulse images which are the output of the time-to-space conversion process) and also the LO light. In the slow phase detection experiments it was important to match the SFG and LO spatial modes at the camera in order to attain the best possible interference fringe contrast.

Finally, coupling of the dispersed signal and reference light into the planar PPLN waveguide required high numerical aperture (NA) imaging of their spatial modes which were tightly focused in the vertical direction. This was to obtain good mode matching to the guided modes in the planar waveguide, thus minimising insertion loss.

Chapter 2: High resolution and background-free time-to-space conversion

During this research project different time-to-space conversion experimental setups were investigated. These setups can be divided into two categories: free-space time-to-space conversion in bulk nonlinear crystal and guided-wave time-to-space conversion in a planar nonlinear waveguide. Experiments belonging to the first category are described in two papers presented in this chapter. Section 2.1 and paper 2A describe the demonstration of collinearly phase-matched and background-free time-to-space conversion in a beta barium borate (BBO) nonlinear crystal. Section 2.2 and paper 2B describe quasi phase-matched time-to-space conversion in periodically-poled lithium niobate crystal, resulting in an increased conversion efficiency slope.

2.1 Collinearly phase-matched, background-free time-to-space conversion in BBO nonlinear crystal

The first research task of this project was to demonstrate background-free time-to-space conversion with collinearly propagating signal and reference pulses in the nonlinear medium. Demonstration of collinearly phase-matched background-free time-to-space conversion in a bulk nonlinear medium is a necessary step prior to performing T-S conversion in nonlinear waveguides; the reason for this will be made clear in Chapter 3.1. Here the origin of background light in the time-to-space conversion process is explained and possible solutions are discussed.

Time-to-space conversion relies on the SFG interaction between signal and reference pulses inside a spectral processor to transfer information from the time to the space domains. However, in addition to the information-carrying SFG light produced due to the signal and reference pulse interaction, SHG light is also generated independently by the signal and reference beams in the nonlinear medium. This light does not contain any useful information on the temporal waveform envelopes or phase. However, it co-propagates with the SFG light and reaches the output image plane, where it forms a background to the focused pulse images and reduces the image quality at the camera or SNR at the photodetector array (see Fig. 2.1).

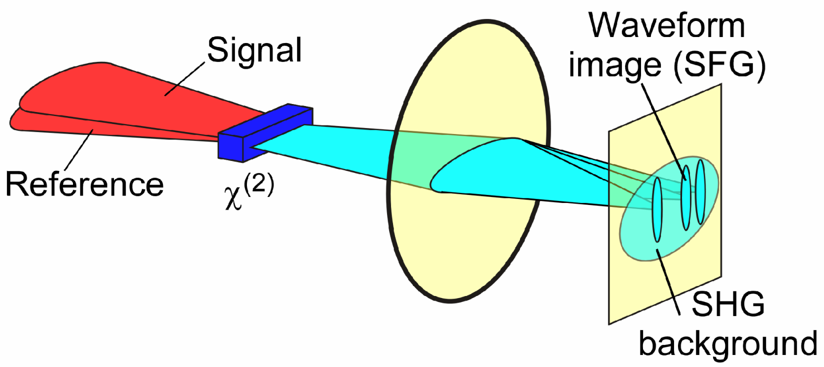

Fig. 2.1: Background SHG light. Whilst the SFG light is generated as a result of the interaction of the signal and reference pulses in the nonlinear medium, the SHG light is generated by each beam independently and so does not carry any useful temporal information. Instead it forms a background at the image plane and degrades the pulse image quality.

In order to eliminate the background SHG, non-collinearly propagating signal and reference beams have been used [13-15]. These are incident on the nonlinear crystal at crossed angles and so, due to phase-matching considerations which will be discussed below, the SFG light generated propagates along the bisector angle (i.e. the optical axis). The SHG light generated by the signal and reference beams propagates at an angle to the optical axis and so spatial filtering can be used to block this background light (see Fig. 2.2).

The disadvantage with this method is that the interaction length in the nonlinear crystal is limited by the non-collinear propagation of the signal and reference beams, resulting in lower conversion efficiency to SFG light. Moreover, this option is precluded by implementation of time-to-space conversion in nonlinear waveguides

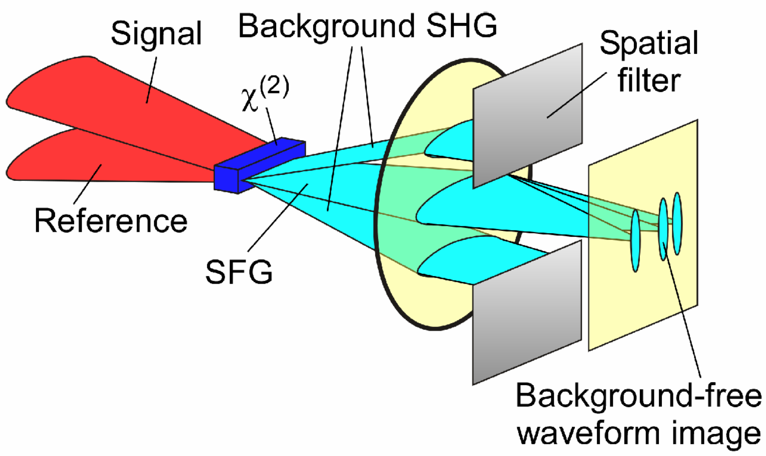

Fig. 2.2: Spatial filtering of background SHG light. The signal and reference beams enter the nonlinear crystal at crossed angles and so the SHG beams generated by each of them propagate in the same direction as the fundamental beams, whereas the SFG light generated by the signal and reference beam interaction propagates along the optic axis. A spatial filter then blocks the SHG and allows the SFG light through, resulting in a background-free time-to-space converted output image.

since the fundamental and generated beams necessarily co-propagate in the waveguides and also on emerging from them, making spatial filtering impossible. Therefore the solution chosen for this project was spectral filtering of the SHG background. In this case the signal and reference pulses are at non-degenerate central wavelengths and so the SHG light is generated at different wavelengths to the SFG light, enabling spectral filtering of the background with a band pass filter (see Fig. 2.3).

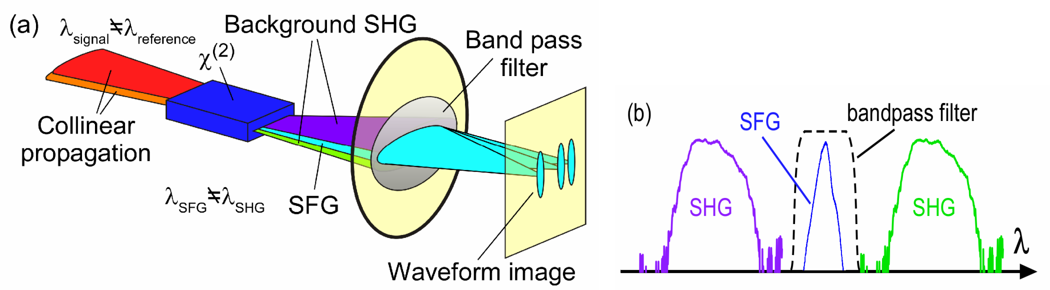

Fig. 2.3: Spectral filtering of background SHG light. (a) Co-propagating signal and reference beams at non-degenerate wavelengths enter the nonlinear crystal and generate SFG and background SHG light. The SFG light is generated at an intermediate wavelength with respect to the SHG wavelengths and so a band pass filter blocks the SHG background whilst passing the SFG light through to the image plane. Collinear propagation of the signal and reference beams results in a longer interaction length in the bulk nonlinear crystal. Since all beams (fundamental and generated) are co-propagating this solution is also applicable to guided wave time-to-space conversion. (b) A band pass filter centred at the SFG wavelength allows the SFG light through while blocking the SHG background light.

Implementation of this scheme in the laboratory necessitates two sources of ultrashort pulses at non-degenerate wavelengths. In the context of this research project the 'signal' pulses were chosen to be at 1550 nm wavelength. This wavelength is in the centre of the optical communications c-band (1530 nm to 1570 nm). This is the main transmission band used in long-haul optical communications, since absorption loss in optical fibre is relatively low at these wavelengths. The standard laboratory source for sub-ps pulses is the mode-locked titanium-sapphire (Ti:saph) solid-state laser, which emits ~100 fs pulses in the region of 800 nm. In order to convert these pulses to 1550 nm wavelength, an optical parametric oscillator (OPO) is used. This device is based on the optical nonlinear process of difference-frequency generation (see Chapter 1.1), which converts a short wavelength input beam to two longer wavelength output beams. By putting the nonlinear crystal (in this case LBO) in a resonant cavity, the conversion efficiency of the process is greatly increased. Since the OPO generates two beams (consisting of sub-ps pulse trains) at non-degenerate wavelengths, this can serve as the source for time-to-space conversion based on collinearly phase-matched

SFG. By choosing 1550 nm wavelength for the signal beam, the reference beam is automatically generated at 1697 nm. SFG between these two wavelengths in the time-to-space converter results in an output wave at 810 nm. This is not surprising since SFG is the inverse of the DFG interaction which occurs in the OPO and converts the Ti:saph laser 810 nm pulses to 1550 nm and 1697 nm pulses. The 810 nm wavelength of the output SFG light can be conveniently detected by CMOS cameras and silicon-based photodiodes.

Efficient SFG, like all 2^{nd} order nonlinear optics effects, relies on achieving good phase matching between the fundamental (in this case the signal and reference) waves and the generated wave. This means that the fundamental and generated waves should maintain a fixed phase relationship during propagation through the nonlinear medium. This is equivalent to fulfilling the conservation of momentum condition, since the product of the wavevector with propagation distance equals accumulated phase:

$$\Delta k = k_{SFG} - k_{sig} - k_{ref} = 0 \tag{2.1}$$

where Δk is the wavevector mismatch and $k_{SFG,\, sig,\, ref}$ are the SFG, signal and reference wavevectors respectively. If this condition is not satisfied energy flows continuously back and forth between the fundamental waves and the SFG, preventing the SFG field from building up to an appreciable value. In a dispersive medium (which is generally the case), the wavevector k varies nonlinearly with frequency due to the frequency dependent refractive index n:

$$k = n(\omega) \cdot \frac{\omega}{c} \tag{2.2}$$

where ω is the optical frequency and c is the speed of light in a vacuum. This chromatic dispersion means that the phase-matching condition in Eqn. 2.1 is generally not fulfilled (see Fig. 2.4) unless some particular measures are taken to satisfy it. One option is to use non-collinear phase matching where the signal and reference wavevectors are angled with respect to each other, such that their vector sum is equal to the SFG wavevector (as shown in Fig. 2.2).

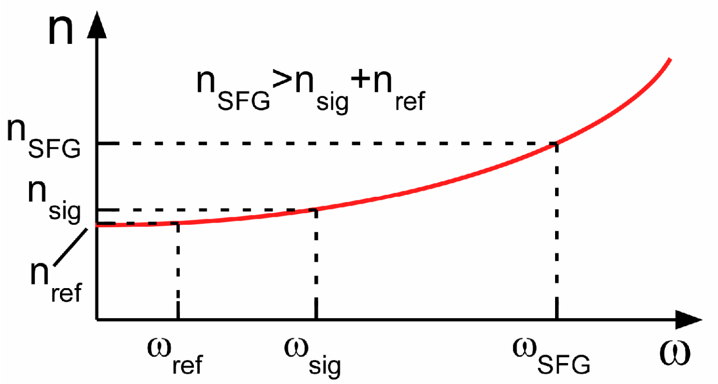

Fig. 2.4: Refractive index variation with frequency in a dispersive medium. The sum of the signal and reference refractive indices will generally be less than the SFG refractive index, resulting in a non-zero wavevector mismatch $\Delta k\neq 0$.

Another widely used technique is birefringent phase matching, which takes advantage of the polarisation dependant refractive indices of a birefringent nonlinear crystal. For a uniaxial birefringent crystal the refractive index experienced by light polarised parallel to the ordinary crystal axis is independent of the propagation direction, whereas light polarised parallel to the extraordinary axis will experience a different refractive index which also varies with propagation direction. By choosing a

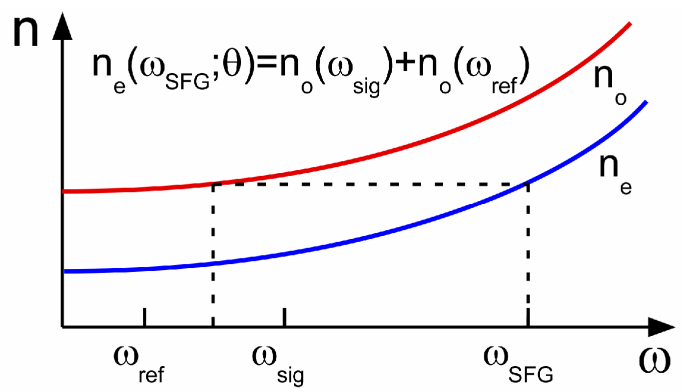

Fig. 2.5: Birefringent phase-matching. The signal and reference waves are polarised parallel to the ordinary axis of the birefringent crystal and so experience the ordinary refractive index n_0 (the red line). The SFG light is generated polarised parallel to the extraordinary axis, experiencing refractive index n_e (the blue line), and in a direction θ which satisfies the phase-matching condition. This is known as type I birefringent phase-matching (in type II phase-matching one of the fundamental beams is polarised along the ordinary axis and the other along the extraordinary axis).

suitable crystal and propagation direction the phase-matching condition in Eqn. 2.1 can be met (see Fig. 2.5). The angle between the propagation direction and the extraordinary axis of the crystal which satisfies the phase-matching condition is known as the phase-matching angle. Note that since refractive index is temperature dependent (via the thermo-optic effect), the phase-matching angle will vary with crystal temperature. The sensitivity of the phase-matching angle to fluctuations in temperature for a particular crystal is expressed as the thermal acceptance bandwidth.

A disadvantage of birefringent phase matching stems from spatial walkoff of the SFG beam with respect to the fundamental beams. This is due to the Poynting vector of light in an anisotropic medium, which gives the direction of energy flow, being generally non-parallel to the wavevector. This occurs for light polarised along the extraordinary axis and so causes the generated SFG light to propagate at an angle with respect to the fundamental beams (see Fig. 2.6). The resulting spatial walkoff limits the effective SFG interaction length between the interacting waves, thus reducing conversion efficiency. The spatial walkoff angle for the experiment using BBO described in paper 2A below was approximately 50 mrad.

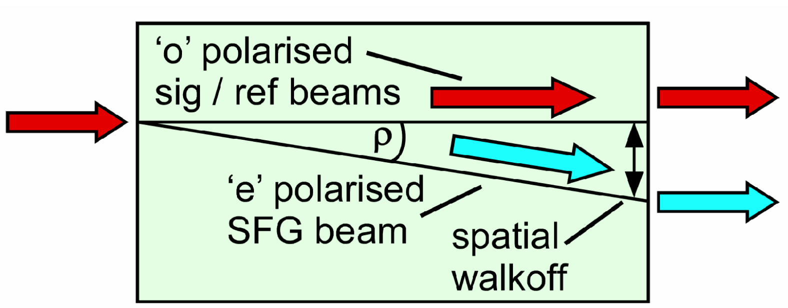

Fig. 2.6: Spatial walkoff. The anisotropy of the crystal results in an angle ρ between the SFG wavevector and its direction of energy flow. This causes spatial walkoff of the SFG beam from the fundamental beams, effectively limiting the interaction length.

The uniaxial birefringent nonlinear crystal BBO was chosen for the experiment presented in paper 2A due to the combination of reasonably high effective nonlinearity, wide phase matching bandwidth (enabling phase-matching of non-degenerate signal and reference light at widely spaced wavelengths), large thermal acceptance bandwidth (i.e. relative insensitivity of the phase-matching condition to temperature fluctuations) and high optical damage threshold. In addition, use of BBO allowed birefringent type I phase matching for the relevant wavelength range (from 1697 nm to 810 nm) at room temperature, obviating the need for a crystal oven. The

BBO crystal used was supplied by CASTECH, cut at an angle of 19.8° to the crystal z-axis (the extraordinary axis) for phase-matching, with an aperture of 8 mm × 8 mm and thickness of 1 mm in the light propagation direction. It was broadband anti-reflection (AR) coated from 1500 nm to 1750 nm on the input face and at 810 nm on the output face. The BBO crystal effective nonlinearity corresponding to the phase-matching angle of 19.8° used in the experiment was calculated as d_{eff} = 1.94 pm/V [48].

2.2 Time-to-space conversion in periodically-poled lithium niobate

Birefringent phase matching, as used for the time-to-space conversion experiment in BBO, suffers from the problem of spatial walkoff due to the orthogonally polarised fundamental and SFG waves in the birefringent nonlinear crystal. In addition, the use of orthogonally polarised light restricts the possible choices of nonlinear susceptibility tensor elements which can be exploited in the interaction. The strongest nonlinear susceptibility element of a given material may not be accessible, thus limiting the achievable conversion efficiency. This problem can be overcome by using a phase matching technique in which all interacting waves are parallel polarised along one of the crystal axes; the particular crystal axis to which the polarisation is aligned can then be chosen in order to obtain the highest possible nonlinearity. This arrangement is known as non-critical or temperature-tuned phase-matching, since the phase-matching condition must be satisfied via temperature tuning of the crystal refractive indices. However for a given set of interaction wavelengths the phase-matching temperature may be inconveniently high or in fact phase-matching may not be possible at all.

To overcome this difficulty a method known as quasi phase-matching (QPM) is often employed. Prior to use in a nonlinear interaction, the crystal structure is altered by the technique of periodic poling. In this case the spontaneous polarisation along one of the crystal axes is periodically inverted along the length of the crystal, successively reversing the sign of the nonlinear coefficient associated with that axis. The periodicity is chosen such that the phase-relation between the fundamental and generated waves is reset each time they become 180° out of phase after propagating a distance L_C known as the coherence length, as shown in Figure 2.7. The periodic poling creates a grating structure in the nonlinear crystal, whose grating wavevector k_G can then satisfy the phase-matching condition from Eqn 2.1:

$$\Delta k = k_{SFG} - k_{sig} - k_{ref} + k_G = 0 \tag{2.3}$$

where $k_G = 2\pi/\Delta$ and $\Delta = 2L_C$ is the domain length. As can be seen in Fig. 2.7, QPM allows a continual increase in SFG power along the crystal length (limited eventually by fundamental beam power depletion), although this increase is slower than would be the case for perfect phase-matching since the effective nonlinearity is reduced by a factor 2/π. However, correct choice of poling periodicity allows reasonably efficient SFG interactions between arbitrary wavelengths, subject to technological limitations on the poling procedure (for instance obtaining very small periodicity is difficult). Typically the direction of the nonlinear coefficient is reversed by applying a high electric field across the crystal. This causes a permanent reversal of the crystal axis and, by fabricating a series of electrodes on the crystal surface, a high voltage can be applied to pole the crystal with the desired periodicity.

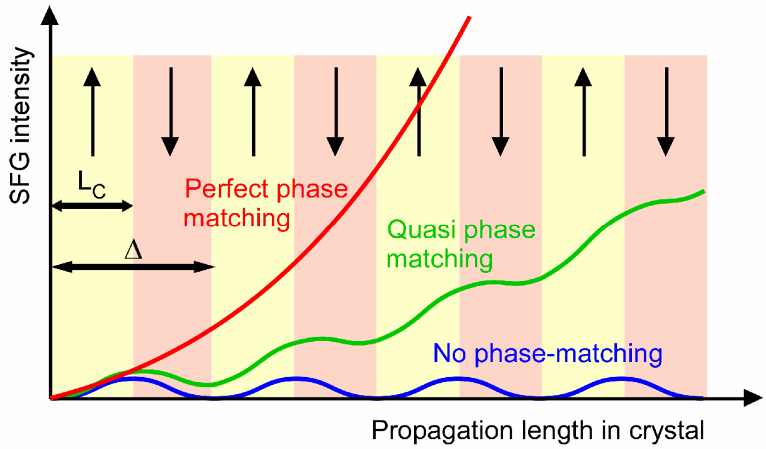

Fig. 2.7: Quasi phase-matching in a periodically-poled nonlinear crystal. Conversion efficiencies of phase-matched, quasi phase-matched and non phase-matched SFG are compared as a function of propagation length in the nonlinear crystal. The coherence length L_C is the distance over which the fundamental and generated waves become 180° out of phase and the domain length $\Delta = 2L_C$. The shaded background indicates individual domains and the arrows indicate the poling direction of the nonlinear coefficient.

One of the most widespread nonlinear crystals used for QPM is lithium niobate. Lithium niobate has a high nonlinear coefficient of d_{eff} = 25 pm/V for light at 1550 nm polarised along the crystal z-azis [49]. This nonlinearity is reduced to 16 pm/V by the 2/π factor due to periodic poling; however it is still significantly higher than the BBO effective nonlinearity of 1.94 pm/V. Since the SFG power generated depends on the square of d_{eff}, the use of PPLN resulted in a large increase in conversion efficiency slope (see paper 2B below). The periodically-poled lithium niobate (PPLN) chip used in the experiment had a domain length of 20.3 μm (due to the specific wavelengths of the signal and reference beams used and according to Eqn. 2.3) and dimensions of 10 mm × 6 mm × 0.5 mm in the spatial dispersion, light propagation and vertical directions respectively (see Fig. 2.8). In addition the input face had broadband AR-coating in the range 1500 nm to 1750 nm and the output face was AR-coated at 810 nm. This was in order to minimise back-reflections of the input signal and reference beams from the front face of the crystal and back-reflection of the generated SFG

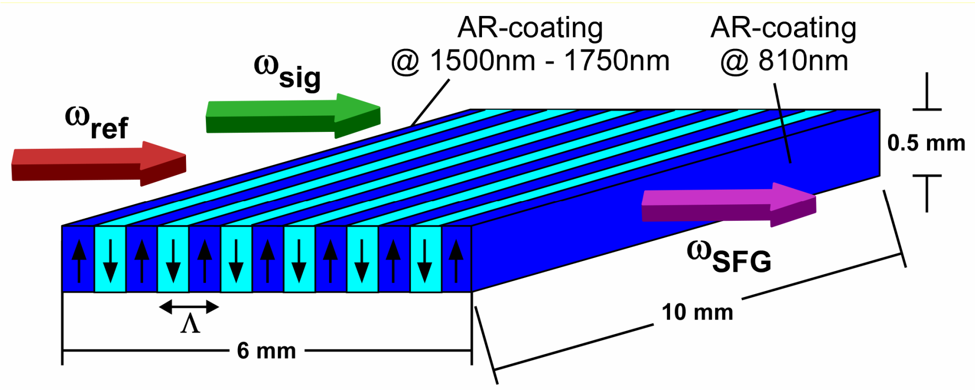

Fig. 2.8: Periodically-poled lithium niobate (PPLN) nonlinear crystal. The physical dimensions of the PPLN chip used in time-to-space conversion experiment are shown (not to scale).

light from the back face of the crystal (lithium niobate has a relatively high refractive index of 2.2). This PPLN chip was fabricated by Harald Herrmann and co-workers from the Integrated Quantum Optics group at the Department of Applied Physics, University of Paderborn in Germany. In addition another chip was fabricated with the same dimensions but with a periodicity of 20.5 μm, to allow testing of different QPM periods for optimisation of the conversion efficiency. A home-made oven was used for control and stabilisation of the PPLN temperature; the temperature for optimum phase-matching was determined experimentally to be 165 °C for the 20.3 μm periodicity chip.

The time-to-space experiment in bulk PPLN (presented in Chapter 2B) resulted in a large increase (by a factor 60) of the conversion efficiency slope compared with that obtained using BBO (as detailed in Chapter 2A). This increase was due to the higher effective nonlinearity of PPLN. At the same time the high resolution of the time-to-space converted image was maintained, with a serial-to-parallel resolution factor *N* of 95 and a time window of 42 ps. Figure 2.9 shows a photograph of the central part of the bulk PPLN crystal time-to-space setup; the BBO setup and also the experimental setups presented in later chapters were broadly similar, with some changes in the optical elements used.

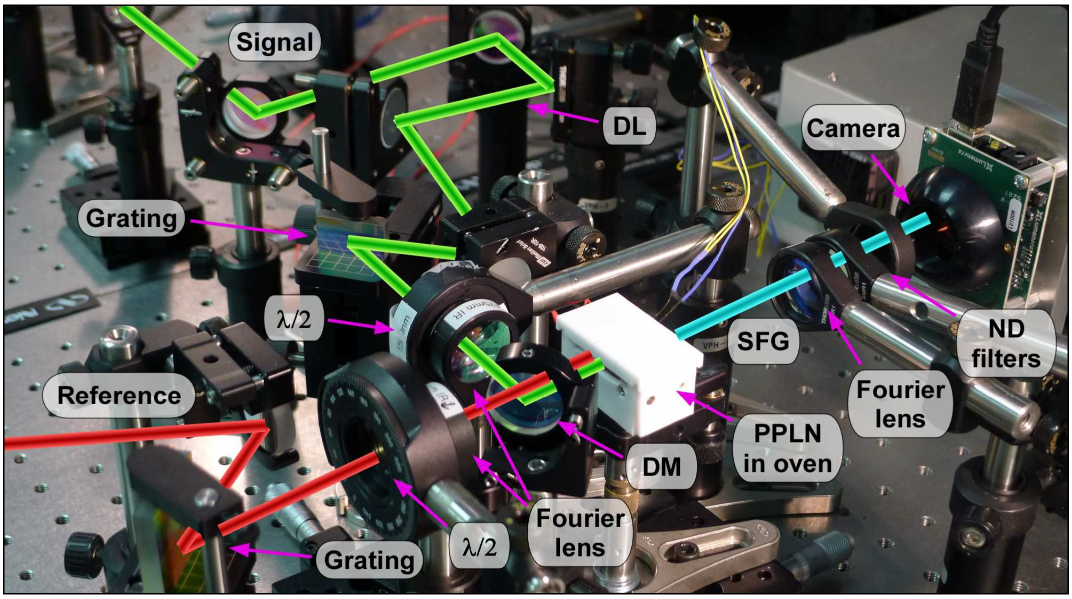

Fig. 2.9: Bulk PPLN time-to-space conversion setup. This photograph shows the central part of the time-to-space conversion setup in the laboratory. The signal, reference and SFG beam paths are marked in green, red and blue respectively. The signal and reference beams enter from the top left and left of the picture and are directed onto separate diffraction gratings, with the signal beam first passing through an optical delay line (DL). The dispersed beams then pass through half-waveplates ($\lambda/2$) to align their polarisations to the PPLN z-axis. The spectral components of each dispersed beam are then focused by Fourier lenses and made co-propagating by a dichroic mirror (DM), which transmits the reference beam (long wavelength) and reflects the signal beam (shorter wavelength). The signal and reference spatially resolved spectra are focused into a bulk PPLN nonlinear crystal which is located inside the white temperature control oven. The SFG beam that is generated is focused by another Fourier lens onto the output image plane, where the focused pulse image is recorded by a CMOS camera. Neutral density (ND) attenuation filters are used to avoid saturation of the camera.

Chapter 2A

High-resolution, background-free, time-to-space conversion by collinearly phase-matched sum-frequency generation

Dror Shayovitz and Dan M. Marom

Published in Optics Letters:

D. Shayovitz and D. M. Marom, "High-resolution, background-free, time-to-space conversion by collinearly phase-matched sum-frequency generation," Opt. Lett. **36**, 1957-1959 (2011)

High-resolution, background-free, time-to-space conversion by collinearly phase-matched sum-frequency generation

Dror Shayovitz and Dan M. Marom*

Department of Applied Physics, Hebrew University of Jerusalem, Jerusalem 91904, Israel
**Corresponding author: danmarom@cc.huji.ac.il*

Received March 17, 2011; revised April 20, 2011; accepted April 22, 2011;
posted April 22, 2011 (Doc. ID 144400); published May 20, 2011

We report the first demonstration, to our knowledge, of time-to-space conversion of 1.55 μm femtosecond optical pulses using nondegenerate, collinearly phase-matched sum-frequency generation. A quasi-monochromatic and background-free output signal spanning a time window of 35 ps and with a pulse image width of 350 fs was achieved. The resulting serial-to-parallel resolution factor of 100 demonstrates the potential for all-optical complete frame demultiplexing of a 1 Tbit/s optical time-division multiplexing bit stream.
OCIS codes: 320.7085, 190.4223, 060.4230.

The use of optical time-division multiplexing (OTDM) in high-speed optical communications is a possible solution to the challenge of supporting ever-increasing capacity requirements while avoiding the overhead costs associated with high channel-count wavelength-division multiplexed systems. A recent demonstration of 5.1 Tbit/s data transmission achieved at 1.28 Tbaud/s signaling with phase-shift keying (PSK) [1] demonstrates the bandwidth efficiency potential of coherent detection OTDM. However, signal recovery at Tbit/s bit rates poses a serious challenge, because available optoelectronic receivers are limited to electrical bandwidths of 50–100 GHz. A solution that has attracted much attention is all-optical demultiplexing using fast optical nonlinearities.

Time-to-space conversion [2–8] is a real-time optical demultiplexing technique that utilizes sum-frequency generation (SFG) between a frame of signal pulses and a reference pulse to convert a fast serial OTDM pulse stream to a number of slower spatially parallel channels, which can then be directly detected by an array of optoelectronic receivers. Key advantages of this technique are the strong $\chi^{(2)}$ nonlinearity of certain nonlinear crystals and the preservation of phase information for compatibility with advanced modulation formats such as PSK. Time-to-space conversion has been demonstrated in the optical communications band [8], but with relatively low conversion efficiency. A limiting factor on the conversion efficiency is the short interaction length of two crossed beams in noncollinear phase-matching, which is required to provide a background-free output signal. One way to improve the conversion efficiency is to use birefringent phase-matching with copropagating beams, thus increasing the interaction length up to the focused beams' confocal length. However, in the collinear configuration, the information-bearing SFG signal is superimposed over the second harmonic generation (SHG) background light from the signal and reference pulses independently and will coherently interfere with it.

In this Letter, we report the first (to our knowledge) demonstration of time-to-space conversion by means of collinear nondegenerate wave mixing with a background-free output image. By employing nondegenerate wavelength mixing, the SFG product is generated at a different wavelength from the two SHG background components. Spectral filtering of the generated light then provides a background-free output signal. Detailed analyses of the operation of a time-to-space conversion processor are provided in [2,3,7] and briefly summarized here. A sequence of input signal pulses (a "frame") and the locally generated reference pulse both enter the processor. Each of these waveforms is then spatially dispersed in opposite directions with a grating and lens combination, so that the high-frequency components of the signal waveform spatially overlap the low-frequency components of the reference pulse, and vice versa. A nonlinear crystal is located at the Fourier plane where the dispersed light is spatially resolved. SFG between the spectral components at every spatial location results in a quasi-monochromatic upconverted wave. This generated wave contains a linear phase tilt across the beam that is proportional to the time delay between each signal pulse in the frame and the reference pulse. A spatial Fourier transform by an output lens converts this phase tilt to a spatial translation at the image plane, resulting in a

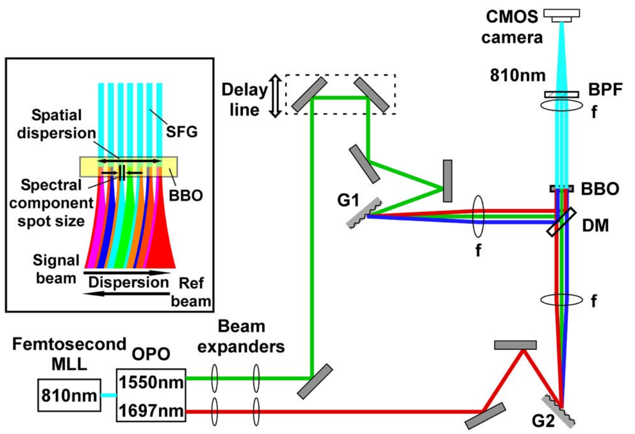

Fig. 1. (Color online) Experimental setup (MLL, mode-locked laser; OPO, optical parametric oscillator; G1/G2, grating; f, Fourier lens; DM, dichroic mirror; BBO, beta barium borate nonlinear crystal; BPF, bandpass filter. Inset: collinear, oppositely dispersed signal and reference beams at the nonlinear crystal.

0146-9592/11/111957-03$15.00/0

Table 1. Input Beam Characteristics of Time-to-Space Converter[a]

	λ_0(nm)	f_g (lp/mm)	α (°)	$dx/d\omega$ (μm/GHz)	w_0 (μm)	P_{av}/P_{max}(mW/kW)
Signal	1550	1100	70.0	–0.16	13	215/27
Ref.	1697	1000	79.8	0.16	14	85/11

[a] λ_0, central wavelength; f_g, grating frequency; α, angle of incidence on grating; $dx/d\omega$, spatial dispersion; w_0, focused spot radius of single spectral component; P_{av}/P_{max}, average beam power/peak power at crystal. Ideally the reference beam power would be higher than the signal power.

transverse spatial pattern that is the direct image of the input signal waveform.

Figure 1 shows our experimental setup. The signal (at 1550 nm) and idler (at 1697 nm) outputs of a Spectra-Physics Opal (Newport Corporation, USA) optical parametric oscillator (with FWHM pulse duration of 100 fs and repetition rate of 80.2 MHz) are expanded to appropriate collimated beam sizes and undergo equal but opposite linear spatial dispersions by diffraction gratings G1 and G2 and 75 mm Fourier lenses. The two dispersed beams are superimposed by a long-pass dichroic mirror (DM) and are incident on a 1 mm-thick beta barium borate (BBO) nonlinear crystal located at the focal plane. The confocal length of the focused signal and reference beams in the plane of dispersion was calculated as 1.1 mm (per spectral component). The relevant beam characteristics are listed in Table 1.

Because of the matched yet flipped spatial dispersions of the signal and reference beams at the BBO crystal, Type I phase-matched SFG at each point in space results in a quasi-monochromatic output beam at 810 nm. An output lens of focal length 75 mm coherently focuses the light to a narrow line at the Fourier plane, where a CMOS camera records the output spatial image. The SFG –3 dB bandwidth was measured as 0.22 nm (= 100 GHz) centered at 810 nm by coupling focused output light into a multimode fiber connected to an optical spectrum analyzer (Fig. 2). This narrow signal bandwidth demonstrates compatibility with optoelectronic receivers and also the possibility of mixing the SFG signal with a CW local oscillator at the same wavelength to extract phase information. Background second harmonic light at 775 nm and 849 nm is blocked by a bandpass filter (central wavelength 810 nm, –3 dB bandwidth 10 nm) placed between the lens and the camera.

The key performance parameters of the time-to-space converter are the serial-to-parallel resolution factor N and the conversion efficiency η. The serial-to-parallel resolution factor N is defined as the ratio of the time window, ΔT (which limits the maximum extent of the output spatial pattern), to the width of an individual pulse image, τ, and determines the maximum number of pulses that can be simultaneously demultiplexed to separate spatial channels. The conversion efficiency η is defined as the SFG output power divided by the signal beam power incident on the nonlinear crystal. The resolution–conversion efficiency product is invariant to the spot size, w_0, of a spectral component focused at the crystal, so that one can be improved at the expense of the other. However, N is dictated by the application and, for demultiplexing a 1 Tbit/s OTDM signal down to electrical bandwidths, should be between 40 and 100.

The time-to-space conversion factor and the time window were measured by varying the time delay between the signal and reference pulses (Fig. 3). A linear fit to the time-delay-dependent pulse image position data results in a time-to-space conversion factor of 60 μm/ps. A Gaussian curve was fitted to the time-delay-dependent pulse image intensity data giving a FWHM time window of 35 ps. The conversion efficiency was calculated by measuring the SFG output power with a power meter placed after the bandpass filter and dividing by the signal beam power incident on the BBO crystal at zero time delay (peak efficiency). The linear conversion efficiency slope was measured as 11.2×10^{-5} per watt of reference beam power and the maximum conversion efficiency obtained was 0.9×10^{-5} at 85 mW reference beam power. This low conversion efficiency is primarily due to the low reference beam power available in our setup and is also due to the spatial walkoff (48.9 mrad) limited interaction length in the BBO crystal. Note that the spatial walkoff limitation can be overcome by using noncritical phase-matching [3] or quasi-phase-matching [8]. Because we are operating in the linear conversion regime (i.e., with nondepleting pump power), we would benefit from

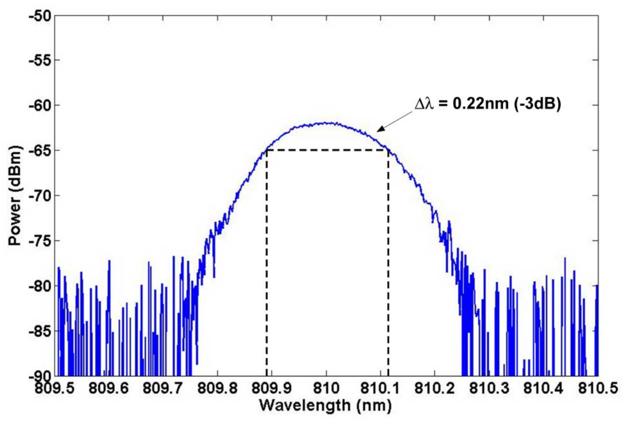

Fig. 2. (Color online) SFG narrowband spectrum centered at 810 nm with a –3 dB bandwidth of 0.22 nm (= 100 GHz).

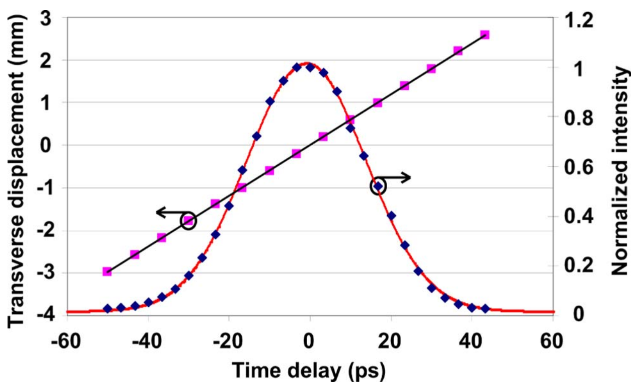

Fig. 3. (Color online) Variation of pulse image position and intensity as a function of time delay, showing linear and Gaussian fits, respectively.

Table 2. Calculated and Measured Time-to-Space Conversion Parameters[a]

	$\Delta x/\Delta t$ (μm/ps)	ΔT (ps)	τ (ps)	N	η (%)
Predicted	57	34	0.15	227	1.7×10^{-3}
Measured	60	35	0.35	100	0.9×10^{-3}

[a] $\Delta x/\Delta t$, time-to-space conversion factor; ΔT, FWHM time window; τ, FWHM pulse image width; N, serial-to-parallel resolution factor; η, conversion efficiency.

a more intense reference pulse. The results are summarized and compared with the theoretically calculated parameters in Table 2.

The time-to-space converted pulse image width τ was estimated by fitting a Lorentzian curve to a pulse image at the center of the time window, with the resulting FWHM corresponding to 350 fs. Note that because the signal and reference pulses are of the same duration, an autocorrelation factor of 1.5 has been included in the values of the theoretical time window and pulse image width. It can be seen that the measured pulse image width is more than twice as long as the predicted value. We attribute this loss of resolution to a narrowing of the phase-matched bandwidth due to distortions in the dispersed reference beam spectrum, which result from the asymmetric spatial profile of the reference beam incident on the diffraction grating. This reduction in the SFG interaction bandwidth results in a less spectrally resolved SFG output beam and therefore a less tightly focused pulse image.

Despite this, the high time-to-space conversion resolution of $N = 100$ demonstrates the potential for 1-to-50 demultiplexing of subpicosecond pulses with low interchannel cross talk. As a demonstration, a series of 35 pulse images equally spaced throughout the 35 ps time window (equivalent to 1 THz OTDM baud rate) was recorded [Figs. 4(a) and 4(b)]. In addition to the time-delay-dependent intensity of the output image, it is noted that there is a defocusing effect toward one side of the time window [the right-hand side in Figs. 4(a) and 4(b)]. We attribute this again to an asymmetry in the spectral profile of the dispersed reference beam. This spectral asymmetry results in a more limited range of phase-matched signal and reference frequency components toward one side of the time window, giving a less tightly focused output image. It may be possible to correct this distortion by spatially filtering the reference beam before it reaches the diffraction grating, at the expense of reference beam power.

The important innovation of our work is the implementation of background-free, high-resolution time-to-space conversion using nondegenerate, collinearly phase-matched SFG. This opens the way to a further advance by employing quasi-phase-matching in a periodically poled lithium niobate crystal, thus overcoming the spatial walkoff limitation on the interaction length and increasing the conversion efficiency.

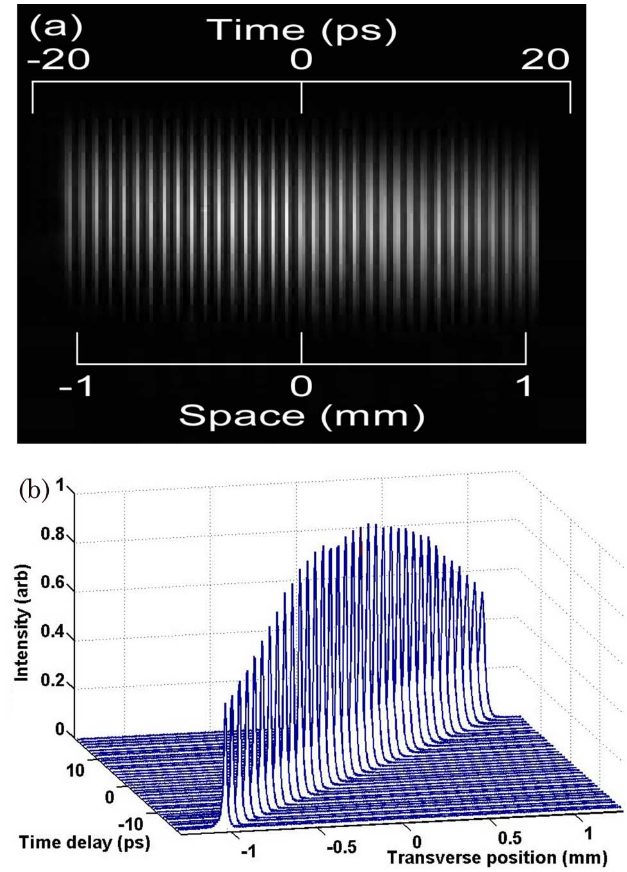

Fig. 4. (Color online) (a) 35 pulse spatial images representing a synthetic 1 Tbit/s data stream (composite image) and (b) variation in pulse image intensity and transverse position as the time delay is varied throughout the time window.

The authors gratefully acknowledge the support of The Peter Brodje Center for Innovative Engineering.

References

1. H. C. H. Mulvad, M. Galili, L. Oxenlowe, H. Hu, A. T. Clausen, J. B. Jensen, C. Peucheret, and P. Jeppesen, Opt. Express **18**, 1438 (2010).
2. P.-C. Sun, Y. T. Mazurenko, and Y. Fainman, J. Opt. Soc. Am. A **14**, 1159 (1997).
3. A. M. Kan'an and A. M. Weiner, J. Opt. Soc. Am. B **15**, 1242 (1998).
4. K. Oba, P.-C. Sun, Y. T. Mazurenko, and Y. Fainman, Appl. Opt. **38**, 3810 (1999).
5. J. Ishi, H. Kunugita, T. Ban, T. Kondo, and K. Ema, Appl. Phys. Lett. **77**, 3487 (2000).
6. D. M. Marom, D. Panasenko, P.-C. Sun, and Y. Fainman, IEEE J. Sel. Top. Quantum Electron. **7**, 683 (2001).
7. D. M. Marom, D. Panasenko, P.-C. Sun, Y. T. Mazurenko, and Y. Fainman, J. Opt. Soc. Am. A **18**, 448 (2001).
8. J.-H. Chung and A. M. Weiner, J. Lightwave Technol. **21**, 3323 (2003).

Chapter 2B

High resolution time-to-space conversion of sub-picosecond pulses at 1.55μm by non-degenerate SFG in PPLN crystal

Dror Shayovitz, Harald Herrman, Wolfgang Sohler, Raimund Ricken, Christine Silberhorn and Dan M. Marom

Published in Optics Express:

D. Shayovitz, H. Herrman, W. Sohler, R. Ricken, C. Silberhorn and D. M. Marom, "High resolution time-to-space conversion of sub-picosecond pulses at 1.55μm by non-degenerate SFG in PPLN crystal," Opt. Exp. **24**, 27388-27395 (2012)

High resolution time-to-space conversion of sub-picosecond pulses at 1.55μm by non-degenerate SFG in PPLN crystal

Dror Shayovitz[1,*] Harald Herrmann,[2] Wolfgang Sohler,[2] Raimund Ricken,[2] Christine Silberhorn,[2] and Dan M. Marom[1]

[1]*Department of Applied Physics, Hebrew University of Jerusalem, Jerusalem, 91904, Israel*
[2]*Department of Applied Physics, The University of Paderborn, Warburger Str. 100 D-33098, Paderborn, Germany*
[*]*dror.shayovitz@mail.huji.ac.il*

Abstract: We demonstrate high resolution and increased efficiency background-free time-to-space conversion using spectrally resolved non-degenerate and collinear SFG in a bulk PPLN crystal. A serial-to-parallel resolution factor of 95 and a time window of 42 ps were achieved. A 60-fold increase in conversion efficiency slope compared with our previous work using a BBO crystal [D. Shayovitz and D. M. Marom, Opt. Lett. **36**, 1957 (2011)] was recorded. Finally the measured 40 GHz narrow linewidth of the output SFG signal implies the possibility to extract phase information by employing coherent detection techniques.

OCIS codes: (190.0190) Nonlinear optics; (320.0320) Ultrafast optics; (060.0060) Fiber optics and optical communications.

References and links

1. T. Richter, E. Palushani, C. Schmidt-Langhorst, R. Ludwig, L. Molle, M. Nolle, and C. Schubert, "Transmission of single-channel 16-QAM data signals at terabaud symbol rates," J. Lightwave Technol. **30**(4), 504–511 (2012).
2. B. C. Wang, V. Baby, W. Tong, L. Xu, M. Friedman, R. J. Runser, I. Glesk, and P. R. Prucnal, "A novel fast optical switch based on two cascaded Terahertz Optical Asymmetric Demultiplexers (TOAD)," Opt. Express **10**(1), 15–23 (2002).
3. H. Le Minh, Z. Ghassemlooy, and W. Pang Ng, "Characterization and performance analysis of a TOAD switch employing a dual pulse scheme in high-speed OTDM demultiplexer," IEEE Commun. Lett. **12**(4), 316–318 (2008).
4. J. Du, Y. Dai, G. K. P. Lei, and C. Shu, "Reconfigurable two-channel demultiplexing using a single baseband control pulse train in a dispersion asymmetric NOLM," Opt. Express **18**(18), 18691–18696 (2010).
5. K. I. Kang, I. Glesk, T. G. Chang, P. R. Prucnal, and R. K. Boncek, "Demonstration of all-optical Mach-Zehnder demultiplexer," Electron. Lett. **31**(9), 749–750 (1995).
6. T. Miyazaki and F. Kubota, "Simultaneous demultiplexing and clock recovery for 160-Gb/s OTDM signal using a symmetric Mach-Zehnder switch in electrooptic feedback loop," IEEE Photon. Technol. Lett. **15**(7), 1008–1010 (2003).
7. T. Hirooka, M. Okazaki, T. Hirano, P. Guan, M. Nakazawa, and S. Nakamura, "All-optical demultiplexing of 640-Gb/s OTDM-DPSK signal using a semiconductor SMZ switch," IEEE Photon. Technol. Lett. **21**(20), 1574–1576 (2009).
8. E. S. Awad, P. S. Cho, N. Moulton, and J. Goldhar, "All-optical timing extraction with simultaneous opyical demultiplexing from 40 Gb/s using a single electroabsorption modulator," IEEE Photon. Technol. Lett. **15**(1), 126–128 (2003).
9. A. Cheng, M. P. Fok, and C. Shu, "All-optical tunable delay line for channel selection in OTDM demultiplexing," in *Asia Optical Fiber Communication and Optoelectronic Exposition and Conference*, OSA Technical Digest (CD) (Optical Society of America, 2008), paper SuA3. *http://www.opticsinfobase.org/abstract.cfm?URI=AOE-2008-SuA3*
10. F. Li, M. Pelusi, D.-X. Xu, A. Densmore, R. Ma, S. Janz, and D. J. Moss, "Error-free all-optical demultiplexing at 160Gb/s via FWM in a silicon nanowire," Opt. Express **18**(4), 3905–3910 (2010).
11. B. Corcoran, M. D. Pelusi, C. Monat, J. Li, L. O'Faolain, T. F. Krauss, and B. J. Eggleton, "Ultracompact 160 Gbaud all-optical demultiplexing exploiting slow light in an engineered silicon photonic crystal waveguide," Opt. Lett. **36**(9), 1728–1730 (2011).
12. C. Koos, P. Vorreau, T. Vallaitis, P. Dumon, W. Bogaerts, R. Baets, B. Esembeson, I. Biaggio, T. Michinobu, F. Diedrich, W. Freude, and J. Leuthold, "All-optical high-speed signal processing with silicon-organic hybrid slot waveguides," Nat. Photonics **3**(4), 216–219 (2009).

#175578 - $15.00 USD Received 5 Sep 2012; revised 27 Oct 2012; accepted 28 Oct 2012; published 19 Nov 2012

13. M. Galili, J. Xu, H. C. Mulvad, L. K. Oxenløwe, A. T. Clausen, P. Jeppesen, B. Luther-Davis, S. Madden, A. Rode, D.-Y. Choi, M. Pelusi, F. Luan, and B. J. Eggleton, "Breakthrough switching speed with an all-optical chalcogenide glass chip: 640 Gbit/s demultiplexing," Opt. Express **17**(4), 2182–2187 (2009).
14. R. Takahashi, T. Yasui, J. Seo, and H. Suzuki, "Ultrafast all-optical serial-to-parallel convertors based on spin-polarized surface-normal optical switches," IEEE J. Sel. Top. Quantum Electron. **13**(1), 92–103 (2007).
15. T. Nakahara, H. Takenouchi, R. Urata, H. Yamazaki, and R. Takahashi, "Hybrid optoelectronic buffer using CMOS memory and optical interfaces for 10-Gbit/s asynchronous variable-length optical packets," Opt. Express **18**(20), 20565–20571 (2010).
16. Y. Oshita, T. Konishi, and Y. Ichioka, "Ultrafast time-to-two-dimensional-space conversion system usng SHG crystal," Opt. Rev. **9**(4), 141–145 (2002).
17. Y. Oshita, T. Konishi, W. Yu, K. Itoh, and Y. Ichioka, "Application of ultrafast time-to-two-dimensional-space-to-time conversion (II): time-varying spectral control for arbitrary ultrafast signal reshaping," IEEE Photon. Technol. Lett. **16**(2), 623–625 (2004).
18. M. A. Foster, R. Salem, D. F. Geraghty, A. C. Turner-Foster, M. Lipson, and A. L. Gaeta, "Silicon-chip-based ultrafast optical oscilloscope," Nature **456**(7218), 81–84 (2008).
19. K. G. Petrillo and M. A. Foster, "Scalable ultrahigh-speed optical transmultiplexer using a time lens," Opt. Express **19**(15), 14051–14059 (2011).
20. E. Palushani, H. C. Hansen Mulvad, M. Galili, H. Hu, L. K. Oxenlowe, A. T. Clausen, and P. Jeppesen, "OTDM-to-WDM conversion based on time-to-frequency mapping by time-domain optical Fourier transformation," IEEE J. Sel. Top. Quantum Electron. **18**(2), 681–688 (2012).
21. H. Hu, J. Yu, L. Zhang, A. Zhang, W. Wang, J. Wang, Y. Jiang, and E. Yang, "40Gb/s all-optical serial-to-parallel conversion based on a single SOA," IEEE Photon. Technol. Lett. **20**(13), 1181–1183 (2008).
22. P.-C. Sun, Y. T. Mazurenko, and Y. Fainman, "Femtosecond pulse imaging: ultrafast optical oscilloscope," J. Opt. Soc. Am. A **14**(5), 1159–1170 (1997).
23. A. M. Kan'an and A. M. Weiner, "Efficient time-to-space conversion of femtosecond optical pulses," J. Opt. Soc. Am. B **15**(3), 1242–1245 (1998).
24. D. M. Marom, D. Panasenko, P.-C. Sun, and Y. Fainman, "Linear and nonlinear operation of a time-to-space processor," J. Opt. Soc. Am. A **18**(2), 448–458 (2001).
25. J.-H. Chung and A. M. Weiner, "Real-time detection of femtosecond optical pulse sequences via time-to-space conversion in the lightwave communications band," J. Lightwave Technol. **21**(12), 3323–3333 (2003).
26. D. Shayovitz and D. M. Marom, "High-resolution, background-free, time-to-space conversion by collinearly phase-matched sum-frequency generation," Opt. Lett. **36**(11), 1957–1959 (2011).
27. D. Shayovitz, H. Herrmann, W. Sohler, R. Ricken, C. Silberhorn, and D. M. Marom, "High resolution time-to-space conversion of sub-picosecond pulses at 1.55µm by non-degenerate SFG in PPLN crystal," in *Nonlinear Photonics,* OSA Technical Digest (online) (Optical Society of America, 2012), paper NM3C.2. *http://www.opticsinfobase.org/abstract.cfm?URI=NP-2012-NM3C.2*

1. Introduction

Optical communications networks are subject to ever increasing capacity demands due to the rapid growth in internet traffic. Two principle approaches in support of these demands are increasing parallelism using wavelength division multiplexing (WDM), filling the gain bandwidth of optical amplifiers, and increasing bandwidth efficiency using advanced modulation formats such as phase-shift keying (PSK). WDM channel reduction is desirable and may be enabled by boosting the serial transmission rate to higher baud rates. This can be achieved by optical time division multiplexing (OTDM) where short pulses are electrooptically modulated at relatively low bandwidths (10's of GHz) and then interleaved into a single high speed serial channel using passive optical delay lines. A recent demonstration of 10.2 Tbit/s data transmission achieved by 1.28 Tbaud/s multiplexing together with 16-QAM (quadrature amplitude modulation) [1] underlines the potential of OTDM for maximizing single wavelength channel data capacity by combining a high symbol rate and multiple bits-per-symbol modulation.

Whilst generating the OTDM channel is relatively straightforward, detection after transmission is more challenging. Direct or coherent optoelectronic detection of terabaud OTDM is not possible due to electric circuit bandwidth limitations. Generally all-optical demultiplexing using a fast nonlinear optical interaction is required; examples include the nonlinear optical loop mirror switch [2–4], the semiconductor optical amplifier based Mach-Zehnder switch [5–7], cross-absorption modulation [8,9] and four-wave mixing in silicon, silicon-organic hybrid or chalcogenide $\chi^{(3)}$ nonlinear waveguides [10–13]. While each technique has its own advantages and disadvantages, their operation principles limit them to single sub-channel (tributary) extraction from the OTDM channel. The result is that the number of devices required to fully demultipex the incoming data stream, and hence also

#175578 - $15.00 USD Received 5 Sep 2012; revised 27 Oct 2012; accepted 28 Oct 2012; published 19 Nov 2012

power consumption, scales with the OTDM channel baud rate. The need for multiple devices leads to the even more serious problem of inter-device timing synchronization, which becomes critical at rates of 100's Gbaud/s and higher.

These problems can be overcome using serial-to-parallel conversion where a single device simultaneously demultiplexes all tributaries out of the OTDM channel, resulting in parallel lower bandwidth output channels which can then be detected optoelectronically. Examples include multiple quantum well based time-to-space conversion [14, 15], angle phase-matched time-and-frequency-to-two-dimensional-space conversion [16, 17], time-to-frequency conversion based on four-wave mixing [18–20] or semiconductor optical amplifier based cross-phase modulaton [21] and spectrally resolved sum-frequency generation (SFG) time-to-space conversion [22–27]. Serial-to-parallel demultiplexing avoids the problem of inter-device clock synchronization and is robust against detection errors due to timing jitter in the transmitted pulse stream.

In this paper we present spectrally resolved SFG time-to-space (T-S) conversion for serial-to-parallel demultiplexing using a bulk periodically-poled lithium niobate (PPLN) crystal. This technique converts a fast temporal data stream to a quasi-static spatial image which can then be detected by an array of photodetectors. In addition to relief from precise timing synchronization, an advantage of T-S conversion is the preservation of phase information during the conversion process and the generation of a narrowband output signal. This characteristic makes T-S conversion especially attractive when compared to time-to-frequency conversion, which generates a wideband output signal making coherent detection inaccessible. Other serial-to-parallel conversion techniques mentioned above (multiple quantum well based T-S conversion and angle phase-matched time-and-frequency-to-two-dimensional-space conversion) are limited, respectively, in speed by the picosecond scale charge carrier lifetime and in conversion efficiency by the non-collinearly phase-matched interaction and requirement for one gating pulse per demultiplexed signal pulse.

Spectrally resolved T-S conversion using second harmonic generation (SHG) was first demonstrated in a lithium triborate crystal at 920 nm [22]. Collinear non-critically phase-matched degenerate SHG at 860 nm in potassium niobate [23] resulted in improved conversion efficiency, but without the possibility of filtering out the background light. T-S conversion at 1560 nm (i.e. in the optical communications C-band) in PPLN was demonstrated [25]. However a limited time window of 25 ps was obtained due to the large spectral component focused spot size necessary for the long interaction length required to obtain the reported conversion efficiency of 0.6%. Non-degenerate, collinearly phase-matched SFG for background-free T-S conversion in the telecom window using a beta barium borate (BBO) crystal was recently demonstrated, with high resolution but low conversion efficiency due to the relatively small nonlinear coefficient of BBO [26]. Here we provide an updated summary of our research on T-S conversion with PPLN presented at the OSA Topical Meeting on Nonlinear Photonics (Colorado Springs, 17-21 June 2012) [27]. In particular, we employ a custom made wide aperture PPLN chip to achieve increased conversion efficiency whilst preserving high resolution and background-free operation. Additionally, the effect of T-S conversion with non-degenerate SFG on the time-to-space mapping factor is determined and experimentally verified, and an approach to achieve higher conversion efficiency by means of a PPLN planar waveguide is proposed.

2. Non-degenerate time-to-space conversion

Time-to-space conversion is based on SFG between the dispersed frequency components of a signal pulse stream and a single reference pulse in a nonlinear medium [22, 24] (see Fig. 1). The signal and reference beams, at central frequencies ω_s and ω_r respectively, are incident on different diffraction gratings and then pass through a Fourier lens, such that their resolved spectra are superimposed at the focal plane with equal magnitude and opposite direction linear spatial dispersions. By placing a $\chi^{(2)}$ nonlinear crystal at this plane SFG occurs between the overlapping frequency components at each point in space. Due to the matched yet flipped spatial dispersions a quasi-monochromatic SFG wave is generated at each location along the

#175578 - $15.00 USD Received 5 Sep 2012; revised 27 Oct 2012; accepted 28 Oct 2012; published 19 Nov 2012

crystal aperture, with automatic phase-matching across the whole bandwidth of the dispersed pulses. In addition the problem of temporal walkoff associated with short pulse harmonic generation is avoided, since the spectrally resolved pulses are stretched in time.

The generated SFG light carries an instantaneous linear spatial phase which is directly dependant on the time delay between the interacting signal and reference pulses. A second Fourier lens placed after the crystal converts this spatial phase into a transverse spatial shift of the focused pulse image at the output plane. The result is a slowly varying spatial image of the input waveform with one-to-one mapping of the time delay, Δt, of the incoming pulses to a spatial shift, Δx, of the output image. Each spatial pulse image corresponds to a single OTDM bit slot and so may be directly detected by a photodetector or mixed with a narrow linewidth local oscillator for coherent detection.

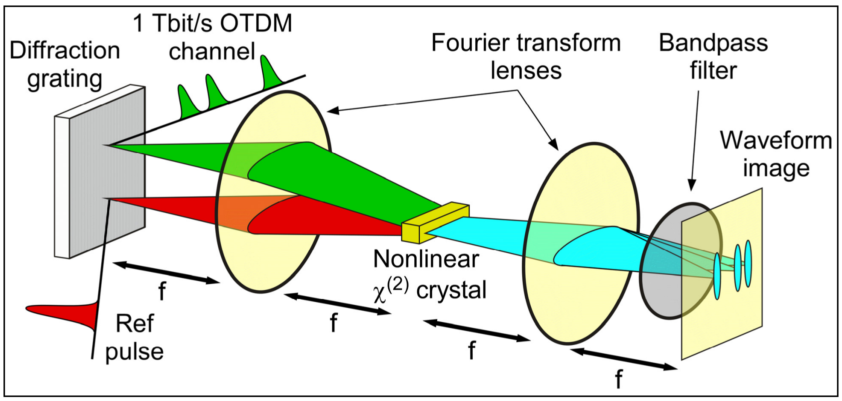

Fig. 1. Time-to-space conversion concept. The time domain information carried by an OTDM channel is transferred to a space domain image via dispersed wave SFG, enabling direct or coherent detection. Note that a non-collinear phase-matching configuration is shown here for clarity, whereas the current experiment utilizes collinear phase-matching for an extended interaction length, necessitating the use of a bandpass filter for separating the SFG light from the background SHG of the signal and reference beams.

The time-to-space mapping factor is given by the product of the linear spatial dispersion and a scaling factor incorporating the new carrier frequency due to the second spatial Fourier transform [25]; taking into account the non-degenerate wavelengths of our signal and reference pulses results in:

$$\frac{\Delta x}{\Delta t} = \frac{f_2}{f_1} \cdot \frac{c \cos \beta}{f_{g,s} \lambda_s} \cdot \frac{\lambda_r}{\lambda_s + \lambda_r} \tag{1}$$

where f_1 and f_2 are the focal lengths of the first and second Fourier lenses respectively, c is the speed of light, β is the angle of diffraction of the central wavelength component of the dispersed signal pulse, $f_{g,s}$ is the signal pulse diffraction grating frequency and λ_s and λ_r are the signal and reference pulse central wavelengths respectively. Equation (1) reduces to the same scaling factor presented in [25] for the degenerate case.

In addition to the information carrying SFG signal at $\omega_s + \omega_r$, the signal and reference pulses each independently produce SHG light centered about $2\omega_s$ and $2\omega_r$. This light carries no useful information, yet propagates to the output spatial image plane and there forms an unwanted background to the pulse image. However, since the interacting pulses are at non-degenerate wavelengths the SHG background light is spectrally offset from the SFG signal (ie. $2\omega_s > \omega_s + \omega_r > 2\omega_r$), and so a background-free output image can be obtained by placing a bandpass spectral filter centered about $\omega_s + \omega_r$. This also allows the use of collinearly propagating signal and reference beams, thus maximizing their interaction length inside the nonlinear medium.

#175578 - $15.00 USD Received 5 Sep 2012; revised 27 Oct 2012; accepted 28 Oct 2012; published 19 Nov 2012

The key performance metrics of the T-S converter are the serial-to-parallel resolution factor, *N*, and the conversion efficiency, η. The resolution factor *N* determines the maximum number of signal pulses that can be simultaneously demultiplexed by a single reference pulse and is dependent on the time window of operation. The limited time window stems from the decrease in output image intensity due to less temporal overlap with increasing time delay between the reference pulse and a signal pulse at the $\chi^{(2)}$ nonlinear crystal.

The conversion efficiency η is defined as the SFG output power divided by the signal beam power incident on the nonlinear crystal. The resolution-efficiency product is invariant to the spot size of a spectral component focused at the crystal, so that one parameter can be improved at the expense of the other [24]. In other words, decreasing the spectral component spot size results in an enhanced resolution, but this is achieved at the expense of conversion efficiency due to the shorter interaction length. However the larger $\chi^{(2)}$ nonlinearity of PPLN compared with BBO allows an increase in conversion efficiency without loss of resolution.

3. Experiment

Our experimental setup is shown in Fig. 2. The signal and idler (reference) outputs of a Spectra-Physics Opal OPO (with signal pulse duration 100 fs and repetition rate 80.2 MHz) are expanded to appropriate collimated beam sizes and undergo equal and opposite linear spatial dispersions of approximately 5 mm over a 40 nm (FWHM) bandwidth by diffraction gratings and 75 mm lenses. The dispersed beams are superimposed by a dichroic mirror and are incident on a PPLN crystal located at the focal plane. The main characteristics of the input beams are given in Table 1. Noncritically phase-matched SFG results in a quasi-monochromatic output beam at 810 nm, which another lens of focal length 75 mm coherently focuses to a tight spot at the pulse image plane. A CMOS camera records the output spatial image, with background second harmonic light from the signal and reference beams being blocked by a bandpass filter between the lens and the camera.

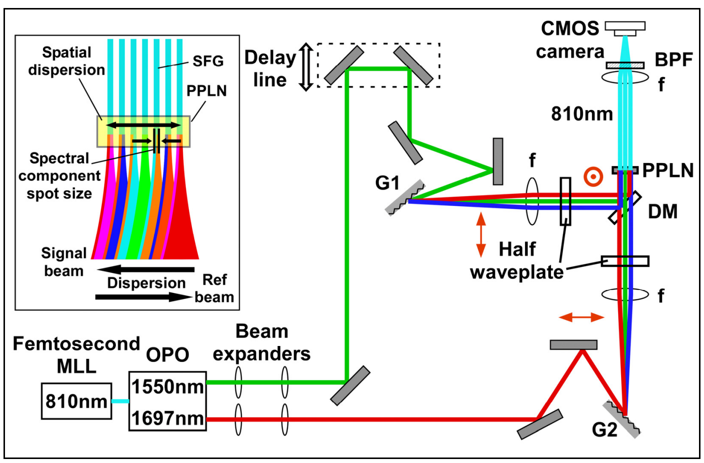

Fig. 2. Experimental setup (MLL, mode-locked laser; OPO, optical parametric oscillator; G1/G2, grating; f, Fourier lens; DM, dichroic mirror; PPLN, periodically-poled lithium niobate; BPF, bandpass filter. Inset: dispersed signal and reference beams at the PPLN chip.

Table 1. Input Beam Characteristics of Time-to-Space Converter[a]

	λ_0 (nm)	f_g (lp/mm)	α (°)	β (°)	dx/dv (mm/THz)	w_0 (μm)	P_{av}/P_{max} (mW/kW)
Signal	1550	1100	70	50	1.03	13	240/30
Reference	1697	1000	80	45	−1.03	14	64/8

[a]λ_0, central wavelength; f_g, grating frequency; α, incidence angle on grating; β, diffraction angle of central wavelength component; dx/dv, spatial dispersion; w_0, focused spot radius of single spectral component in the horizontal direction; Pav/Pmax; average beam power/peak power at the PPLN. Ideally the reference beam power would be higher than the signal power.

#175578 - $15.00 USD Received 5 Sep 2012; revised 27 Oct 2012; accepted 28 Oct 2012; published 19 Nov 2012

PPLN was chosen as the nonlinear medium due to its high d_{eff} coefficient of 16 pm/V (taking into account the reduction by a factor 2/π due to periodic poling) and the absence of spatial walkoff between the extraordinary polarized interacting beams. The PPLN chip used in this experiment was fabricated and anti-reflection coated, with a domain length of 20.3 μm (for a phase-matching temperature of 165 °C) and dimensions of 6 mm in the light propagation direction and 10 mm in the spatial dispersion direction. The extra wide crystal aperture is necessary in order to accommodate the full spatial extent of the dispersed beams and avoid limiting the interaction bandwidth. The confocal length of the focused spectral components of the signal and reference beams in the plane of dispersion was 1.5 mm, thus only a short section of the crystal length is utilized in practice.

4. Results

An example pulse image with a sech squared fit to its horizontal cross-section is shown in Fig. 3(a); we placed a neutral density filter in front of the camera in order to suppress saturation. By varying the delay line in the signal beam path the temporal offset between the signal and reference pulses arriving at the PPLN is controlled. This temporal offset is translated by the T-S conversion process into a transverse spatial shift of the pulse image. Inserting the experimental setup parameters (see Table 1) into Eq. (1) gives a T-S conversion factor of 59.1 μm/ps, in excellent agreement with the measured conversion factor of 58.8 μm/ps. In order to demonstrate the potential for demultiplexing a 1 Tbit/s OTDM channel we recorded 42 individual pulse images at 1 ps separation throughout the FWHM time window (Figs. 3(b) and 3(c)).

The time window was determined by measuring the variation in output pulse image intensity with time delay and the conversion efficiency was measured using a power meter placed after the bandpass filter (at zero time delay); the results are summarized in Table 2.

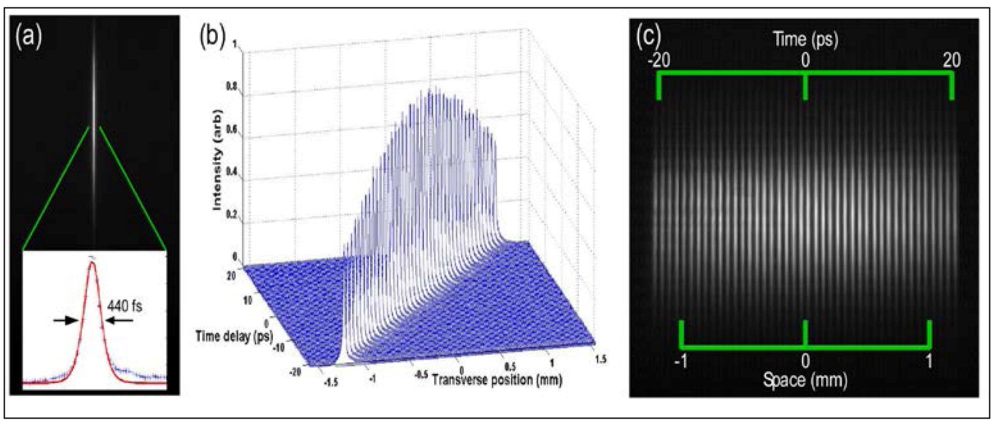

Fig. 3. (a) T-S converted signal pulse image with 440 fs FWHM, (b) pulse image intensity profiles showing shift in spatial position and intensity fall-off with varying time delay and (c) 42 pulse images distributed throughout the T-S processor time window (composite image).

Table 2. PPLN-based T-S Conversion Performance Parameters[a]

ΔT (ps)	τ (fs)	N (= ΔT/ τ)	η (%)	Conversion efficiency slope (%/W)	Bandwidth (nm)
42	440	95	0.03	0.6	0.09

[a]ΔT, FWHM time window; τ, FWHM pulse image width; N, serial-to-parallel resolution factor; η, conversion efficiency.

Note that the pulse image width at 440 fs is approximately three times longer than the expected width for the 100 fs signal pulse (including the autocorrelation factor of ~1.5). This is mainly due to the fact that our reference pulse duration is 210 fs. Of course the reference pulse should ideally be short and intense compared to the signal pulse, enabling high T-S

#175578 - $15.00 USD Received 5 Sep 2012; revised 27 Oct 2012; accepted 28 Oct 2012; published 19 Nov 2012

fidelity and conversion efficiency. A factor 30 increase in conversion efficiency and factor 60 increase in conversion efficiency slope compared with our previous work using BBO [26] were achieved (see Fig. 4(a)). This compares well with the predicted increase in conversion efficiency slope due to the larger nonlinear coefficient of PPLN:

$$\frac{\eta_{SFG-PPLN}}{\eta_{SFG-BBO}} = \left(\frac{(2/\pi) \cdot d_{eff,LiNbO3}}{d_{eff,BBO}} \right)^2 = 64 \tag{2}$$

where η is conversion efficiency and d_{eff} is the effective nonlinear coefficient of the crystal.

Finally, the SFG bandwidth was measured as 0.09 nm using light coupled by a single mode fiber into an optical spectrum analyzer (Fig. 4(b)). This two order-of-magnitude reduction from the input signal bandwidth (5 THz to 40 GHz) brings the ultrafast input waveform to within the detection bandwidth of a fast optoelectronic receiver. In addition, the relatively narrow linewidth of the converted signal shows the potential for extraction of phase information using coherent detection.

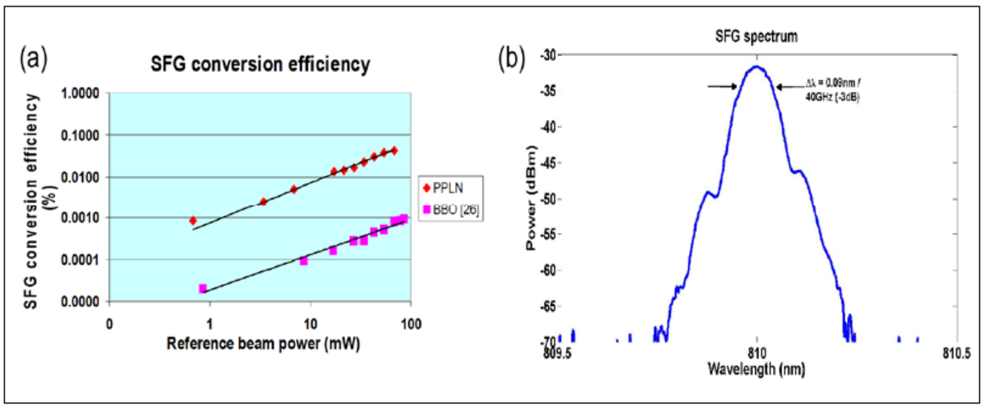

Fig. 4. (a) T-S conversion efficiency slope with PPLN (red diamonds) and BBO (pink squares) and (b) SFG narrowband spectrum centered at 810 nm with a –3 dB bandwidth of 0.09 nm (= 40 GHz).

5. Discussion and conclusion

The obtained T-S conversion efficiency of 0.03% in our current setup is clearly too low to be considered as a viable solution for OTDM demultiplexing. In order to boost the conversion efficiency we propose to implement the SFG interaction in a PPLN planar waveguide, with the interacting waves confined in the vertical direction. The non-degenerate configuration utilized here and in [26] is ideally suited for this task, as it is impossible to use a non-collinear arrangement with vertical confinement in a planar waveguide. The advantages of performing the T-S conversion in a planar waveguide are twofold; the vertical mode height can be focused independently and more tightly thereby increasing the interaction intensity and the tight vertical mode does not impose any diffraction limitation as the mode is confined within the waveguide structure.

The estimated vertical mode size in a planar waveguide defined by titanium diffusion at the reference wavelength (1697 nm) is approximately 5.5µm ($1/e^2$ intensity points diameter). Compared to our current bulk PPLN crystal setup, where the vertical mode size of the reference beam is approximately 100 µm, this represents an intensity increase factor of 18, which should translate directly to a conversion efficiency improvement from the signal light to the generated SFG light. In addition, whereas the interaction length will still be limited by diffractive spreading in the non-confined horizontal direction, preservation of the beams' intensity in the vertical direction along the interaction length should result in a further

#175578 - $15.00 USD Received 5 Sep 2012; revised 27 Oct 2012; accepted 28 Oct 2012; published 19 Nov 2012

increase in conversion efficiency by a factor of √2. Thus a total increase by factor 25 in conversion efficiency as compared to the bulk PPLN T-S conversion reported here is expected due to these combined effects, bringing the overall conversion efficiency close to 1%.

In conclusion we have demonstrated high resolution and increased efficiency background-free time-to-space conversion using non-critically phase-matched SFG in a PPLN crystal. The quasi-monochromatic SFG output signal implies the potential for recovery of phase encoded information by coherent detection, allowing compatibility with advanced modulation formats such as n-QAM which are necessary for high spectral efficiency. We are currently planning a phase extraction experiment using a narrow linewidth local oscillator in order to demonstrate this possibility. The PPLN slab waveguide currently under fabrication will allow tight confinement of the light intensity in the vertical direction and thus further increase the conversion efficiency, en route towards practical time-to-space detection of optical waveforms in the lightwave telecommunication band.

Finally, the conversion of amplitude and, potentially, phase information from the time domain to the spatial domain by means of spectrally resolved SFG is a very general technique which can find applications in a number of fields in addition to optical communications. For example the ability to perform single-shot imaging of non-repetitive ultrafast temporal waveforms with high resolution would be useful for investigating femtosecond time scale molecular dynamics. T-S conversion may also be interesting for single wavelength channel real-time photonic analog-to-digital conversion due to the possibility for oversampling of the converted signal in the spatial domain, thus reducing detection errors.

#175578 - $15.00 USD Received 5 Sep 2012; revised 27 Oct 2012; accepted 28 Oct 2012; published 19 Nov 2012

Chapter 3: Increased efficiency time-to-space conversion in a nonlinear planar waveguide

3.1 Time-to-space conversion in a nonlinear planar waveguide

By employing PPLN as the nonlinear medium for time-to-space conversion, a factor 60 increase in conversion efficiency slope was obtained compared with the use of BBO. This increase was due to the stronger $\chi^{(2)}$ nonlinearity of PPLN and the fact that QPM allowed the use of parallel polarised fundamental and SFG waves, thus enabling access to the highest d_{eff} coefficient of the lithium niobate nonlinear susceptibility tensor. However the scope for further increases in conversion efficiency slope by using different nonlinear crystals is limited; instead a change in the optical arrangement is required.

As mentioned in Chapter 1.2, there is an inherent trade-off between the two main time-to-space conversion performance parameters: the time window and the conversion efficiency. In order to widen the time window, the spectral resolution of the dispersed signal and reference pulses at the Fourier plane of the spectral processor must be increased. This can be accomplished by expanding the collimated beam size of the signal and reference beams arriving at the diffraction gratings. Note that the use of shorter focal length Fourier lenses will not increase the spectral resolution, since as well as decreasing the focused spot size at the Fourier plane the linear spatial dispersion extent will also decrease. The spectral processor resolution is independent of the Fourier lens focal length. However, illuminating a larger area of the diffraction grating results in tighter focusing of the spectral components at the Fourier plane whilst leaving the spatial dispersion extent unaltered, resulting in higher spectral resolution.

The Rayleigh length z_R is the distance along the optical axis over which a focused beam stays relatively focused; at a distance of one Rayleigh length from the focal plane the beam radius has increased by a factor of $\sqrt{2}$:

$$z_R = \frac{\pi w_0^2}{\lambda} \tag{3.1}$$

where w_0 is the focused spot radius and λ is the wavelength in vacuum. The efficiency of the SFG process depends on the optical intensity present at each point along the crystal length. Since it is inversely proportional to the square of the beam radius, the intensity of a diverging beam falls off quickly for increasing distance from the focal plane. At the Rayleigh length the intensity has decreased by a factor of two and further along the optical axis the intensity decreases as the square of the propagation distance. Therefore tighter focusing of the dispersed signal and reference beams, whilst giving a larger time window, results in decreased conversion efficiency (see Fig. 3.1).

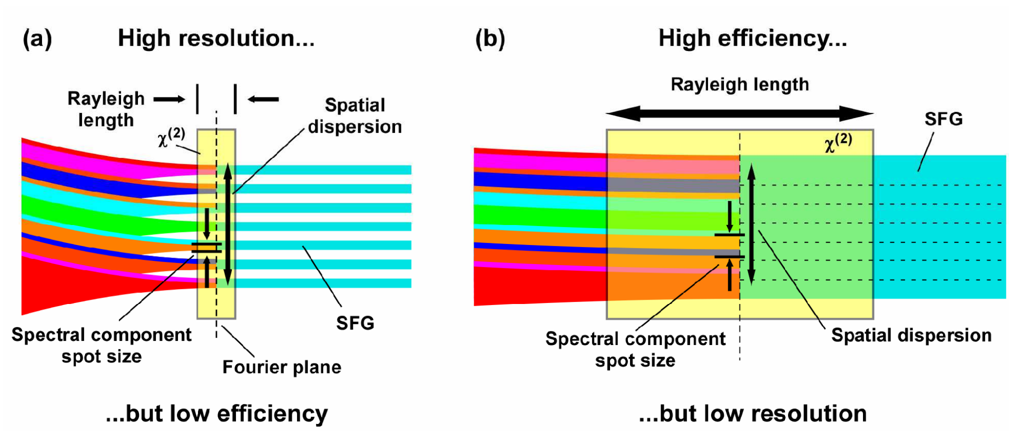

Fig. 3.1: Time window vs conversion efficiency. (a) High spectral resolution of the signal and reference frequency components at the Fourier plane results in a wider time window for the output time-to-space converted pulse image. However the reduced Rayleigh length due to tighter focusing (and hence faster beam divergence) of the frequency components means a shorter interaction length inside the nonlinear crystal, thus limiting the conversion efficiency. (b) Loose focusing of the signal and reference pulse spectral components increases their Rayleigh length, giving a longer interaction length inside the nonlinear crystal and resulting in higher conversion efficiency. However the low spectral resolution limits the time window.

This time window – conversion efficiency invariance [16] is an intrinsic feature of time-to-space conversion by spectrally resolved SFG as has been presented so far. It stems from free-space diffraction of the focused signal and reference frequency components within the spectral processor. In order to attain high conversion efficiency whilst preserving a large time window, it is necessary to break this invariance. This can be achieved by stopping the diffraction of the focused spectral components via implementation of guided-wave time-to-space conversion. By confining the SFG interaction between the spatially dispersed signal and reference waves in nonlinear waveguides, diffraction is eliminated and the interaction length can be made much longer, subject to waveguide fabrication limitations and temporal walkoff effects. At the same time the high spectral resolution necessary for a large time window is maintained, since each waveguide contains a single pair of phase-matched signal and reference frequency components (also subject to waveguide design restraints).

It can now be appreciated why the demonstration of background-free time-to-space conversion with collinearly propagating signal and reference beams, described in Chapter 2, is significant with respect to guided wave time-to-space conversion. The signal and reference spectral components confined in single mode waveguides are necessarily co-propagating. Background SHG removal by spatial filtering would not be possible since there is no angular or spatial separation between the SHG light and the SFG (signal-carrying) light at the waveguide exits. Therefore spectral filtering of the SHG background enabled by wavelength non-degenerate signal and reference beams co-propagating in the time-to-space converter was a necessary step towards implementation of guided wave time-to-space conversion.

Realisation of guided wave time-to-space conversion in an array of nonlinear waveguides is a complex technical challenge. Therefore, the intermediate stage of time-to-space conversion in a one-dimensional planar waveguide in PPLN was demonstrated. In this case the interacting spectral components are confined in the vertical direction inside the planar waveguide, with free-space diffraction in the horizontal plane (see Fig. 3.2). By eliminating diffraction in the vertical direction the overall intensity over the length of the PPLN chip is higher than when compared with the completely unguided case in bulk PPLN. However the Rayleigh length of the free-

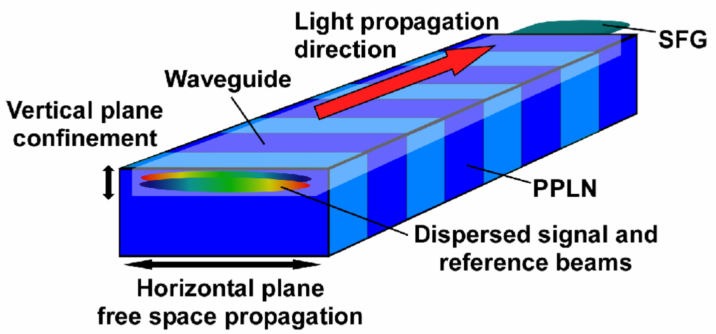

Fig. 3.2: Planar waveguide in PPLN. The signal and reference dispersed waves are confined in the vertical direction by a slab waveguide at the top surface of the PPLN chip. There is no confinement in the horizontal plane and so diffraction of the focused spectral components occurs. The effective interaction length determining the conversion efficiency is therefore the Rayleigh length of the focused spectral components in the horizontal plane. The diagram is not to scale.

space diffracting frequency components in the horizontal plane still determines the effective interaction length, thus limiting conversion efficiency.

The planar waveguide in PPLN was also fabricated at the University of Paderborn with physical dimensions of 10 mm × 4 mm × 0.5 mm in the spatial dispersion, light propagation and vertical directions respectively and poling periodicity of 18.7 μm. This was smaller than that of the bulk PPLN because of the increased effective refractive index due to the waveguide. Details of the fabrication process are given in Chapter 3A. The optical arrangement used to focus the dispersed signal and reference beams into the planar waveguide is also detailed in Chapter 3A. However, in order to achieve efficient coupling into the planar waveguide preliminary measurements were performed and these are now described.

First the guided spatial mode sizes of the signal and reference light emerging from the exit face of the waveguide were measured. Since the purpose of this measurement was simply to determine the guided mode size of the signal and reference light inside the planar waveguide, it was not performed within the spectral processor setup (i.e. the light coupled into the planar waveguide was not first dispersed by diffraction gratings). Furthermore, a CW source was used for the signal light at 1550 nm instead of the sub-ps pulses from the OPO. For the reference light measurement no CW source was available at 1697 nm and so the OPO source was used. In each case the signal and reference light was coupled via a lensed fibre brought almost in contact with the input face of the planar waveguide (see Fig. 3.3). A 0.65 numerical aperture (NA) microscope objective and a 1000 mm focal length lens were used to magnify by a factor 180 the light exiting the planar waveguide and image it onto an InGaAs

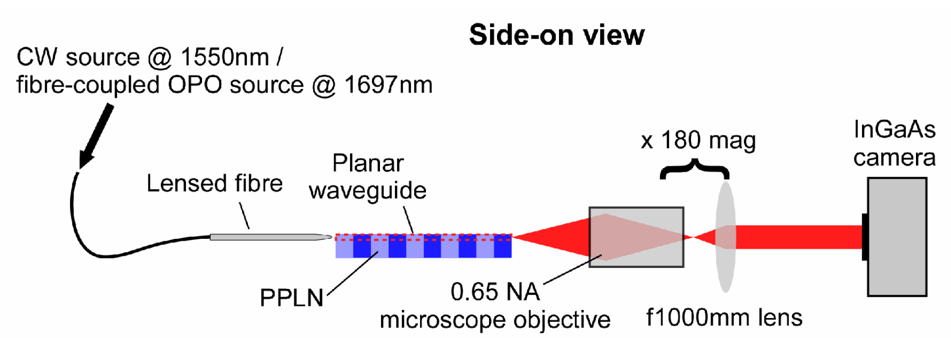

Fig. 3.3: High NA imaging of the guided mode size in the PPLN planar waveguide. Light at 1550 nm or 1697 nm is alternately coupled into the PPLN planar waveguide via a lensed fibre. The guided mode emerging from the end face of the crystal is magnified and imaged onto the InGaAs camera. The region of the planar waveguide in the PPLN is shown by the red dashed line (diagram is not to scale).

camera. A visible light source reflected off the PPLN crystal exit face was used to focus the exit face magnified image onto the camera, before taking measurements of the IR light. From Gaussian fits to the recorded intensity profiles the vertical mode sizes were measured as 3 ± 0.2 μm and 3.5 ± 0.2 μm (FWHM) for the signal light at 1550 nm and the reference light at 1697 nm respectively. These measurements compare well with the theoretical values of 3 μm and 3.25 μm for 1550 nm and 1697 nm light respectively. An example image of the guided mode at 1550 nm is shown in Figure 3.4.

Since only the optical power which is coupled into the PPLN planar waveguide contributes to the SFG interaction, it was necessary to measure the insertion loss (IL). This is defined as the ratio of the optical power of the guided mode emerging from the waveguide exit face to the optical power of the input beam at the entrance face of the waveguide (assuming that absorption is negligible over the 4 mm propagation distance in the waveguide). In order to determine the IL of the signal and reference beams, a power meter was first used to measure the beam power at the PPLN entrance face. Note that the IL measurements were all performed using the OPO sub-ps source for the signal and reference light, but with non-dispersed light. The high NA imaging system described above was then used to optimise coupling of the signal / reference light into the planar waveguide, by viewing the light emerging from the waveguide exit on the camera. An adjustable slit was then placed in front of the camera, vertically centred on the light exiting the planar waveguide and closed until the emerging beam just began to become clipped. In other words the slit aperture was

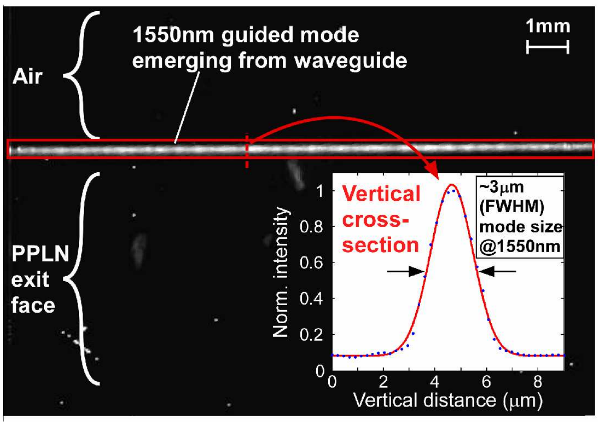

Fig. 3.4: Example guided mode image. InGaAs camera snapshot showing the upper part of the exit face of the PPLN crystal with emerging light from the 1550 nm vertically guided mode. The region of the planar waveguide is marked with a red line. The inset shows a vertical cross-section of the recorded intensity profile, with a 3 μm FWHM.

adjusted to block any non waveguide-coupled light from the signal / reference beam from reaching the camera. The camera was then replaced with the power meter and the optical power measured (see Fig. 3.5). The insertion loss was given by the difference (in dB) between this measurement and the previous measurement of optical power at the PPLN entrance face. Losses in the microscope objective and telescope lens were assumed to be negligible.

The signal and reference beam insertion losses were measured as 4.1 dB and 4.9 dB respectively. Possible causes for these quite high insertion losses include imperfect spatial mode matching of the focused signal and reference beams at the waveguide entrance to the guided modes supported in the waveguide and non lowest order spatial mode and / or spatial frequency noise on the signal and reference beams exiting the OPO. The higher IL for the reference beam is consistent with the observed spatial mode of this beam, which is not a lowest order Gaussian mode on exiting the OPO. Note that this measurement using the adjustable slit was less than ideal since the measured IL depended sensitively on the slit aperture. Ideally all of the background non-coupled light should be blocked whilst allowing through all of the coupled light emerging from the waveguide. However it is unlikely that this ideal situation was realised in the measurement.

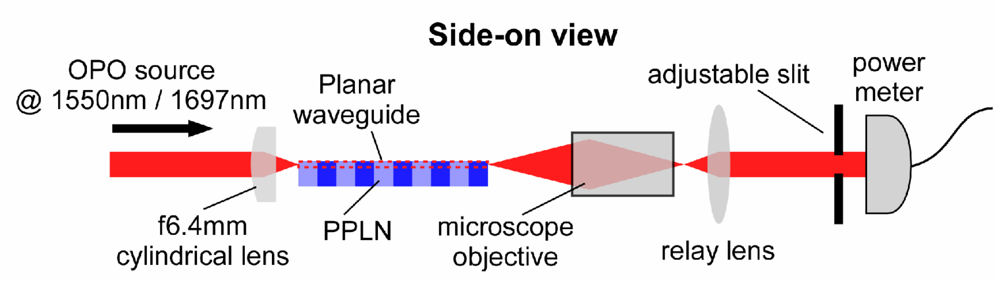

Fig. 3.5: Measurement of insertion loss into the PPLN planar waveguide. The signal and reference beam powers after the cylindrical lens were alternately measured by the power meter (not shown in this diagram). The beams were then focused into the waveguide; coupling was maximised by using the InGaAs camera to view the guided mode emerging from the waveguide exit face (also not shown in the diagram). An adjustable slit was then used to block background non-coupled light, whilst allowing light exiting the waveguide to be incident on the power meter for the insertion loss measurement (diagram is not to scale).

Chapter 3A

Time-to-space conversion of ultrafast waveforms at 1.55 μm in a planar periodically poled lithium niobate waveguide

Dror Shayovitz, Harald Herrman, Wolfgang Sohler, Raimund Ricken, Christine Silberhorn and Dan M. Marom

Published in Optics Letters:

D. Shayovitz, H. Herrman, W. Sohler, R. Ricken, C. Silberhorn and D. M. Marom, "Time-to-space conversion of ultrafast waveforms at 1.55 μm in a planar periodically poled lithium niobate waveguide," Opt. Lett. **38**, 4708-4711 (2013).

Time-to-space conversion of ultrafast waveforms at 1.55 μm in a planar periodically poled lithium niobate waveguide

Dror Shayovitz,[1,*] Harald Herrmann,[2] Wolfgang Sohler,[2] Raimund Ricken,[2] Christine Silberhorn,[2] and Dan M. Marom[1]

[1]Department of Applied Physics, Hebrew University of Jerusalem, Jerusalem 91904, Israel

[2]Applied Physics, University of Paderborn, Warburger Str. 100, D-33098 Paderborn, Germany

*Corresponding author: dror.shayovitz@mail.huji.ac.il

Received August 16, 2013; revised October 9, 2013; accepted October 9, 2013; posted October 10, 2013 (Doc. ID 195946); published November 12, 2013

We report the first demonstration, to our knowledge, of time-to-space conversion of subpicosecond pulses in a slab nonlinear waveguide. By vertically confining the nondegenerate sum-frequency generation interaction between a spatially dispersed 100 fs signal pulse at 1.55 μm and a reference pulse in a titanium indiffused planar periodically poled lithium niobate crystal waveguide, we have attained a conversion efficiency of 0.1% and a conversion efficiency slope of 4% per watt of reference beam power. This was achieved while maintaining high conversion resolution, with a measured time window of operation of 48 ps resulting in a serial-to-parallel demultiplexing factor of 90.

OCIS codes: (190.0190) Nonlinear optics; (320.0320) Ultrafast optics; (060.0060) Fiber optics and optical communications.

http://dx.doi.org/10.1364/OL.38.004708

The continued rapid growth in Internet and data center traffic stimulates research into optical communications transmission techniques, in order to increase data capacity and spectral efficiency and reduce energy consumption. Optical time division multiplexing (OTDM) enables generation of record multi-Tbaud symbol rates on a single wavelength channel, and can be combined with advanced modulation formats to achieve greater than 10 Tb/s data transmission [1]. Techniques for demultiplexing a Tb/s OTDM channel must exploit optical nonlinearities due to the limited bandwidth (up to around 100 GHz) of optoelectronic devices. Various types of all-optical switching to extract a single bit from an OTDM channel have been investigated, including the nonlinear optical loop mirror [2,3], sum-frequency generation (SFG) in periodically poled lithium niobate (PPLN) waveguides [4], and four-wave mixing (FWM) in silicon and chalcogenide nonlinear waveguides [5,6]. However, the number of switching devices required scales with the OTDM symbol rate, increasing the total power consumption and system complexity.

Serial-to-parallel demultiplexing methods overcome this problem by using a single device to simultaneously demultiplex an entire OTDM channel, on a frame-by-frame basis. Examples include multiple quantum well based time-to-space (T-S) conversion [7], time-to-frequency conversion by FWM [8,9], and spectrally resolved SFG T-S conversion [10–16]. T-S conversion transforms the OTDM serial pulse stream into a quasi-static parallel spatial image, using SFG between multiple signal pulses and a single reference pulse. Each output spatial pulse image corresponds to a single OTDM bit slot and so may be directly detected by a photodetector or mixed with a narrow linewidth local oscillator for coherent detection.

T-S conversion by degenerate SFG was first demonstrated at 920 nm with an LBO nonlinear crystal [10] and later at 1550 nm with bulk PPLN [13]. We have previously performed background-free T-S conversion using nondegenerate and collinearly phase-matched SFG in a BBO crystal [14] and in bulk PPLN [15]. However, free-space diffraction of the signal and reference beams in the bulk nonlinear crystal limits the SFG interaction length, and therefore also limits the T-S conversion efficiency. To achieve reasonable conversion efficiencies, a high-peak-power (some hundreds of kilowatts) reference pulse is needed, making the T-S conversion technique impractical for real system use. In order to overcome this barrier, it is necessary to both increase the intensity of the interacting beams by tight focusing and simultaneously increase the interaction length. In the free-space regime, tighter focusing results in more rapid beam spreading due to diffraction and therefore reduced interaction length. However, confinement of the SFG interaction in a nonlinear planar waveguide prevents beam spreading in one dimension and thus a greater effective interaction length can be achieved.

In this Letter, we report the first demonstration, to our knowledge, of T-S conversion in a planar nonlinear waveguide [16]. By confining the interacting signal and reference light within a PPLN slab waveguide, we have significantly improved the T-S conversion efficiency compared to our previous work in bulk PPLN [15], while maintaining a high serial-to-parallel demultiplexing factor.

The operation of a T-S processor is described in detail in [10–12] and briefly summarized here. The signal pulse stream and a single reference pulse are incident on diffraction gratings and pass through Fourier lenses, such that their resolved frequency components are superimposed at the spectral plane with equal magnitudes but opposite directions of the spatial dispersions. By placing a $\chi^{(2)}$ nonlinear crystal at the spectral plane, SFG between the superimposed frequency components occurs at each point in space. Due to the matched yet flipped spatial dispersions, a quasi-monochromatic SFG wave is generated across the crystal aperture. The SFG light carries an instantaneous linear spatial phase, which is

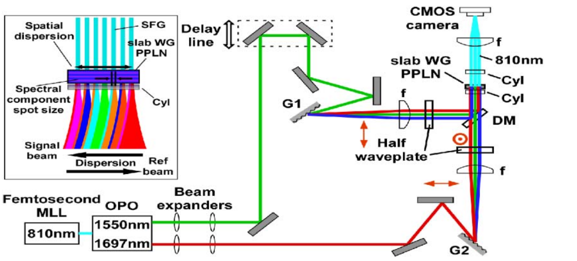

Fig. 1. Experimental setup (MLL, mode-locked laser; OPO, optical parametric oscillator; G1/G2, grating; f, Fourier lens; Cyl, vertical cylindrical lens; DM, dichroic mirror; slab WG PPLN, slab waveguide in PPLN). Inset: dispersed signal and reference beams at the slab WG PPLN.

directly dependant on the time delay between the incoming signal and reference pulses. A second Fourier lens placed after the crystal converts this instantaneous linear phase into a transverse spatial shift of the focused pulse image at the output plane. The result is a slowly varying spatial image of the input signal waveform with one-to-one mapping of the temporal position of the incoming pulses to the spatial position of the output image.

Figure 1 shows the slab waveguide PPLN T-S experimental setup. The signal and idler (reference) pulses of a spectra-physics opal optical parametric oscillator (OPO) have central wavelengths of 1550 and 1697 nm, respectively, FWHM pulse durations of 100 and 210 fs, respectively, and an 80 MHz repetition rate. The two beams are anamorphically expanded to appropriate collimated beam sizes in the vertical and horizontal directions and undergo equal and opposite linear spatial dispersions of approximately 5 mm over a 40 nm (−3 dB) bandwidth by diffraction gratings and 75 mm Fourier lenses. The dispersed beams are then superimposed by a dichroic mirror and focused in the vertical direction with a 6.4 mm cylindrical lens. This focal length was chosen to try to obtain best mode matching between the free-space vertically focused mode sizes at the input facet of the PPLN slab waveguide to the guided mode size within the waveguide.

The PPLN chip (with length 4 mm; see Fig. 2) was positioned along the optical axis such that the dispersed signal and reference beams' horizontal spectral planes were located at its center, in order to best exploit the waveguide length for generation of SFG light. The cylindrical focusing lens was then placed such that the signal and reference beams' vertical focal planes were displaced

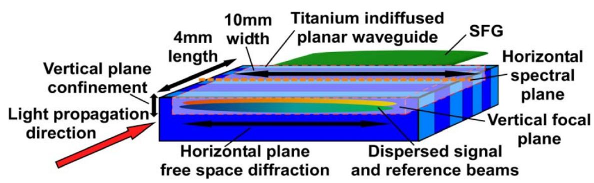

Fig. 2. Slab waveguide PPLN (not to scale) showing titanium indiffusion defined waveguiding region, spatially dispersed signal and reference beams vertically focused to the waveguide entrance facet and horizontally focused to the center of the crystal, and SFG light at the output facet.

by 2 mm ahead of the spectral plane, to the PPLN chip input facet for optimal waveguide coupling.

The PPLN poling period of 18.7 μm was chosen to support quasi phase-matched SFG between the signal and reference pulses' central wavelengths at a crystal temperature of 30°C, taking into account the increased effective refractive index in the slab waveguide region compared to that of bulk PPLN. The waveguide length of 4 mm in the light propagation direction and aperture of 10 mm in the spatial dispersion direction were chosen, respectively, to fully contain the focused spectral components' confocal length and the spatial extent of the dispersed light at the spectral plane.

The slab waveguide was fabricated by indiffusion of an 88 nm thick Ti layer at 1060°C for 8.5 h into the upper surface of the z-cut crystal. The intensity distribution of the waveguide mode at $\lambda \approx 1550$ nm is confined to approximately 3 μm FWHM in the vertical direction. This tight vertical confinement of the signal and reference beams results in increased intensity of the interacting light throughout the propagation length, enabling more efficient generation of SFG light. A broadband antireflection coating from 1500 to 1750 nm was deposited on the PPLN entrance facet and an antireflection coating at 810 nm on the exit facet. The PPLN was held at a temperature of 30°C (± 0.1°C) for optimum phase matching.

The FWHM spot size of the focused spectral components within the crystal was approximately 14 μm. While the signal and reference beams coupled into the waveguide were confined in the vertical direction as single-mode guided waves, free-space diffraction of the focused spectral components in the nonguiding horizontal plane still limits the SFG interaction length. The confocal length in the horizontal direction was 1.2 mm; thus the full length of the chip is not exploited in practice; i.e., horizontal plane diffraction limits the maximum conversion efficiency achievable in our current experiment.

Note that the use of nondegenerate wavelengths for the interacting light is essential in order to avoid generation of strong background second-harmonic generation (SHG) light by the signal and reference pulses individually in the slab waveguide PPLN. This background light would propagate to the output plane and there degrade the pulse image quality, reducing the signal-to-noise ratio at the photodetector placed to receive the demultiplexed bit. The PPLN poling periodicity required for quasi phase-matched SFG between signal and reference beams with widely spaced wavelengths (i.e., 1550 and 1697 nm) does not allow for phase-matched SHG from the input wavelengths individually, and so the SHG background is negligible in this case.

Due to the matched yet flipped spatial dispersions of the two beams, noncritically phase-matched SFG between overlapping pairs of signal and reference spectral components at each point along the PPLN aperture results in a quasi-monochromatic output beam at 810 nm. A 75 mm lens coherently focuses the SFG light to the pulse image plane, with a 25 mm cylindrical lens used for vertical collimation of the light exiting the planar waveguide.

An example of a pulse image recorded by a CMOS camera at the image plane is shown, together with a Gaussian fit to its horizontal cross-section, in Fig. 3(a). The T-S

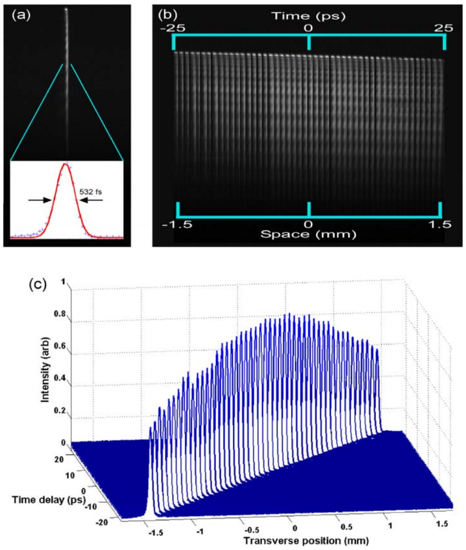

Fig. 3. (a) T-S converted signal pulse image with 532 fs FWHM, (b) 48 pulse images distributed throughout the T-S processor time window of 48 ps (composite image), and (c) pulse image intensity profiles showing shift in spatial position and intensity fall-off with increasing time delay.

conversion factor was measured as 62 μm/ps, by recording the shift in the transverse spatial position of the output pulse image at different signal pulse delay line lengths. This compares well with the calculated value of 59 μm/ps (see Ref. [15], where the Fourier lens focal lengths and diffraction grating frequency used are essentially the same as in the current experimental setup). The resulting FWHM pulse image width τ was found to be 532 fs, which is longer than the ideally expected image width of 232 fs corresponding to the cross correlation of a 100 fs signal pulse with a 210 fs reference pulse. We attribute this broadening to the poor beam quality of the reference beam ($M^2 = 1.3$). This results in less than optimal focusing of the reference pulse spectral components at the Fourier plane, reducing the T-S processor spectral resolution and so limiting the image plane resolution.

An important performance parameter of the T-S processor is the time window of operation ΔT. This is equivalent to the duration of the SFG output pulse and defines the maximum spatial extent of the T-S converted output parallel pulse images. The time window is determined by the temporal overlap of the interacting signal and reference pulses within the processor, which results in a drop in generated SFG signal power from the center of the time window toward its edges. The FWHM time window was measured as 48 ps by changing the delay line length and measuring the variation in SFG power.

The serial-to-parallel conversion factor N is defined as the time window ΔT divided by the pulse image width τ. This determines the maximum number of signal pulses that can be simultaneously demultiplexed by a single reference pulse to spatially separated parallel output channels. Our T-S conversion setup resulted in a conversion factor of $N = 90$. In order to demonstrate the potential for complete demultiplexing of a 1 Tbit/s OTDM channel, we recorded 48 individual pulse images at 1 ps separation throughout the FWHM time window [Figs. 3(b) and 3(c)]; it can be seen that there is clear spatial separation between adjacent output channels and the pulse images obtained are background free.

The T-S conversion efficiency η is defined as the SFG output power divided by the signal beam power coupled into the slab waveguide PPLN. We obtained a maximum conversion efficiency of 0.1% at 23 mW of coupled reference beam average power and a conversion efficiency slope of 4% per watt of coupled reference beam power [see Fig. 4]. Reference [13] reports a higher conversion efficiency of 0.6%; however, this was achieved at the expense of a reduced time window of 25 ps due to the decrease in spectral resolution required for fully exploiting the crystal interaction length (trading off efficiency for resolution).

The insertion losses for the signal and reference beams into the slab waveguide were measured as 4.1 and 4.9 dB, respectively. The average power and peak power of the signal (reference) beam at the PPLN waveguide entrance facet were 132 (70) mW and 16.5 (4.2) kW, respectively. Ideally, the pump power should be much higher than the signal power.

The SFG output signal bandwidth was measured as 0.1 nm (46 GHz) using light coupled via a multimode fiber into an optical spectrum analyzer [see Fig. 5]. This two-order-of-magnitude reduction from the input signal pulse bandwidth (from 5 THz to 46 GHz) implies the possibility for extraction of phase information from the converted signal by using coherent detection techniques.

The slab waveguide PPLN T-S conversion results are summarized and compared to those obtained with bulk PPLN [15] in Table 1. Note that the time window and serial-to-parallel resolution factors are similar for slab waveguide PPLN and for bulk PPLN T-S conversion. This is as expected since these parameters are determined

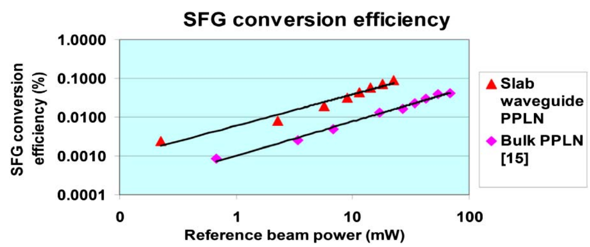

Fig. 4. T-S conversion efficiency slope for slab waveguide PPLN (red triangles) compared to our previous result with bulk PPLN crystal (pink diamonds; see Ref. [15]).

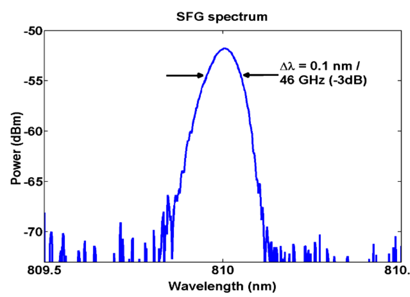

Fig. 5. Output SFG spectrum centered at 810 nm with a –3 dB bandwidth of 0.1 nm (= 46 GHz); the optical spectrum analyzer resolution was set to 0.01 nm for this measurement.

Table 1. Slab Waveguide PPLN and Bulk PPLN T-S Conversion Performance Parameters[a]

	ΔT (ps)	τ (fs)	N	η (%)	Conversion Efficiency Slope (%/W)	Bandwidth (nm)
Slab WG PPLN	48	532	90	0.1	4	0.1
Bulk PPLN [15]	42	440	95	0.03	0.6	0.09

[a] ΔT, FWHM time window; τ, FWHM pulse image width; N, serial-to-parallel resolution factor ($= \Delta T/\tau$); η, conversion efficiency. Note that due to insertion loss, the maximum conversion efficiency for the slab waveguide PPLN was obtained at lower reference beam average power (23 mW) compared to the bulk PPLN in Ref. [15] (64 mW).

solely by the spectral resolution of the dispersed signal and reference pulses at the spectral plane and ideally should not be affected by the type of nonlinear medium used. The principle difference between T-S conversion in the slab waveguide and bulk PPLN media is the conversion efficiency obtainable.

In summary, we have demonstrated T-S conversion of 100 fs pulses at 1.55 μm in a one-dimensional PPLN waveguide. This advance from a free-space nonlinear interaction to a semiguided wave regime resulted in increased SFG conversion efficiency, while maintaining high serial-to-parallel conversion resolution.

It should be noted that T-S conversion is a true serial-to-parallel demultiplexing technique, with all the signal pulses in the OTDM channel being simultaneously demultiplexed by a single reference pulse. In order to compare the optical power requirements of T-S conversion with other (single bit extraction) demultiplexing techniques, it is useful to consider the reference pulse energy-per-extracted-bit parameter. In our slab waveguide PPLN setup we use 3 pJ/bit to achieve 0.1% conversion efficiency. This compares with 1.1 pJ/bit for 0.8% conversion efficiency [5] and 1.7 pJ/bit for 0.06% conversion efficiency [6] for FWM single bit extraction in silicon and chalcogenide waveguides.

For high-bit-rate OTDM demultiplexing, for example, from 1 Tbit/s to 50×20 Gbit/s, our current slab PPLN waveguide T-S setup would require an average pump power of around 5 W. Clearly this is a higher than the acceptable pump power requirement for practical OTDM demultiplexing. In order to reduce the pump power, the T-S conversion efficiency could be increased by less tight focusing (in the horizontal direction) of the signal and reference spectral components, allowing for extended Rayleigh interaction range in a lengthened slab PPLN waveguide. This can be achieved by employing longer focal length lenses; however, this would increase the overall footprint of the system.

Finally, high-resolution T-S conversion may be exploited in a number of applications, including single-shot imaging of ultrashort temporal waveforms for investigating femtosecond time scale molecular dynamics and single wavelength channel photonically assisted analog-to-digital conversion, for which reference power is not a major concern, but having large conversion efficiency and signal strength are.

References

1. T. Richter, E. Palushani, C. Schmidt-Langhorst, R. Ludwig, L. Molle, M. Nolle, and C. Schubert, J. Lightwave Technol. **30**, 504 (2012).
2. B. C. Wang, V. Baby, W. Tong, L. Xu, M. Friedman, R. J. Runser, I. Glesk, and P. R. Prucnal, Opt. Express **10**, 15 (2002).
3. J. Du, Y. Dai, G. K. P. Lei, and C. Shu, Opt. Express **18**, 18691 (2010).
4. Y. L. Lee, H. Suche, Y. H. Min, J. H. Lee, W. Grundkotter, V. Quiring, and W. Sohler, IEEE Photon. Technol. Lett. **15**, 978 (2003).
5. F. Li, M. Pelusi, D.-X. Xu, A. Densmore, R. Ma, S. Janz, and D. J. Moss, Opt. Express **18**, 3905 (2010).
6. M. Galili, J. Xu, H. C. Mulvad, L. K. Oxenløwe, A. T. Clausen, P. Jeppesen, B. Luther-Davis, S. Madden, A. Rode, D.-Y. Choi, M. Pelusi, F. Luan, and B. J. Eggleton, Opt. Express **17**, 2182 (2009).
7. R. Takahashi, T. Yasui, J. Seo, and H. Suzuki, IEEE J. Sel. Top. Quantum Electron. **13**, 92 (2007).
8. E. Palushani, H. C. H. Mulvad, M. Galili, H. Hu, L. K. Oxenlowe, A. T. Clausen, and P. Jeppesen, IEEE J. Sel. Top. Quantum Electron. **18**, 681 (2012).
9. K. G. Petrillo and M. A. Foster, Opt. Express **21**, 508 (2013).
10. P.-C. Sun, Y. T. Mazurenko, and Y. Fainman, J. Opt. Soc. Am. A **14**, 1159 (1997).
11. A. M. Kan'an and A. M. Weiner, J. Opt. Soc. Am. B **15**, 1242 (1998).
12. D. M. Marom, D. Panasenko, P.-C. Sun, and Y. Fainman, J. Opt. Soc. Am. A **18**, 448 (2001).
13. J.-H. Chung and A. M. Weiner, J. Lightwave Technol. **21**, 3323 (2003).
14. D. Shayovitz and D. M. Marom, Opt. Lett. **36**, 1957 (2011).
15. D. Shayovitz, H. Herrmann, W. Sohler, R. Ricken, C. Silberhorn, and D. M. Marom, Opt. Express **20**, 27388 (2012).
16. D. Shayovitz, H. Herrmann, W. Sohler, R. Ricken, C. Silberhorn, and D. M. Marom, in *Conference on Lasers and Electro-Optics (CLEO 2013)*, OSA Technical Digest (online) (Optical Society of America, 2013), paper CTu3E.2.

Chapter 4: Full-field measurement of ultrashort pulses

Whilst the work presented here so far has focused on developing time-to-space conversion as a demultiplexer for OTDM optical communications, it is in fact a general technique for transferring time domain information onto the spatial domain for ease of detection. It can therefore be used for ultrashort pulse measurement, where optoelectronic photodetectors lack the necessary bandwidth to resolve sub-picosecond temporal features. By mapping the temporal waveform onto a spatial dimension, an array of photodetectors or a camera can be used to record the original pulse intensity envelope with high spatial resolution. However, as mentioned in Chapter 1.4, an intensity-only measurement discards important information about the waveform which is contained in the phase. The time-to-space conversion process converts this temporal phase to a spatial phase on the generated SFG wave. In the case of a linear temporal phase (i.e. a time delay between the signal waveform and the reference pulse), the spatial phase of the SFG wave is also linear and so is converted by the output Fourier lens to a transverse spatial shift of the waveform image. In the case of a quadratic temporal phase the spatial phase of the SFG wave is also quadratic, resulting in a defocus of the pulse image at the output image plane.

Whilst this image defocus has been shown to give an indication of the presence and magnitude of frequency chirp on an ultrashort pulse [13, 14], an immediate and simultaneous recording of the converted complex field (i.e. amplitude and phase) would be preferable. This is made possible by the narrow bandwidth of the SFG output carrying the time-to-space converted phase information, allowing interferometric phase detection using a narrow-linewidth local oscillator. Section 4.1 and paper 4A describe the results of full-field measurement experiments by time-to-space conversion of ultrashort pulse packets and frequency chirped pulses. Section 4.2 and paper 4B present the experimental demonstration of real-time phase detection of a phase-modulated pulse train.

4.1 Pulse packet and chirped pulse full-field measurement

Two full-field measurement experiments by time-to-space conversion were performed: the first on a linearly phase-modulated pulse packet consisting of two bandwidth-limited ultrashort pulses and the second on quadratically phase-modulated and temporally stretched pulses. The experimental setups used to apply linear and quadratic phase modulation to the signal pulse are detailed below, but first the generation of the local oscillator (LO) is described.

Since optoelectronic photodetectors and cameras respond only to intensity, any phase measurement must be performed by first converting phase variations into intensity variations. This is typically done by interfering the phase information-carrying signal wave with a featureless reference wave (i.e. the local oscillator) at the same frequency. When the signal and LO waves are superimposed in space their instantaneous field amplitudes are combined, giving constructive interference where they are in phase and destructive interference where they are out of phase. The resulting spatial intensity variations (interference fringes) are recorded by the CMOS camera, thus creating an interferogram from which the field amplitude and phase of the signal wave can be extracted. In order to obtain high visibility interference fringes the LO should have precisely the same frequency as the signal wave and should also have as narrow a linewidth as possible. Typically a CW laser is used, however in the experiments described below the LO was generated by spectral filtering of the mode-

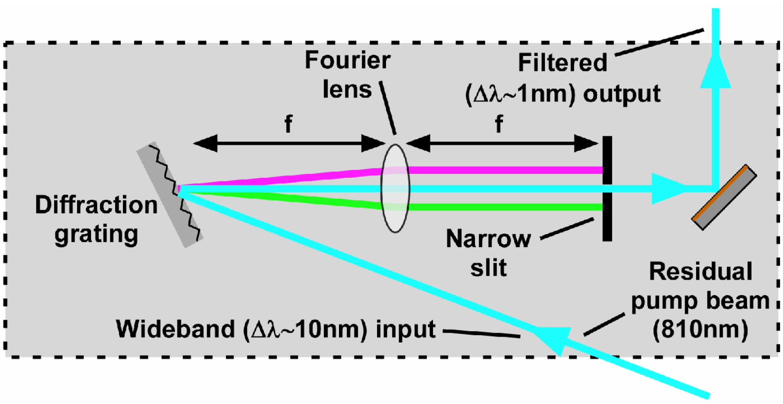

Fig. 4.1: LO generation by spectral filtering of the residual pump pulse. The sub-ps broadband residual pump pulse which exits the OPO is centred at 810 nm and has an FWHM bandwidth of ~10 nm. The pulse is incident on a diffraction grating which angularly disperses the various frequency components. A Fourier lens then converts the angular dispersion to a linear spatial dispersion of focused frequency components at the Fourier plane. Here a 20 μm wide slit blocks all spectral components except for a 1 nm bandwidth centred at 810 nm. The spectrally filtered (and temporally stretched) LO is then directed towards the CMOS camera to interfere coherently with the SFG phase-carrying signal.

locked laser residual pump pulse. The residual pump is the part of the MLL pulse which does not get converted to signal and reference light by DFG in the OPO; instead it exits from the OPO and can be used as a separate source of sub-ps pulses at 810 nm. Since the residual pump pulses have a broad bandwidth of approximately 10 nm (FWHM), it was necessary to narrow this spectral content down to approximately 1 nm by spectral filtering. Figure 4.1 shows the LO spectral filtering setup. The residual pump pulses are spatially dispersed by a diffraction grating and Fourier lens pair (as described in section 1.2) and a 20 μm wide slit is then used to block all frequency components except those in a 1 nm (FWHM) bandwidth centred around 810 nm. Note that this is wider than the 0.1 nm bandwidth of the SFG light. This was done intentionally to avoid interference fringes due to the LO alone, which were initially observed on the camera. The LO light was incident on the camera at a small angle from above in order to intersect the SFG beam and create a spatial interference pattern with the time-to-space converted pulse image.

The pulse packet used for the linear phase modulation experiment was generated by using an unbalanced Mach-Zehnder interferometer to split the signal pulse at 1550 nm emerging from the OPO into two copies (see Fig. 4.2). One copy (not phase-modulated) passed through a delay line in order to adjust the temporal offset between the two pulses. The other copy passed through a rotating glass slide which was used to apply a linear phase to the pulse. This controllable differential phase between the modulated and unmodulated pulses was the target for detection in this experiment.

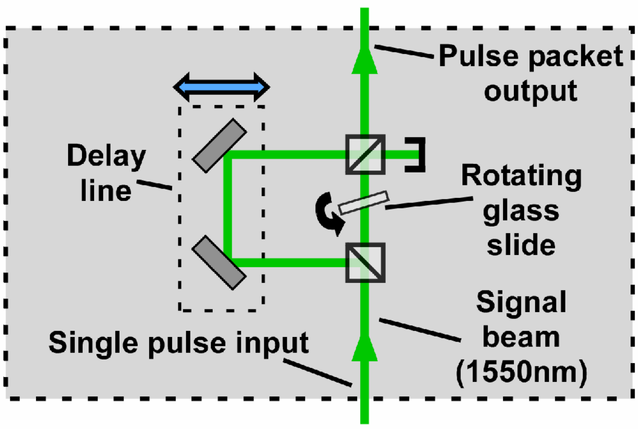

Fig. 4.2: Pulse packet generation. The signal pulse at 1550 nm from the OPO is split into two copies by a beamsplitter. One copy (unmodulated) passes through a delay line and the other copy receives a linear phase applied by a rotating glass slide. The two pulses are then re-formed into a single beam at the second beamsplitter, with a few picoseconds time delay between them. The double pulse is then directed via a delay line to the time-to-space converter.

The signal pulse packet then passed through another delay line and entered the time-to-space converter along with a reference pulse at 1697 nm. The time-to-space conversion setup used was the same as that described in Chapter 2B, with a bulk PPLN nonlinear crystal. The resulting SFG wave carrying the temporal amplitude and phase information was focused to the CMOS camera where the double pulse image was observed. The LO beam was also directed onto the camera at a small angle and horizontal interference fringes were observed on the pulse images.

For the quadratic phase modulation experiment, frequency chirp was applied to the signal pulses using a four-pass pulse stretcher (see Fig. 4.3). The bandwidth-limited incoming signal pulse is dispersed by a diffraction grating and Fourier lens pair, with the dispersed spectrum incident on the mirror. When the lens-grating distance *d* equals the lens focal length *f* there is no applied quadratic phase and the pulse exiting the pulse stretcher is still bandwidth-limited (this is known as the pulse stretcher 'null position'). In order to apply quadratic phase to the pulse the mirror and lens are together displaced along the optical axis with respect to the grating (note that the lens-to-mirror distance is fixed), causing the Fourier plane at the mirror to become curved [50]. This means that each spectral component travels a different total distance through the pulse stretcher, thereby acquiring a differential path length or phase. This phase varies quadratically across the pulse spectrum; equivalent to a linear frequency chirp in which each frequency component has a different time delay with respect to the pulse envelope, thus stretching the pulse in time. The direction and magnitude of

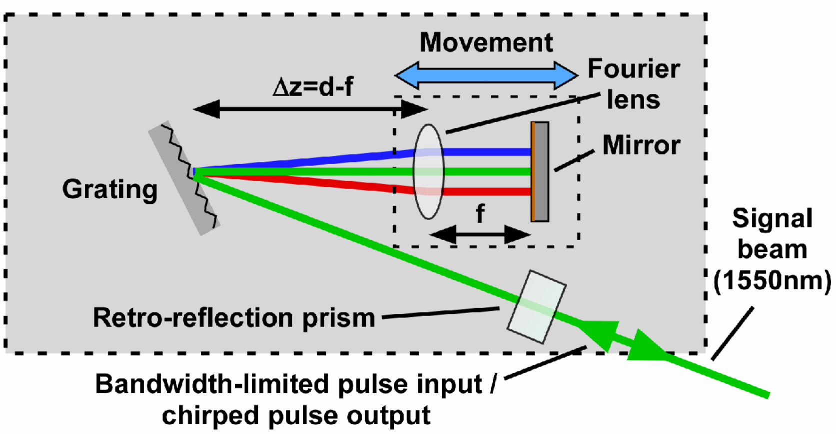

Fig. 4.3: Pulse stretcher for applying quadratic phase modulation. By displacing the lens and mirror with respect to the diffraction grating, positive or negative quadratic phase of varying magnitude can be applied to the dispersed frequency components. This is equivalent to a linear frequency chirp and also results in temporal stretching of the pulse.

the chirp simply depend on the direction and extent of the displacement of the mirror and lens. In this way a controllable quadratic phase can be applied to the signal pulse. The four-pass configuration is in order to ensure that the spatio-temporal coupling inside the pulse stretcher is undone for the output pulse. The chirped pulse is then time-to-space converted and its pulse image viewed on the camera, along with the curved fringe interference pattern due to the LO beam as described above.

In order to recover the amplitude and phase information from the phase modulated pulses in the experiments described above, the interference patterns recorded by the camera were Fourier transformed to the spatial frequency domain on a PC. Single sideband (SSB) filtering was then applied to eliminate the DC component and one of the sidebands. The filtered spatial frequency image was then inverse Fourier transformed back to the spatial domain and the time-dependant amplitude and phase were extracted.

4.2 Real time phase demodulation of ultrashort pulses by time-to-space conversion

The phase modulation experiments described above were designed to show proof of principle of time-to-space conversion for full-field measurement of ultrashort pulses. Phase recovery is also important in the context of time-to-space conversion as a potential OTDM demultiplexing technique for optical communications. As mentioned in section 1.3 advanced modulation formats such as QPSK, where data is encoded on the phase of the optical wave, are typically used together with OTDM to increase the bit rate and spectral efficiency. Therefore it is imperative that an OTDM demultiplexing method is compatible with coherent detection of phase information.

The phase detection experiments described in section 4.1 were both based on slow phase modulation of the signal pulses. The phase modulation applied, whilst it could be varied between measurements, did not change in time with respect to the individual signal pulses. Furthermore, the detection stage was also 'slow' since the time-averaging CMOS camera recorded the incident optical intensity over a span of a few milliseconds. Therefore a few hundred thousand time-to-space converted pulse images were incident on the camera for each recorded snapshot (the repetition rate of the signal pulses from the OPO was approximately 80 MHz). Since the phase modulation was slow in these experiments, the detection stage could also be slow without affecting the results. However, in an optical communications link a pseudo-random bit sequence is amplitude and phase-modulated onto the optical carrier in real time and must also be detected in real time. Clearly another experiment is required to show proof of principle for time-to-space conversion as a potential candidate for OTDM demultiplexing.

This experiment was performed by replacing the slow phase modulation setups described above with an electro-optic phase modulator which could be driven with an RF sinusoidal signal. At the same time the time-averaging camera at the output of the time-to-space processor was replaced with a fast photodetector for real-time coherent detection of the SFG light mixed with the LO. The phase modulator used was based on the linear electro-optic effect (Pockels effect) in a KTP crystal. By applying an electric field across the crystal transverse to the optical axis, its refractive index changes and so light passing through the crystal experiences an increased phase delay.

The applied voltage can be reversed periodically with a sinusoid function at RF frequencies, resulting in a time-varying phase modulation of the signal pulse train.

In the experiment described in paper 4B, a true pulse-to-pulse π phase swing was not possible, since the maximum driving frequency which could be applied to the phase modulator was limited to around 500 kHz (compared to the 80 MHz repetition rate of the signal pulses). This meant that the sinusoidal phase modulation was applied to the pulse train as a whole, rather than individual pulses. In addition the maximum modulation depth attained was approximately 1.5 radians; ideally it would have been π radians. This was due to the dependence of the magnitude of the Pockels effect on the applied electric field, which is equal to the applied voltage divided by the crystal width. Since the signal pulses to be modulated propagated in free-space (as opposed to in a waveguide), the crystal width had to be relatively large to allow a sufficient clear aperture of 2 mm for the free-space beam, thus limiting the modulation depth. However enough phase modulation was applied to give a detectable signal after time-to-space conversion.

The phase-modulated signal pulse train was time-to-space converted in the same setup as described in section 4.1 above. In order to sensitively detect the phase modulation that was transferred to the SFG wave, a technique known as balanced homodyne detection was employed. The SFG light was coupled into a single mode fibre via a fibre collimator and the LO light at the same wavelength was coupled via another collimator into a separate single mode fibre. The two fibres were connected to a 3 dB fibre coupler which combined the SFG and LO light into each of its two outputs, with a $\pi/2$ relative phase shift between them (see Fig. 4.4). This converts the phase modulation of the SFG light into an intensity modulation; when the SFG and LO are in phase their combined optical power exits via one output and when they are out of phase the optical power exits via the other output. The fibre coupler outputs were then connected to the two photodiodes of a 350 MHz bandwidth silicon balanced photodetector. The two photodiodes generated photocurrents $I_{+,-}$ proportional to the incident optical power, but with opposite polarities, as shown in Eqns 4.1 [51]:

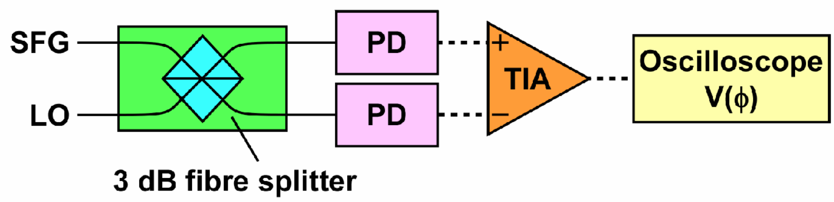

Fig. 4.4: Balanced coherent detection setup. The phase-modulated signal and LO are coupled into a 3 dB fibre splitter which combines the two waves. These are then incident on photodiodes which generate photocurrents proportional to the incident optical power, but with opposite polarities. The transimpedance amplifier sums the electrical signals, thus cancelling out the DC components from each photodiode, whilst passing the RF component. The output phase-dependent voltage is displayed on the oscilloscope.

$$I_{+} = S\left(\frac{1}{2}\left(P_{SFG} + P_{LO}\right) + \sqrt{P_{SFG}P_{LO}}\sin\left(\phi(t)\right)\right) \tag{4.1a}$$

$$I_{-} = -S\left(\frac{1}{2}\left(P_{SFG} + P_{LO}\right) - \sqrt{P_{SFG}P_{LO}}\sin\left(\phi(t)\right)\right) \tag{4.1b}$$

where S is the photodiode spectral responsivity (which is simply a constant for light of a particular wavelength), P_{SFG} and P_{LO} are the SFG and LO optical powers respectively coupled into the fibre collimators (assuming negligible insertion loss at the 3 dB fibre coupler) and $\phi(t)$ is the original phase modulation applied to the signal pulses (assuming a non time-varying phase of the LO light which is here set to zero for convenience). Note that here we have assumed that the SFG and LO optical frequencies are identical. By summing these two photocurrents and converting them to a voltage in a transimpedance amplifier, the constant SFG and LO terms cancel out and we are left with an electrical signal $V(\phi)$ which represents the original time-varying phase modulation:

$$V(\phi) = 2GS\sqrt{P_{SFG}P_{LO}}\sin\left(\phi(t)\right) \tag{4.2}$$

where G is the electrical gain provided by the transimpedance amplifier. Note that a significant advantage of balanced homodyne detection is that the signal-to-noise ratio can be enhanced by using a high power local oscillator, effectively providing gain for a weak signal of interest (in this case the SFG wave). The voltage in Eqn 4.2 is then amplified and the result recorded by a 12 GHz bandwidth oscilloscope, completing the phase demodulation.

Chapter 4A

Full-field reconstruction of ultrashort waveforms by time to space conversion interferogram analysis

Dror Shayovitz, Harald Herrman, Wolfgang Sohler, Raimund Ricken, Christine Silberhorn and Dan M. Marom

Published in Optics Express:

D. Shayovitz, H. Herrman, W. Sohler, R. Ricken, C. Silberhorn and D. M. Marom, "Full-field reconstruction of ultrashort waveforms by time to space conversion interferogram analysis," Opt. Exp. **22**, 20205-20213 (2014).

Full-field reconstruction of ultrashort waveforms by time to space conversion interferogram analysis

Dror Shayovitz,[1,*] Harald Herrmann,[2] Wolfgang Sohler,[2] Raimund Ricken,[2] Christine Silberhorn,[2] and Dan M. Marom[1]

[1]*Department of Applied Physics, Hebrew University of Jerusalem, Jerusalem, 91904, Israel*
[2]*Department of Applied Physics, The University of Paderborn, Warburger Str. 100 D-33098, Paderborn, Germany*
**dror.shayovitz@mail.huji.ac.il*

Abstract: Accurate amplitude and phase measurements of ultrashort optical waveforms are essential for their use in a wide range of scientific disciplines. Here we report the first demonstration of full-field optical reconstruction of ultrashort waveforms using a time-to-space converter, followed by a spatial recording of an interferogram. The algorithm-free technique is demonstrated by measuring ultrashort pulses that are widely frequency chirped from negative to positive, as well as phase modulated pulse packets. Amplitude and phase measurements were recorded for pulses ranging from 0.5 ps to 10 ps duration, with measured dimensionless chirp parameter values from −30 to 30. The inherently single-shot nature of time-to-space conversion enables full-field measurement of complex and non-repetitive waveforms.

OCIS codes: (320.0320) Ultrafast optics; (190.0190) Nonlinear optics.

References and links

1. C. I. Blaga, J. Xu, A. D. DiChiara, E. Sistrunk, K. Zhang, P. Agostini, T. A. Miller, L. F. DiMauro, and C. D. Lin, "Imaging ultrafast molecular dynamics with laser-induced electron diffraction," Nature **483**(7388), 194–197 (2012).
2. B. E. Van Kuiken, N. Huse, H. Cho, M. L. Strader, M. S. Lynch, R. W. Schoenlein, and M. Khalil, "Probing the electronic structure of a photoexcited solar cell dye with transient x-ray absorption spectroscopy," J. Phys. Chem. Lett. **3**, 1695–1700 (2012).
3. R. S. Pillai, C. Boudoux, G. Labroille, N. Olivier, I. Veilleux, E. Farge, M. Joffre, and E. Beaurepaire, "Multiplexed two-photon microscopy of dynamic biological samples with shaped broadband pulses," Opt. Express **17**(15), 12741–12752 (2009).
4. W. Ng, T. D. Rockwood, G. A. Sefler, and G. C. Valley, "Demonstration of a large stretch-ratio (M = 41) photonic analog-to-digital converter with 8 ENOB for an input signal bandwidth of 10 GHz," IEEE J. Photon. Technol. Lett. **24**(14), 1185–1187 (2012).
5. T. Richter, E. Palushani, C. Schmidt-Langhorst, R. Ludwig, L. Molle, M. Nölle, and C. Schubert, "Transmission of Single-Channel 16-QAM Data Signals at Terabaud Symbol Rates," J. Lightwave Technol. **30**(4), 504–511 (2012).
6. J. T. Willits, A. M. Weiner, and S. T. Cundiff, "Line-by-line pulse shaping with spectral resolution below 890 MHz," Opt. Express **20**(3), 3110–3117 (2012).
7. D. J. Kane and R. Trebino, "Single-shot measurement of the intensity and phase of an arbitrary ultrashort pulse by using frequency-resolved optical gating," Opt. Lett. **18**(10), 823–825 (1993).
8. D. J. Kane, R. Trebino, K. W. DeLong, D. N. Fittinghoff, J. N. Sweetser, M. A. Krumbugel, and B. A. Richman, "Measuring ultrashort laser pulses in the time-frequency domain using frequency-resolved optical gating," Rev. Sci. Instrum. **68**(9), 3277–3295 (1997).
9. L. Xu, E. Zeek, and R. Trebino, "Simulations of frequency-resolved optical gating for measuring very complex pulses," J. Opt. Soc. Am. B **25**(6), 70–80 (2008).
10. P. O'Shea, M. Kimmel, X. Gu, and R. Trebino, "Highly simplified device for ultrashort-pulse measurement," Opt. Lett. **26**(12), 932–934 (2001).
11. D. Meshulach, D. Yelin, and Y. Silberberg, "Real-time spatial–spectral interference measurements of ultrashort optical pulses," J. Opt. Soc. Am. B **14**(8), 2095–2098 (1997).
12. C. Iaconis and I. A. Walmsley, "Spectral phase interferometry for direct electric-field reconstruction of ultrashort optical pulses," Opt. Lett. **23**(10), 792–794 (1998).

#213096 - $15.00 USD Received 23 Jun 2014; revised 4 Aug 2014; accepted 4 Aug 2014; published 13 Aug 2014

13. P. Bowlan, P. Gabolde, A. Shreenath, K. McGresham, R. Trebino, and S. Akturk, "Crossed-beam spectral interferometry: a simple, high-spectral-resolution method for completely characterizing complex ultrashort pulses in real time," Opt. Express **14**(24), 11892–11900 (2006).
14. K. W. DeLong, D. N. Fittinghoff, and R. Trebino, "Practical issues in ultrashort-laser-pulse measurement using frequency-resolved optical gating," IEEE J. Quantum Electron. **32**(7), 1253–1264 (1996).
15. B. H. Kolner, "Space-time duality and the theory of temporal imaging," IEEE J. Quantum Electron. **30**(8), 1951–1963 (1994).
16. M. A. Foster, R. Salem, D. F. Geraghty, A. C. Turner-Foster, M. Lipson, and A. L. Gaeta, "Silicon-chip-based ultrafast optical oscilloscope," Nature **456**(7218), 81–84 (2008).
17. C. Dorrer, "Single-shot measurement of the electric field of optical waveforms by use of time magnification and heterodyning," Opt. Lett. **31**(4), 540–542 (2006).
18. A. Zeytunyan, A. Muradyan, G. Yesayan, L. Mouradian, F. Louradour, and A. Barthélémy, "Generation of broadband similaritons for complete characterization of femtosecond pulses," Opt. Commun. **284**(15), 3742–3747 (2011).
19. N. K. Fontaine, R. P. Scott, L. Zhou, F. M. Soares, J. P. Heritage, and S. J. B. Yoo, "Real-time full-field arbitrary optical waveform measurement," Nat. Photonics **4**(4), 248–254 (2010).
20. Y. T. Mazurenko, S. E. Putilin, A. G. Spiro, A. G. Beliaev, V. E. Yashin, and S. A. Chizhov, "Ultrafast time-to-space conversion of phase by the method of spectral nonlinear optics," Opt. Lett. **21**(21), 1753–1755 (1996).
21. P.-C. Sun, Y. T. Mazurenko, and Y. Fainman, "Femtosecond pulse imaging: ultrafast optical oscilloscope," J. Opt. Soc. Am. A **14**(5), 1159–1170 (1997).
22. K. Oba, P. C. Sun, Y. T. Mazurenko, and Y. Fainman, "Femtosecond single-shot correlation system: a time-domain approach," Appl. Opt. **38**(17), 3810–3817 (1999).
23. A. M. Kan'an and A. M. Weiner, "Efficient time-to-space conversion of femtosecond optical pulses," J. Opt. Soc. Am. B **15**(3), 1242–1245 (1998).
24. D. M. Marom, D. Panasenko, P.-C. Sun, and Y. Fainman, "Linear and nonlinear operation of a time-to-space processor," J. Opt. Soc. Am. A **18**(2), 448–458 (2001).
25. J.-H. Chung and A. M. Weiner, "Real-time detection of femtosecond optical pulse sequences via time-to-space conversion in the lightwave communications band," J. Lightwave Technol. **21**(12), 3323–3333 (2003).
26. D. M. Marom, D. Panasenko, P.-C. Sun, Y. T. Mazurenko, and Y. Fainman, "Real-time spatial-temporal signal processing with optical nonlinearities," IEEE J. Sel. Top. Quantum Electron. **7**(4), 683–693 (2001).
27. D. Shayovitz and D. M. Marom, "High-resolution, background-free, time-to-space conversion by collinearly phase-matched sum-frequency generation," Opt. Lett. **36**(11), 1957–1959 (2011).
28. D. Shayovitz, H. Herrmann, W. Sohler, R. Ricken, C. Silberhorn, and D. M. Marom, "High resolution time-to-space conversion of sub-picosecond pulses at 1.55µm by non-degenerate SFG in PPLN crystal," Opt. Express **20**(24), 27388–27395 (2012).
29. D. Shayovitz, H. Herrmann, W. Sohler, R. Ricken, C. Silberhorn, and D. M. Marom, "Time-to-space conversion of ultrafast waveforms at 1.55 µm in a planar periodically poled lithium niobate waveguide," Opt. Lett. **38**(22), 4708–4711 (2013).
30. M. T. Kauffman, W. C. Banyai, A. A. Godil, and D. M. Bloom, "Time-to-frequency converter for measuring picosecond optical pulses," Appl. Phys. Lett. **64**(3), 270–272 (1994).
31. L. Kh. Mouradian, F. Louradour, V. Messager, A. Barthélémy, and C. Froehly, "Spectro-temporal imaging of femtosecond events," IEEE J. Quantum Electron. **36**(7), 795–801 (2000).
32. G. P. Agrawal, *Fiber-Optic Communication Systems*, 3rd ed. (John Wiley & Sons, 2002).
33. D. Shayovitz, H. Herrmann, W. Sohler, R. Ricken, C. Silberhorn, and D. M. Marom, "Coherent detection of phase modulated ultrashort optical pulses using time-to-space conversion at 1.55µm," in *CLEO: 2014*, OSA Technical Digest (online) (Optical Society of America, 2014), paper STu2I.3.

1. Introduction

Ultrashort optical pulses are used in many areas of science and technology, for example the investigation of femtosecond time-scale molecular interactions [1, 2], multi-photon microscopy of dynamic biological samples [3], optical data processing [4] and optical communications [5]. Full-field measurement of ultrashort optical pulses is essential for understanding their generation, ascertaining their propagation properties and for pulse shaping applications [6]. For example, temporal phase measurement of a pulse can be used to determine whether it is bandwidth-limited or has undergone dispersive or nonlinear phase distortions. Optoelectronic photodetectors are unable to measure ultrashort (sub-picosecond) pulses, due to their limited electrical bandwidth of ~100 GHz in state of the art devices. Pulse measurement techniques are therefore typically based on optical nonlinear phenomena, which are effectively instantaneous on the femtosecond timescale.

The requirements for a successful ultrashort pulse full-field characterization technique include: unambiguous measurement of complex and non-symmetric pulses, single-shot measurement of non-repetitive pulses, a high record length-to-resolution ratio for long and complex waveforms and algorithm-free phase recovery to minimize post-processing and eliminate the problem of non-convergence.

Among the full-field characterization methods that have been investigated, frequency-resolved optical gating (FROG) [7–10] and spectral interferometry techniques [11–13] such as SPIDER are popular. However, the FROG technique requires a phase recovery algorithm whose run time rapidly increases for larger time-bandwidth product waveforms [14], while SPIDER's record length is limited by spectrometer resolution. Temporal magnification, following the analogy between short pulse dispersive propagation and free-space diffraction [15], can temporally stretch pulses to enable detection by conventional photodetectors [16] or to perform full-field measurement by interferometry in the time [17] or frequency [18] domains. This technique, however, is only single-shot within a time window limited by the stretched reference pulse duration. Optical arbitrary waveform measurement (OAWM) uses spectral slicing and digital coherent detection to achieve a record length-to-resolution ratio of >300,000 [19]. However, the requirement for a stable frequency comb and multiple high-speed receivers and digitizers reduces the practical utility of this method.

2. Full-field measurement by time-to-space conversion

Time-to-space (T-S) conversion realizes full-field measurement of ultrashort optical pulses by transferring the pulse's amplitude and phase information from the temporal domain to a spatial domain image. It is based on sum-frequency generation (SFG) between spatially dispersed signal and reference pulses, resulting in a quasi-monochromatic SFG wave which forms a spatial image of the signal pulse. Preservation of phase in the T-S conversion process has been shown experimentally using displaced image plane observations [20–22], and here we present the first interferometric phase measurements of T-S converted ultrashort pulses. T-S conversion has a number of attractive features including single-shot operation and unambiguous and algorithm-free amplitude and phase measurement.

The principle of operation of T-S conversion [21, 23–26] is illustrated in Fig. 1. The signal and reference pulses, at non-degenerate central wavelengths, are oppositely dispersed by diffraction gratings and are spatially resolved by a Fourier lens, such that their spectra are superimposed at the Fourier plane with equal magnitude and opposite direction linear spatial dispersions. By placing a $\chi^{(2)}$ nonlinear crystal at this plane, SFG occurs between overlapping frequency components of the dispersed signal and reference pulses at each point in space. Due to the matched yet flipped spatial dispersions, a spatially coherent narrow frequency SFG wave is generated all along the crystal aperture, phase-matched across the bandwidth of the dispersed pulses. Temporal walk-off within the nonlinear medium, which can cause distortions in ultrashort pulse measurement, is negligible since the spectrally resolved pulses have extended duration in time.

Time delays between the signal waveform and reference pulse result in linear spectral phases which are converted to linear spatial phases of the quasi-monochromatic SFG wave. A second Fourier lens after the nonlinear crystal converts this linear phase to a transverse spatial shift of the waveform image at the output plane. The instantaneous output field is a quasi-static spatial image of the signal temporal waveform [26]:

$$U_{out}(x,t) = w\left(-\frac{c(t-t_0)}{\alpha}\right)\cdot w\left(\frac{ct}{\alpha}\right)\cdot s\left(\frac{\alpha x}{c}-t_0\right)\otimes r\left(-\frac{\alpha x}{c}\right)\cdot \exp\left(-j(\omega_S+\omega_R)t\right) \quad (1)$$

where $s(\bullet)$ and $r(\bullet)$ are the functional forms of the signal and reference input temporal waveforms, mapped to the output plane spatial coordinate x, $w(\bullet)$ is the spatial width of the input beams striking the grating (assumed equal), mapped to the time duration for which the pulse is present and which forms the temporal aperture of the processor and its spectral resolution, $\omega_{S,R}$ are the signal and reference pulse central angular frequencies respectively, α is the dispersion parameter, c is the speed of light, t_0 is the time delay of the signal pulse with respect to the reference pulse and $\otimes$ is the convolution operator. The use of signal and reference pulses at non-degenerate center wavelengths enables spectral filtering of the output

#213096 - $15.00 USD Received 23 Jun 2014; revised 4 Aug 2014; accepted 4 Aug 2014; published 13 Aug 2014

light to block SHG background [27]. The instantaneous time-to-space mapped output field is typically incident on a camera which records the converted time integrated signal intensity without the phase information [23–25, 27–29]. However, the temporal phase of the signal waveform is contained in the output spatial image, which we demonstrate here by recording the interference with a plane wavefront at the same center wavelength. Phase information can then be extracted from the resulting interference fringes.

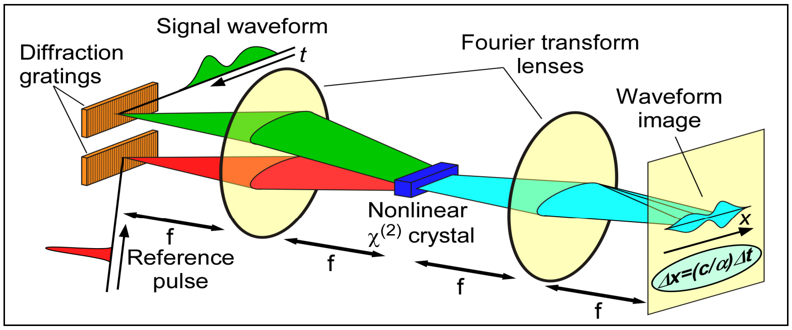

Fig. 1. Time-to-space conversion concept. Time domain information is converted to a spatial image with the temporal coordinate mapped directly to a spatial coordinate: $\Delta x = (c/\alpha)\Delta t$, where c is the speed of light and α is the dispersion parameter (see Eq. (1). Note that in our experimental setup the signal and reference beams propagated collinearly in the nonlinear crystal, whereas here they are shown at crossed angles for clarity.

It is interesting to note the parallels between time-to-space conversion and time-to-frequency (T-F) conversion [15–18, 30, 31]. T-S conversion mixes the spatially dispersed temporal frequency components of the signal and reference pulses, converting the temporal frequency information to spatial frequencies, and then optically Fourier transforms the spatial frequency information to obtain a space-domain image of the temporal waveform. T-F conversion mixes the temporally dispersed frequency components of chirped signal and reference pulses, imprinting the signal pulse envelope shape onto the generated spectrum. Following this, further chromatic dispersion is applied to temporally resolve the spectral components for photodetection of the temporal intensity profile [16], or instead the T-F spectrum can be immediately measured with a spectrometer [30, 31]. The update rate of this measurement is limited in the first case by the temporal magnification factor and in the second case by the time-integrating spectrometer. T-S conversion, on the other hand, alleviates the temporal resolution problem of short pulse measurement by transferring the time domain envelope to a quasi-static spatial image, which can be recorded with high spatial resolution. The update rate of this measurement is determined by the T-S spectral resolution and by the reference pulse repetition rate, allowing for single-shot recording of long temporal waveforms (see the discussion in section 4).

3. Experiment and results

Figure 2 shows our experimental setup. A mode-locked laser (MLL) generated ~100 fs bandwidth-limited pulses at 810 nm with a repetition rate of 80.2 MHz. These were converted by an optical parametric oscillator (OPO) to 'signal' pulses at 1550 nm central wavelength (beam path shown in green) and 'reference' pulses at 1697 nm (shown in red). The signal pulse was directed to one of two phase modulation blocks, resulting in either the generation of a pulse pair with relative phase modulation or a single pulse with quadratic spectral phase modulation. The linear phase modulation block (Fig. 2(b)) consisted of an unbalanced Mach-Zehnder interferometer producing two pulse copies, where one copy passed through a 1 mm thick rotatable glass slide, generating $s(t) = p(t) + p(t\text{-}T_0)\exp(j\phi)$, where T_0 is the fixed time delay and ϕ is the modulated phase. The quadratic phase modulation block (Fig. 2(c)) comprised an imaging four-pass pulse stretcher which applied controllable chromatic dispersion, resulting in either positive, negative or zero frequency chirped pulse: $s(t)$ = exp(-

$(1 + jC)t^2/2\tau^2)$, where C is a dimensionless chirp parameter and 2τ is the full-width of the transform limited Gaussian shape pulse measured at e^{-1} intensity points [32]. The modulated signal pulse is then retimed to the reference pulse by a delay line, to coincide at the nonlinear crystal.

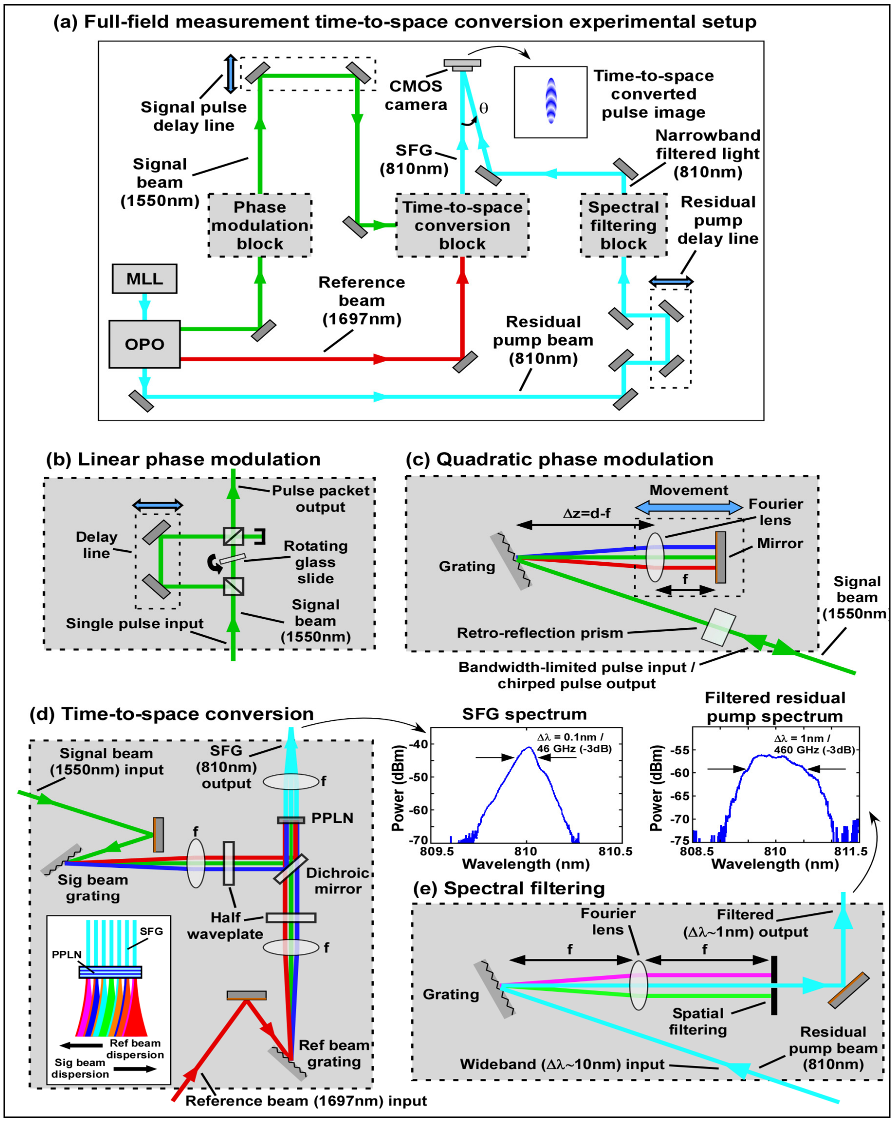

Fig. 2. Full-field measurement time-to-space conversion experimental setup. (a) Overall setup (MLL, mode-locked laser; OPO, optical parametric oscillator; SFG, sum-frequency generation); note that the filtered residual pump beam is incident on the camera at a small angle from above i.e. from out of the plane of the paper. (b) Linear phase modulation block. (c) Quadratic phase modulation block. (d) Time-to-space conversion block (f, Fourier lens; PPLN, periodically-poled lithium niobate). (e) Spectral filtering block for generating the interferogram reference plane wave. The SFG and filtered residual pump spectra are also shown.

The signal pulse was then spatially dispersed by a first diffraction grating (1100 line pairs/mm) and 75 mm focal length Fourier lens (Fig. 2(d)). At the same time the non-modulated reference pulse was given an equal but opposite spatial dispersion by a second diffraction grating (1000 line pairs/mm) and another 75 mm Fourier lens. The two dispersed

#213096 - $15.00 USD Received 23 Jun 2014; revised 4 Aug 2014; accepted 4 Aug 2014; published 13 Aug 2014

pulses were superimposed by a dichroic mirror and were incident on a periodically-poled lithium niobate (PPLN) nonlinear crystal located at the focal plane (see inset in Fig. 2(d)). The PPLN had a poling period of 20.3 μm and dimensions of 12 mm and 8 mm in the spatial dispersion direction and light propagation direction, respectively. The Rayleigh length of the focused signal and reference spectral components inside the PPLN was estimated as ~1 mm by measuring the spectral resolution and spatial dispersion of the light at the Fourier plane.

The signal and reference beams' average powers at the PPLN entrance face were measured as 82 mW and 95 mW respectively, resulting in pulse energies of 1 nJ and 1.2 nJ and peak powers of 22 W and 27 W respectively. The peak powers were calculated assuming that the dispersed signal and reference pulses at the Fourier plane were stretched through the time window, which was measured as 46 ps (FWHM). Phase-matched SFG at each point in space resulted in an up-converted output beam centered at 810 nm with a −3dB bandwidth of 0.1 nm (spectrum shown in Fig. 2).

As noted earlier, temporal walkoff due to group velocity mismatch (GVM) between the fundamental and SFG short pulses in a dispersive nonlinear medium can result in distortion of the output signal. For T-S conversion, however, SFG occurs between spatially dispersed pulses, where the spectral bandwidth present at each point in space along the nonlinear crystal aperture is greatly reduced. This effectively transforms the SFG interaction from one between ultrashort pulses subject to large temporal walkoff, into one between multiple quasi-monochromatic beamlets of light, each centered at a different frequency, which experience negligible temporal walkoff. For lithium niobate the GVM between the longest wavelength pulse (the reference pulse at 1697 nm) and the shortest wavelength pulse (the SFG pulse at 810 nm) is 140 fs/mm. Since the SFG interaction length in the PPLN was ~1 mm, this results in a temporal walkoff of 0.3% of the 46 ps time window (i.e. the stretched pulse duration).

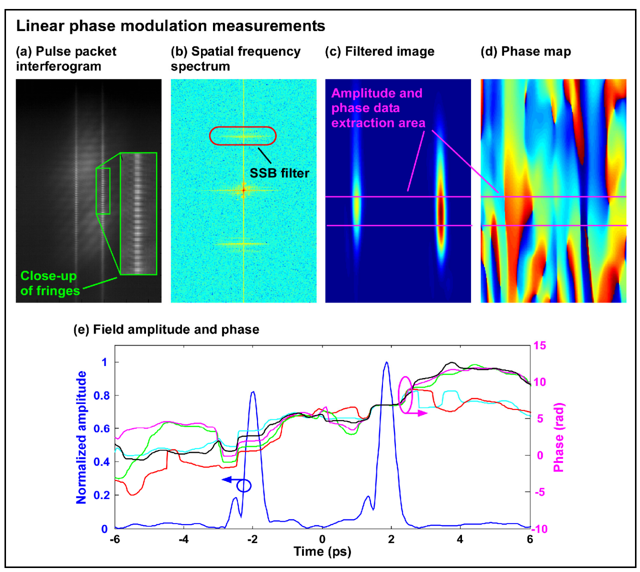

Fig. 3. Pulse packet full-field measurement. (a) Time-to-space converted pulse packet with close-up of the interference fringes. (b) Spatial frequency spectrum of the pulse packet with SSB filter indicated. (c) Inverse Fourier transform of the filtered image. (d) Recovered phase map. (e) Amplitude (blue) and phase (various colors) data taken from the region delimited by pink lines in (c) and (d). Five successive phase measurements are shown, each taken at a linearly increasing applied phase. The normalized field amplitude did not change significantly between successive measurements, so only one amplitude profile is shown here (taken from the same interferogram recording as the light blue line phase profile).

The SFG average beam power emerging from the PPLN was 45 μW (measured for the single unchirped signal pulse case). A 200 mm focal length output Fourier lens focused the SFG light onto a CMOS camera which recorded the pulse image. Next, we interfered the

#213096 - $15.00 USD Received 23 Jun 2014; revised 4 Aug 2014; accepted 4 Aug 2014; published 13 Aug 2014

pulse image with a plane wave having the same center wavelength as the SFG pulse, to extract the phase information. This reference plane wave was generated by spectrally filtering the MLL residual pump pulse exiting the OPO (Fig. 2(e)). The −3dB bandwidth of the filtered residual pump pulse was 1 nm (spectrum shown in Fig. 2). Another delay line temporally overlapped the filtered residual pump pulse and the SFG pulse on arrival at the camera. The reference wave was incident on the camera from above at a small angle to the SFG beam, resulting in the formation of stable interference fringes [33]. Figure 3(a) shows a T-S converted pulse packet interferogram, with fringes clearly visible. By applying single-sideband (SSB) filtering to the image's Fourier transform (Fig. 3(b)) and an inverse Fourier transform (Fig. 3(c)), both the field amplitude and phase were recovered (Figs. 3(d) and 3(e)). Successive phase measurements, shown in different colors in Fig. 3(e), recorded the phase shift of the modulated pulse. Note the flat phase over the two pulse envelopes, with the unmodulated pulse phase staying constant whilst the modulated pulse phase varies with each successive measurement. The small pre-pulses appearing immediately before each of the two main pulse peaks are time-to-space imaging aberrations due to distortions in the temporal intensity envelope of the idler (reference) pulse exiting the OPO.

The quadratic phase modulation experiment is shown in Fig. 4. Figure 4(a) shows an image of a negatively chirped pulse with curved interference fringes. The spatial frequency spectrum, SSB filtered pulse image and recovered phase are shown in Figs. 4(b)-(d), and the time-varying field and phase in Fig. 4(e). In this example a parabolic fit to the phase of the 1.5 ps pulse (FWHM of the intensity envelope) results in a dimensionless chirp parameter of −2. Measurements were made of positively chirped, bandwidth-limited and negatively chirped pulses. Figure 5 shows pulse duration and chirp parameter values for varying pulse stretcher offsets. Linear variation in pulse chirp with increasing pulse stretcher grating – lens offset can be seen, as well as the evolving pulse duration. The error bars are estimated from confidence bounds on the free parameters of the Gaussian and parabolic fits to the measured amplitude and phase respectively. Note that the chirp measurement error increases for smaller chirp values as the phase becomes flatter and the parabolic fit is less applicable. On the other hand the FWHM duration measurement error decreases for the less strongly stretched pulses, since the offset pulse stretcher introduces some distortions to the pulse envelope.

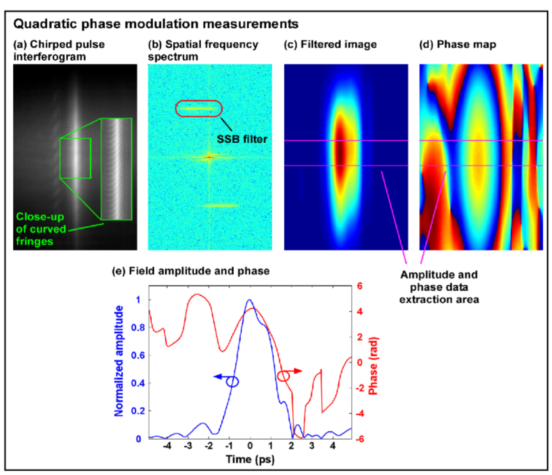

Fig. 4. Chirped pulse full-field measurement. (a) Time-to-space converted negatively chirped pulse interferogram. (b) Spatial frequency spectrum of pulse image. (c) SSB filtered image. (d) Recovered phase map showing quadratic phase variation over the pulse envelope. (e) Pulse field amplitude (blue) and phase (red) with a FWHM pulse duration of ~1.5 ps and chirp parameter of −2. Note that the distortion of the pulse shape seen in (c) and (e) is believed to be due to spatial distortions and spatio-temporal coupling in the pulse stretcher.

#213096 - $15.00 USD Received 23 Jun 2014; revised 4 Aug 2014; accepted 4 Aug 2014; published 13 Aug 2014

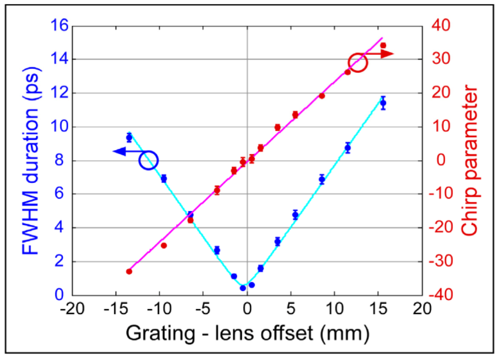

Fig. 5. Measured FWHM pulse duration (blue) and chirp (red) with varying pulse stretcher grating - lens offset, showing Gaussian beam radius evolution and linear fits respectively. The measured chirp clearly shows a linear variation with grating - lens offset. The grating - lens offset zero point (pulse stretcher null position) was determined by the fit to the pulse duration measurements.

4. Discussion and conclusion

The interferogram recording of time-to-space converted ultrashort waveforms reported here operated in real-time and allowed full-field reconstruction without resorting to complex algorithms for phase retrieval. We next discuss the system attributes of our processor.

An important parameter for a waveform measurement technique is the record length-to-resolution ratio, which determines the longest and most complex waveform that can be accurately measured. For T-S conversion the record length is set by the processor's time window, determined by the incident beam sizes on the diffraction gratings. As the time window is extended, by increasing the input beam size, the spectral resolution of the dispersive arrangement is refined and the resultant SFG signal bandwidth is reduced, which allows us to easily record a stable interferogram. We witness the fundamental inverse relationship between time window of operation and spectral bandwidth. In the experiment reported here the SFG bandwidth was measured as 46 GHz (−3dB), roughly in line with our 46 ps time window. In our experiment we acquire the interferogram with a camera operating at several ms integration times, thereby integrating over multiple, repetitive and identical converted signals, which still qualifies as real-time operation. Single-shot operation of the technique can be performed by using a lower repetition pulse source or time-gating a fast one such that a single pulse is incident on the image sensor within its integration time.

The temporal resolution of T-S conversion is determined by the reference pulse duration, as witnessed by the convolution operation in Eq. (1). Temporal features of the signal waveform that are shorter than the reference pulse duration will not be resolved. In our experiment the reference pulse duration was approximately 210 fs (FWHM) and the shortest T-S converted signal pulse was measured as 440 ($\pm$ 80) fs; this is the temporal resolution achieved in the work reported here. Whilst the reference pulse duration sets a fundamental limit on temporal resolution, an additional criterion is introduced by the pixel density on the image acquisition device. To properly record and maintain system resolution, we require that the pixel pitch be much smaller that the minimal spot size of a converted transform-limited ultrashort optical pulse. We may vary this spot size by selection of output Fourier lenses of different focal lengths.

As can be appreciated from the preceding discussion, some flexibility in determining the main performance parameters of T-S conversion can be afforded by changing aspects of the optical setup, such as the signal and reference beam sizes at the diffraction gratings, the reference pulse duration, and the output Fourier lens focal length. The conversion efficiency is also impacted by these choices, but this is not the main focus of this paper. Finally we note that T-S conversion is not a self-referencing technique since it requires a previously characterized reference pulse.

In conclusion, we have demonstrated full-field recovery by interferogram optical recording of ultrafast waveforms by time-to-space conversion. The temporal amplitude and phase were measured for bandwidth-limited and positively and negatively chirped pulses varying in duration from 0.5 ps to 10 ps. This technique may complement existing ultrashort pulse measurement methods such as FROG, which relies on an increasingly heavy algorithm for phase recovery of high time-bandwidth product measured waveforms [14]. Time-to-space conversion may be considered particularly for applications requiring algorithm-free and real-time measurement of complex waveforms with high record length-to-resolution ratio.

#213096 - $15.00 USD Received 23 Jun 2014; revised 4 Aug 2014; accepted 4 Aug 2014; published 13 Aug 2014

Chapter 4B

Real-time coherent detection of ultrashort pulses after time-to-space conversion and spatial demultiplexing

Dror Shayovitz, Harald Herrman, Wolfgang Sohler, Raimund Ricken, Christine Silberhorn and Dan M. Marom

Not published

Real-time coherent detection of ultrashort pulses after time-to-space conversion and spatial demultiplexing

Dror Shayovitz,[1] Harald Herrmann,[2] Wolfgang Sohler,[2] Raimund Ricken,[2] Christine Silberhorn,[2] and Dan M. Marom[1]

[1]*Department of Applied Physics, Hebrew University of Jerusalem, Jerusalem, 91904, Israel*
[2]*Department of Applied Physics, The University of Paderborn, Warburger Str. 100 D-33098, Paderborn, Germany*

Abstract: Sub-picosecond pulses are converted by a time-to-space processor to quasi-monochromatic spatial beams that are spatially demultiplexed and coherently detected in real-time. The time-to-space processor, based on sum-frequency generation (SFG), serves as a serial-to-parallel converter, reducing the temporal bandwidth of the ultrashort pulse to match the bandwidth of optoelectronic receivers. As the SFG process is phase preserving, we demonstrate homodyne coherent detection of phase modulated temporal pulses by mixing the demultiplexed SFG beam with a narrow linewidth local oscillator (LO) resulting in single-shot amplitude and phase detection of the pulse at a balanced detector. Positively and negatively phase-modulated signal pulses are individually detected and LO shot noise limited operation is achieved. This demonstration of real-time demultiplexing followed by single-shot full-field detection of individual pulses, highlights the potential of time-to-space conversion for ultrahigh bit rate optical communications and data processing applications.

The growth trend in global communications traffic shows no sign of slowing, whereas current optical communications networks based on wavelength division multiplexing (WDM) are nearing their available bandwidth limit [1]. In order to support continued growth it is increasingly necessary to exploit all available multiplexing and modulation degrees of freedom, such as polarization multiplexing and complex amplitude modulation. Advanced modulation formats such as quadrature phase shift keying (QPSK) together with coherent detection of the received signal may be employed. Indeed, recently deployed optical networks utilize polarization multiplexing and 2 bits-per-symbol modulation of an electronically generated 25 Gbaud/s serial channel to reach single-wavelength channel data rates of 100 Gb/s. Another advantage of coherent detection is apparent when it is combined with digital signal processing (DSP). This enables electronic compensation of linear distortions such as chromatic dispersion and polarization mode dispersion, and some nonlinear distortions such as cross-phase modulation (XPM) and four-wave mixing (FWM), undergone by short pulses propagating in optical fiber [2].

Optical time division multiplexing enables high bit rate data transmission whilst lowering the number of wavelength channels, thereby minimizing the number of laser sources required and reducing overall system management complexity. By combining OTDM with complex amplitude modulation a single-wavelength channel can be generated at greater than 1 Tb/s [3], exceeding the highest modulation rates in the electronic domain which are limited by device physics to <100 GHz. An OTDM channel is typically produced by using passive optical delay lines to interleave pulses from multiple low baud rate tributaries into unique time slots on a frame-by-frame basis. OTDM demultiplexing is more challenging and several demultiplexing techniques have been investigated. These include the nonlinear optical loop mirror [4, 5], XPM-based Mach-Zehnder switch [6, 7], FWM-based spectral filtering extraction [8, 9] and coherent detection by parallel optical sampling with a pulsed local oscillator [10]. All these methods however are limited to single bit extraction, with multiple devices needed to completely demultiplex the OTDM channel. Since the power consumption and overall complexity of the demultiplexing stage increase with each additional device, the scalability of these techniques to higher symbol rates is challenging. In addition the task of inter-device clock synchronisation, necessary in order to extract the correct tributary at each device, becomes difficult for higher bit rates.

Serial-to-parallel demultiplexing can overcome these problems by simultaneously extracting all the bits in an OTDM frame. With a single reference pulse performing the entire demultiplexing operation the problem of inter-device clock synchronization, as for single-bit extraction, becomes one of synchronizing the reference pulse to the several tens of picoseconds wide OTDM frame, a less onerous task. Serial-to-parallel demultiplexing has been successfully demonstrated by using time-to-frequency conversion, where the temporal pulse envelope is imprinted onto the spectrum of an FWM wave [11, 12]. However the resultant broadband signal makes phase extraction difficult. We propose and demonstrate the time-to-space conversion technique for serial-to-parallel demultiplexing of a high bit rate OTDM channel, including recovery of phase information by coherent detection of the demultiplexed narrowband pulses.

Time-to-space conversion is an all-optical demultiplexing technique based on spectrally-resolved sum-frequency generation (SFG) between a signal pulse stream and a single reference pulse. It works by transferring the spectrally broadband time domain information of the signal pulses to a spatial image formed by quasi-monochromatic SFG light [13-18]. By combining the gating effect of SFG with spectral processing techniques developed originally for ultrashort pulse shaping [19], time-to-space conversion can demultiplex a high bit rate OTDM channel to multiple parallel spatial channels for direct detection by an array of photoreceivers [18]. Alternatively, homodyne mixing of the quasi-monochromatic SFG light with a narrow linewidth local oscillator (LO) allows coherent detection of phase information, making demultiplexing by time-to-space conversion compatible with advanced modulation formats. We have previously demonstrated high resolution time-to-space conversion in bulk and slab waveguide nonlinear media [20-22], as well as phase measurements of time-to-space converted ultrashort waveforms by interferogram recording in the space domain [23]. Here we report real-time demultiplexing and single-shot coherent detection of phase-modulated sub-picosecond pulses at 1.55 μm. This result supports the potential of time-to-space conversion for high bit rate OTDM demultiplexing applications.

The principle of time-to-space conversion [15-18] is shown in Figure 1. The incoming OTDM signal bit stream and a single locally generated reference pulse, at non-degenerate central wavelengths, are given equal magnitude but opposite direction spatial dispersions by pairs of diffraction gratings and Fourier lenses. Their resolved spectra overlap in space at the Fourier plane, where a nonlinear $\chi^{(2)}$ crystal is located. SFG occurs between pairs of overlapping frequency components of the signal and reference spectra at each point in space. Due to the matched yet flipped spatial dispersions, each pair of overlapping frequency components adds up to the same sum-frequency. The result is a spatially coherent narrow bandwidth SFG wave generated along the entire crystal aperture, with automatic phase-matching across the bandwidth of the dispersed pulses. The temporal walk-off problem typically associated with ultrashort pulses in a dispersive nonlinear medium is negligible since the SFG interaction occurs between pairs of quasi-monochromatic beamlets, each at different frequencies, at the Fourier plane of the time-to-space processor.

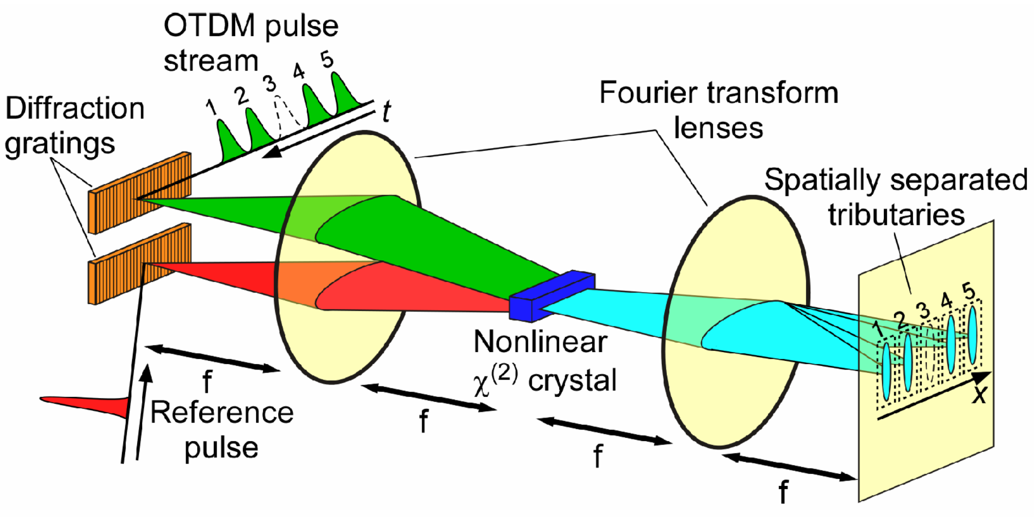

Fig. 1. Time-to-space conversion concept. Time domain information is converted to a spatial image with the temporal coordinate *t* mapped linearly to a spatial coordinate *x*. Note that in our experimental setup the signal and reference beams propagate collinearly in the nonlinear crystal, whereas here they are shown at crossed angles for clarity. The dashed line in the OTDM pulse stream represents an empty bit slot.

The time delay information between a signal pulse in the OTDM pulse stream and the reference pulse is carried by the spectral phase of the spatially dispersed waveforms, which is converted to a linear spatial phase on the generated SFG wave. A second Fourier lens after the nonlinear crystal coverts this linear phase on the quasi-monochromatic waveform to a transverse spatial shift of the focused pulse images at the output image plane. The result is a quasi-static spatial image of the signal pulse (assuming that the reference pulse has a much shorter temporal duration) [17]:

$$U_{out}(x,t) = w\left(-\frac{c(t-t_0)}{\alpha}\right)\cdot w\left(\frac{ct}{\alpha}\right)\cdot s\left(\frac{\alpha x}{c}-t_0\right)\otimes r\left(-\frac{\alpha x}{c}\right)\cdot \exp\left(-j(\omega_S+\omega_R)t\right) \tag{1}$$

where $s(\bullet)$ and $r(\bullet)$ are the functional forms of the signal and reference pulses, mapped to the output plane spatial coordinate x, $w(\bullet)$ is the beam aperture of the input waves forming the temporal aperture of the spectral processor, $\omega_{S,R}$ are the signal and reference pulse central angular frequencies respectively, α is the dispersion parameter, c is the speed of light, t_0 is the time delay of an individual signal pulse within the frame with respect to the reference pulse and $\otimes$ is the convolution operator. The use of signal and reference pulses at non-degenerate central wavelengths enables spectral bandpass filtering of the output light, in order to block background light arising from second harmonic generation by each of the input waves [20]. The space domain image consisting of separated beams can be directly detected [20-22] by an array of photodetectors, resulting in an instantaneous intensity measurement at each time slot within the OTDM frame. Whilst this would be sufficient for detecting an on-off keying (OOK) modulated bit stream, the phase information contained in the quasi-monochromatic SFG light is lost with intensity detection. Here we demonstrate coherent detection of the phase information by homodyne mixing of the SFG output light with a narrowband LO at a balanced detector.

Figure 2 shows our experimental setup. A mode-locked laser (MLL) generates ~100 fs bandwidth-limited pulses at 810 nm with an 80.2 MHz repetition rate. These are converted by an optical parametric oscillator (OPO) to 'signal' pulses at 1550 nm central wavelength (beam path shown in green) and 'reference' pulses at 1697 nm (shown in red). The signal pulse train is directed into an electro-optic phase modulator based on a bulk KTP crystal (New Focus 4064). The phase modulator is driven with a 500 kHz sinusoidally varying high voltage in order to apply positive and negative phase shifts of up to 1.5 radians to the signal pulses. A series of n signal pulses exiting the phase modulator then has the form:

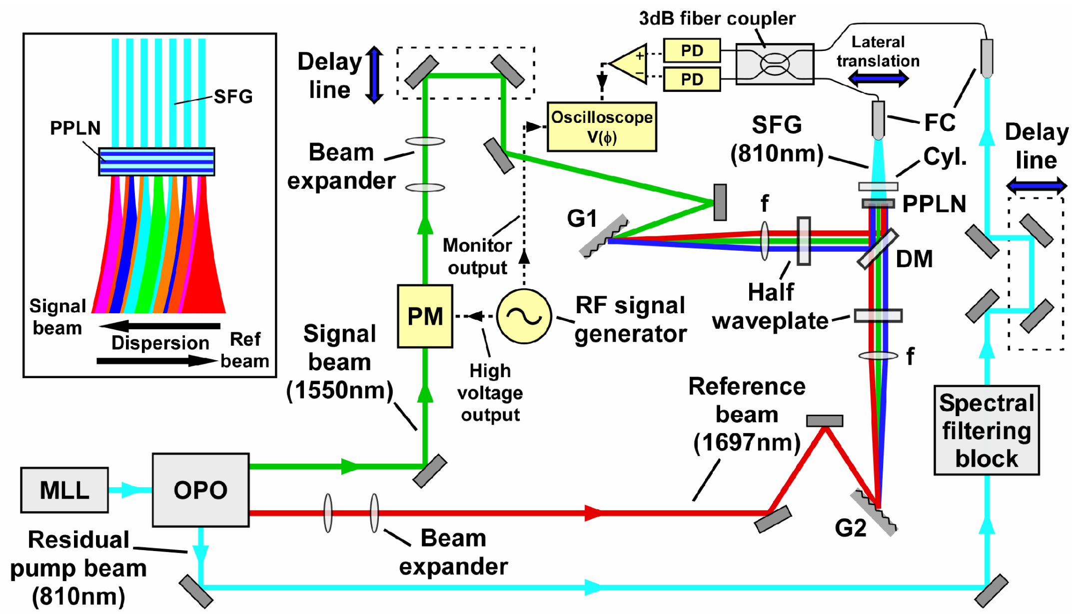

Fig. 2. Experimental setup for time-to-space conversion with coherent detection (MLL, mode-locked laser; OPO, optical parametric oscillator; PM, phase modulator; G1/G2, diffraction grating; f, Fourier lens; DM, dichroic mirror; Cyl., cylindrical lens; FC, fiber collimator; PD, photodetector). Note that the SFG beam fiber collimator can be laterally translated to detect different spatially demultiplexed pulse images. The spectral filtering block represents a diffraction grating – Fourier lens – spatial filter setup. A high voltage amplifier (not shown) was used to amplify the RF signal driving the phase modulator. Dashed lines represent electrical connections. Inset: dispersed signal and reference beams at the PPLN.

$$s(t) = \sum_k p(t - kt_0)\exp(jf_{RF}t) \tag{2}$$

where $p(\bullet)$ is the temporal envelope of the signal pulse located at time kt_0 in the pulse train, k is an integer representing the pulse number, t_0 is the pulse-to-pulse time separation and f_{RF} is the phase modulation frequency. The modulated signal pulse then passes through a delay line in order to adjust its time delay with respect to the reference pulse on arrival at the time-to-space processor.

The signal pulse is then spatially dispersed by a diffraction grating and Fourier lens. At the same time the non-modulated reference pulse is given an equal but opposite spatial dispersion by another diffraction grating and Fourier lens. The two dispersed pulses are superimposed by a dichroic mirror and are incident on a periodically-poled lithium niobate (PPLN) nonlinear crystal located at the focal plane (see inset in Fig. 2). The PPLN crystal has a poling period of 20.3 μm and dimensions of 12 mm and 8 mm in the spatial dispersion direction and light propagation direction, respectively. The Rayleigh length of the focused signal and reference spectral components inside the PPLN was estimated as ~1 mm, by calculating the focused spectral component spot size from measurements of the spectral resolution and spatial dispersion of the light at the Fourier plane.

The signal and reference beams' average powers at the PPLN entrance face were measured as 134 mW and 75 mW respectively, resulting in pulse energies of 1.7 nJ and 0.9 nJ and peak powers of 35 W and 19 W respectively. The spatial extent of the dispersed beams was approximately 4 mm in the horizontal (spatial dispersion) direction and 12 μm in the vertical (focused) direction (both sizes are the $1/e^2$ radius). Ideally the reference pulse peak power would be much higher than that of the signal pulse; however this was not available from the OPO used in this experiment. The peak powers were calculated assuming that the dispersed signal and reference pulses at the Fourier plane were stretched through the time-to-space converter time window, which was measured as 48 ps (FWHM). Phase-matched SFG at each point in space resulted in the generation of sum-frequency light centered at 810 nm with a -3 dB bandwidth of 0.1 nm; the spectrum is shown in Fig. 3 (blue line). The THz bandwidth input sub-picosecond pulses are thereby transferred to a narrowband output SFG wave with an approximately 50 GHz bandwidth, which is within the detection bandwidth of fast optoelectronic detectors. The SFG beam average power emerging from the PPLN was measured as 22 μW.

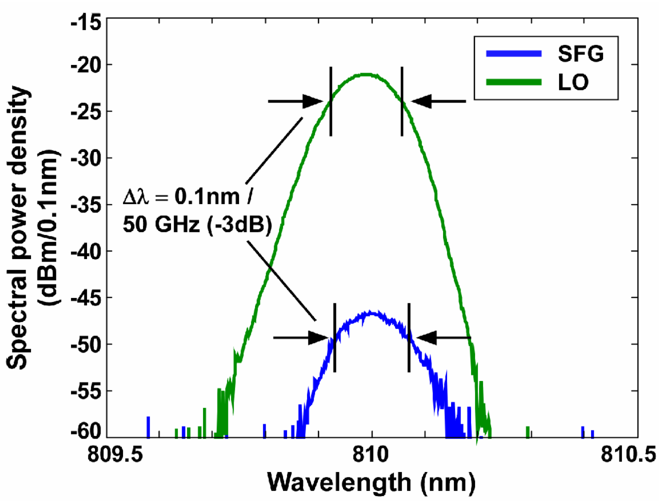

Fig. 3. Time-to-space converted SFG spectrum (blue) and local oscillator spectrum (green). Each spectrum is centered at 810 nm and has a -3dB bandwidth of approximately 0.1 nm (~50 GHz). The measurements were made by alternately coupling the SFG and LO light from one of the -3 dB fiber coupler outputs into an optical spectrum analyzer set to 0.1 nm resolution.

The elliptical SFG beam was collimated in the vertical direction by a cylindrical lens placed after the PPLN, resulting in a more circular beam profile. At the same time the LO beam was generated by spectral filtering of the mode-locked laser residual pump pulse at 810 nm, which exits from the OPO (beam path shown in cyan in Fig. 2). A diffraction grating, Fourier lens and narrow slit (represented by the 'spectral filtering block' in Fig. 2) were used to narrow the -3 dB bandwidth of the residual pump pulse from approximately 9 nm to 0.1 nm to match the SFG spectrum; the LO spectrum is also shown in Fig. 3 (green line). Another delay line was used to obtain temporal overlap of the filtered LO pulse with the SFG pulse at the balanced detector.

The SFG and LO beams were each coupled via fiber collimators into separate single mode fibers (at 810 nm). There was an approximately 9 dB insertion loss of the SFG light into its fiber collimator, due to mode mismatch between the SFG beam and the collimator mode. The SFG and LO light was then mixed in a -3 dB coupler, obtaining different beat measurements at the two output ports of the coupler. The light from each output was then incident on the positive and negative photodiodes of a 350 MHz bandwidth silicon balanced detector (Thorlabs PDB430A-AC). Interference between the SFG and LO light converted the SFG phase modulation into intensity modulation which could be registered by the photodiodes. The SFG and LO optical powers arriving at the balanced detector were individually measured as 0.003 mW and 5 mW respectively. By equalizing the optical power incident on each photodiode the DC component of the summed photocurrents was minimized, leaving the RF sum component whose amplitude was proportional to the SFG and LO optical power and, crucially, to the relative phase between the SFG and LO.

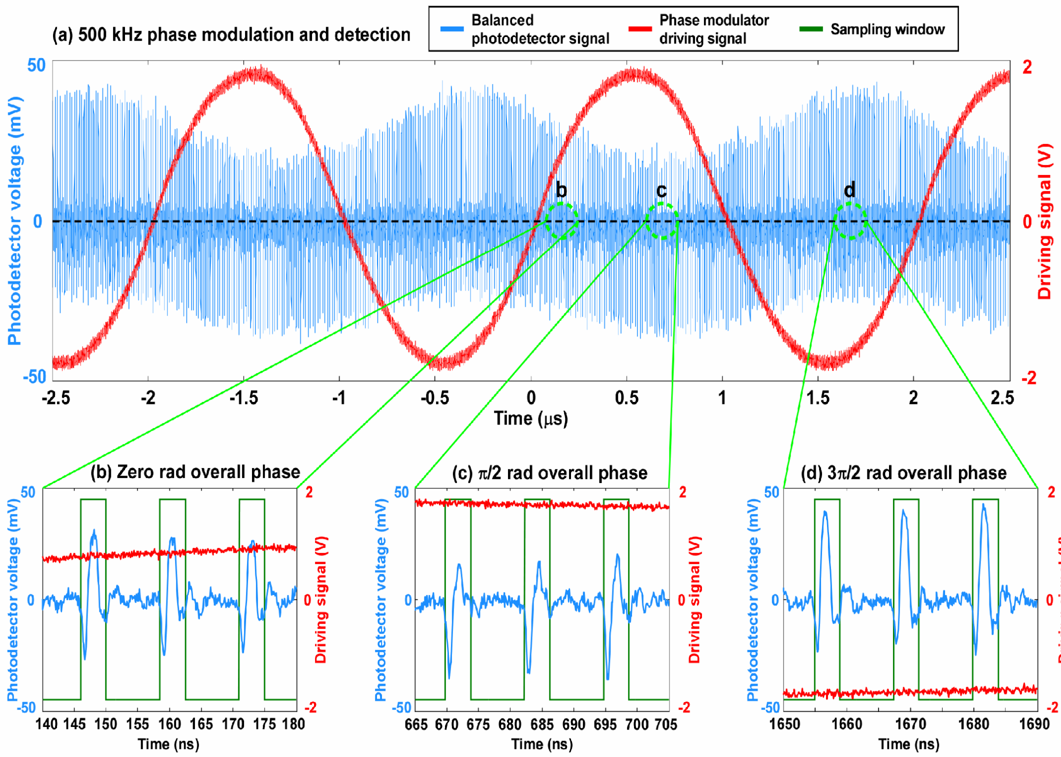

Fig. 4. Coherent detection of time-to-space converted phase modulated pulses. (a) Oscilloscope trace showing the balanced photodetector signal (blue) and the 500 kHz sinusoidal driving signal applied to the phase modulator (red). The phase modulator driving signal shown was taken from the monitor output of the high voltage amplifier which was used to drive the phase modulator. (b), (c) and (d) Close-ups of individual pulses detected at various phases (note the nanosecond time scale). The sampling windows used to derive the data shown in Fig. 5 are represented by green rectangles; the window amplitude varies from zero to one in a square wave fashion. The location on the oscilloscope trace of each close-up is indicated by a green dashed circle in (a). The waveforms seen in (b) are due to ringing by the 350 MHz bandwidth balanced detector, which degrades the quality of the phase-demodulated signal as can be seen in (a). However negative and positive demodulated pulses can clearly be seen in (c) and (d) respectively. Note that due to a residual fixed phase on the LO, there is an offset between the phase modulator driving signal phase and the phase of the received signal.

The RF electrical signal was recorded on a 12 GHz oscilloscope (Agilent DSO 81204A) and an example trace is shown in Fig. 4(a), along with the phase modulator driving signal. A sinusoidal modulation of the SFG pulse train with modulation frequency 500 kHz can also be seen. However, as is evident in Fig. 4(a) and Fig. 4(b), an electrical signal was present at the balanced photodetector RF output even for zero overall phase of the homodyne mixing product. We believe this was due to ringing effects caused by the limited bandwidth of the photodiodes and transimpedance amplifier in the balanced photodetector. Figures 4(b), 4(c) and 4(d) show close-ups of individual pulses taken from the trace in Fig. 4(a) at zero, $\pi/2$ and $3\pi/2$ phases. Figures (c) and (d) provide clear evidence for single-shot coherent detection of negatively and positively phase modulated pulses respectively. A small phase shift between the phase modulator driving signal and the response of the modulated signal as measured on the oscilloscope is also apparent; this is due to a constant phase offset present on the LO wave with respect to the signal. In coherent reception, this phase offset is eliminated by an estimation and DSP.

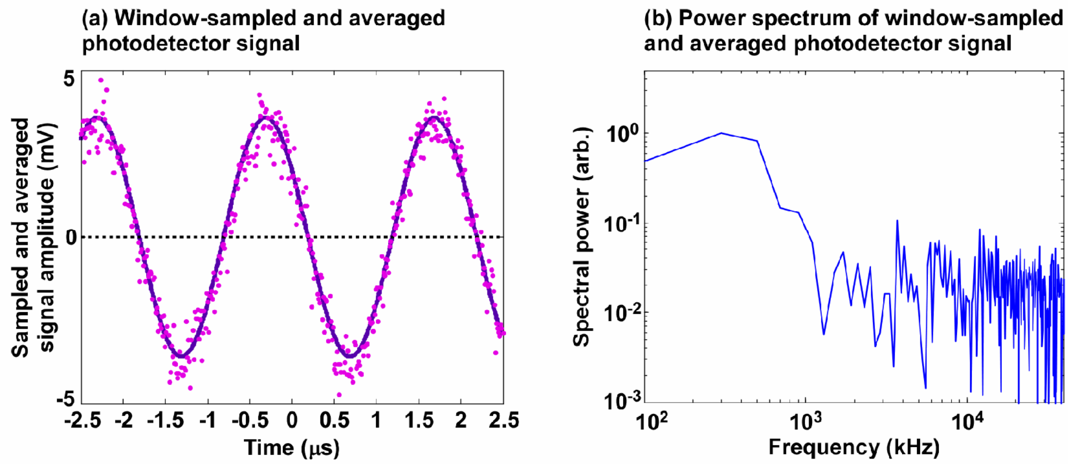

Fig. 5. Time window sampled and averaged photodetector signal. (a) Time domain representation showing the average photovoltage for each pulse (pink dots) with a sine curve fit to the data points (purple line). (b) Frequency domain representation of the sampled signal, found by taking the Fourier transform of the photovoltage data points in (a).

To obtain a clearer phase-demodulated output signal, the oscilloscope trace shown in Fig. 4(a) was sampled to extract the signal component only. The signal was extracted by integrating over a time window matched to the detector response time; the time windows are illustrated by the green rectangles in Figs. 4(b), 4(c) and 4(d). The width of each time window is set to 4 ns to collect the energy over the whole electrical waveform generated by each detected pulse. The electrical signal present within each window results in a single average voltage value for each detected pulse; these are plotted as pink dots in Fig. 5(a).

In order to determine the signal to noise ration (SNR) of the demodulated signal, a sine function was fitted to the sampled data points; this is shown as the purple line in Fig. 5(a). The fit resulted in a root mean squared amplitude and standard deviation of v_{opt} = 2.67 mV and σ_v = 0.53 mV respectively, giving an SNR of $v_{opt}^2 / \sigma_v^2 = 25$. The balanced photodetector noise was calculated as 0.52 mV dominated by LO shot noise, showing that the demodulated signal is shot noise limited by the LO. The power spectrum of the sampled signal, found by taking the Fourier transform of the data points shown in Fig. 5(a), is shown in Fig. 5(b); a peak due to the applied phase modulation can be seen at approximately 500 kHz. Note that the signal modulation depth was limited to ~0.5 due to the maximum 1.5 radians phase modulation applied by the free-space phase modulator; this was in turn restricted by the highest driving voltage (± 200 V) which could be supplied. Had full phase modulation depth been achieved, the SNR would reach 100 since the noise figure would be expected to remain the same. Additionally, the 9 dB insertion loss of the SFG light into the fiber collimator further limited the SNR achieved. Eliminating this loss would result in an approximately factor 3 increase in signal amplitude whilst leaving the LO dominated noise level unaffected, thus giving a factor 9 increase in SNR.

In conclusion we have demonstrated real-time demultiplexing to the spatial domain and single-shot coherent detection of a phase modulated ultrashort pulse train by time-to-space conversion. The inherently narrow linewidth SFG output signal of the time-to-space conversion process enables interferometric detection of phase information originally encoded on ultrashort pulses. This demonstration underlines the potential of time-to-space conversion as an all-optical serial-to-parallel demultiplexer capable of transferring wideband time domain signals to a slowly varying spatial domain image. By bridging the optical-electrical bandwidth gap, time-to-space conversion can be a valuable tool in support of ultrahigh bit rate OTDM optical communications.

References

1. R. Essiambre and R. W. Tkach, "Capacity trends and limits of optical communications networks," Proc. IEEE **100**(5), 1035-1055 (2012).
2. E. M. Ip and J. M. Kahn, "Fiber Impairment Compensation Using Coherent Detection and Digital Signal Processing," J. Lightwave Technol. **28**(4), 502-519 (2010).
3. H. Weber, R. Ludwig, S. Ferber, C. Schmidt-Langhorst, M. Kroh, V. Marembert, C. Boerner, and C. Schubert, "Ultrahigh-Speed OTDM-Transmission Technology," J. Lightwave Technol. **24**(12), 4616-4627 (2006).
4. J. P. Sokoloff, P. R. Prucnal, I. Glesk, and M. Kane, "A Terahertz Optical Asymmetric Demultiplexer (TOAD)," IEEE Photon. Technol. Lett. **5**(7), 787-790 (1993).
5. H. Sotobayashi, C. Sawaguchi, Y. Koyamada, and W. Chujo, "Ultrafast walk-off-free nonlinear optical loop mirror by a simplified configuration for 320-Gbit/s time-division multiplexing signal demultiplexing," Opt. Lett. **27**(17), 1555-1557 (2002).
6. K.I. Kang, I. Glesk, T.G. Chang, P.R. Prucnal and R.K. Boncek, "Demonstration of all-optical Mach-Zehnder demultiplexer," Opt. Lett. **31**(9), 749-750 (1995).
7. T. Miyazaki and F. Kubota, “Simultaneous Demultiplexing and Clock Recovery for 160-Gb/s OTDM Signal Using a Symmetric Mach-Zehnder Switch in Electrooptic Feedback Loop,” IEEE Photon. Technol. Lett. **15**(7), 1008-1100 (2003).
8. K.-Y. Wang, K. G. Petrillo, M. A. Foster, and A. C. Foster, “Ultralow-power all-optical processing of high speed data signals in deposited silicon waveguides,” Opt. Exp. **20**(22), 24600-24606 (2012).
9. T. D. Vo, H. Hu, M. Galili, E. Palushani, J. Xu, L. K. Oxenløwe, S. J. Madden, D.-Y. Choi, D. A. P. Bulla, M. D. Pelusi, J. Schröder, B. Luther-Davies, and B. J. Eggleton, “Photonic chip based transmitter optimization and receiver demultiplexing of a 1.28 Tbit/s OTDM signal,” Opt. Exp. **18**(16), 17252-17261 (2010).
10. J. K. Fischer, R. Ludwig, L. Molle, C. Schmidt-Langhorst, A. Galperin, T. Richter, C. C. Leonhardt, A. Matiss, C. Schubert, “High-speed digital coherent based on parallel optical sampling,” J. Lightwave Technol. **29**(4), 378-385 (2011).
11. M. T. Kauffman, W. C. Banyai, A. A. Godil, and D. M. Bloom, "Time-to-frequency converter for measuring picosecond optical pulses," Appl. Phys. Lett. **64**(3), 270-272 (1994).
12. E. Palushani, H. C. Mulvad, M. Galili, H. Hu, L. K. Oxenløwe, A. T. Clausen, and P. Jeppesen, "OTDM-to-WDM Conversion Based on Time-to-Frequency Mapping by Time-Domain Optical Fourier Transformation," IEEE J. Sel. Top. Quantum Electron. **18**(2), 681-688 (2012).
13. Y. T. Mazurenko, S. E. Putilin, A. G. Spiro, A. G. Beliaev, V. E. Yashin, and S. A. Chizhov, “Ultrafast time-to-space conversion of phase by the method of spectral nonlinear optics,” Opt. Lett. **21**(21), 1753-1755 (1996).
14. P. C. Sun, Y. T. Mazurenko, and Y. Fainman, “Femtosecond pulse imaging: ultrafast optical oscilloscope,” J. Opt. Soc. Am. A **14**(5), 1159-1170 (1997).
15. A. M. Kan'an and A. M. Weiner, “Efficient time-to-space conversion of femtosecond optical pulses,” J. Opt. Soc. Am. B **15**(3), 1242-1245 (1998).
16. D. M. Marom, D. Panasenko, P. -C. Sun, and Y. Fainman, “Linear and nonlinear operation of a time-to-space processor,” J. Opt. Soc. Am. A **18**(2), 448-458 (2001).
17. D. M. Marom, D. Panasenko, P. -C. Sun, Y. T. Mazurenko and Y. Fainman, “Real-time spatial–temporal signal processing with optical nonlinearities,” IEEE J. Sel. Top. Quantum Electron. **7**(4), 683-693 (2001).
18. J.-H. Chung and A. M. Weiner, “Real-time detection of femtosecond optical pulse sequences via time-to-space conversion in the lightwave communications band,” J. Lightwave Technol. **21**(12), 3323–3333 (2003).
19. A. M. Weiner, “Femtosecond pulse shaping using spatial light modulators,” Rev. Sci. Instrum. **71**(5), 1929-1960 (2000).
20. D. Shayovitz and D. M. Marom, “High-resolution, background-free, time-to-space conversion by collinearly phase-matched sum-frequency generation,” Opt. Lett. **36**(11), 1957–1959 (2011).
21. D. Shayovitz, H. Herrmann, W. Sohler, R. Ricken, C. Silberhorn, and D. M. Marom, “High resolution time-to-space conversion of sub-picosecond pulses at 1.55µm by non-degenerate SFG in PPLN crystal,” Opt. Exp. **20**(24), 27388-27395 (2012).
22. D. Shayovitz, H. Herrmann, W. Sohler, R. Ricken, C. Silberhorn, and D. M. Marom, “Time-to-space conversion of ultrafast waveforms at 1.55µm in a planar periodically poled lithium niobate waveguide,” Opt. Lett. **38**(22), 4708-4711 (2013).
23. D. Shayovitz, H. Herrmann, W. Sohler, R. Ricken, C. Silberhorn, and D. M. Marom, “Full-field reconstruction of ultrashort waveforms by time to space conversion interferogram analysis,” Opt. Exp. **22**(17), 20205-20213 (2014).

Chapter 5: Summary and future directions

This thesis presented research on time-to-space conversion of ultrafast optical signals and its applications in optical communications and ultrashort pulse measurement. By combining the effectively instantaneous response time of nonlinear optical gating with the high spectral resolution of broadband spectral processing techniques, time-to-space conversion transfers information from the difficult to measure time domain to the spatial domain, where it can be measured with high resolution. This technique can be used to perform serial-to-parallel demultiplexing of a high bit rate OTDM channel or to perform full-field measurement for complete characterisation of ultrashort pulses.

The main aims of the project were: a) to develop time-to-space conversion as a practical technique for OTDM demultiplexing and b) to demonstrate proof of principle for full-field measurement of ultrashort optical waveforms. In order to achieve aim (a) collinearly phase-matched, non-degenerate, background-free and high resolution time-to-space conversion was demonstrated, as a necessary condition for implementing time-to-space conversion in the guided-wave regime. In addition, time-to-space conversion in a planar nonlinear waveguide was implemented, resulting in an increase in conversion efficiency slope compared to the case for bulk nonlinear crystal. Real time demodulation of phase information, a prerequisite for compatibility with optical communications advanced modulation formats, was demonstrated by homodyne coherent detection of a time-to-space converted phase-modulated ultrashort pulse train. Aim (b) was achieved by performing amplitude and phase measurements of linearly phase-modulated pulse packets and of bandwidth-limited and frequency chirped ultrashort pulses.

Further development of the time-to-space conversion technique into a practical solution to OTDM demultiplexing will require transfer of all the optical functionalities of the time-to-space processor from free-space to the guided-wave regime. Having demonstrated time-to-space conversion in a planar nonlinear waveguide, the next step would be to fabricate an array of long waveguides in PPLN, in order to fully confine the SFG interactions between the dispersed signal and reference pulses (see Fig. 6.1). This should result in a large increase in conversion efficiency, finally bringing down the time-to-space conversion optical power requirements to the mW average power level. The length of the waveguides will be determined by a combination of factors including optimum conversion efficiency, pump (reference beam) depletion and deleterious spectral filtering effects due to temporal walkoff. The number of waveguides in the array will be around 100, determined by the required spectral resolution (time window extent) and by fabrication constraints in achieving a high degree of optical uniformity across the array.

Integrated together with the PPLN waveguide array will be planar lightwave circuit components designed to perform the other optical functionalities of the time-to-space processor. Currently the spatial dispersion of the signal and reference pulses and the spatial Fourier transform of the light before and after the nonlinear crystal are performed by bulk diffraction gratings and lenses respectively. For the guided-wave time-to-space processor the diffraction gratings will be replaced by arrayed waveguide gratings and the bulk Fourier lenses by slab lenses. Integration of the time-to-space processor onto a single chip will potentially allow its deployment from the research laboratory environment to actual use as part of a high speed optical communications network.

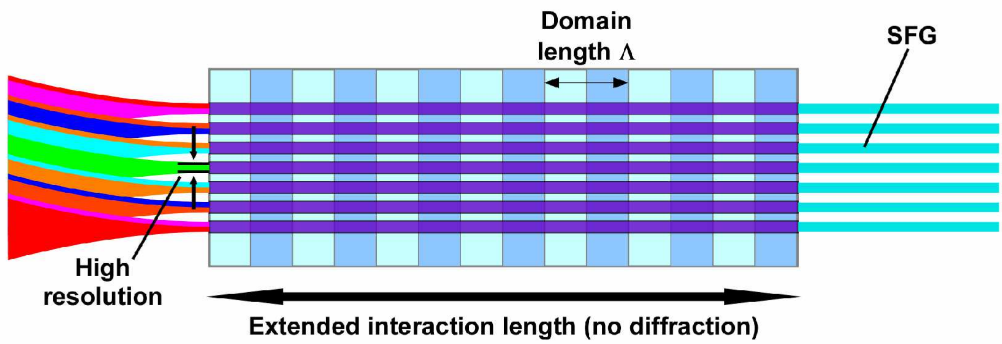

Fig. 5.1: Schematic illustration of time-to-space conversion in an array of PPLN waveguides. Each pair of signal and reference pulse frequency components is fully confined in a separate waveguide and so SFG light is generated all along the waveguide length, resulting in a large increase in conversion efficiency.

Bibliography

The following references refer to the general introduction (Chapter 1) and the individual chapter introductions. Each article included in the thesis is followed by its own references.

1. C. V. Shank and E. P. Ippen, "Subpicosecond kilowatt pulses from a mode-locked cw dye laser," Appl. Phys. Lett. **24**(8), 373-375 (1974).
2. K. Zhao, Q. Zhang, M. Chini, Y. Wu, X. Wang, and Z. Chang, "Tailoring a 67 attosecond pulse through advantageous phase-mismatch," Opt. Lett. **37**(18), 3891-3893 (2012).
3. A. Zewail, "Femtochemistry. Past, present and, future," Pure Appl. Chem. **72**(12), 2219-2231 (2000).
4. C. I. Blaga, J. Xu, A. D. DiChiara, E. Sistrunk, K. Zhang, P. Agostini, T. A. Miller, L. F. DiMauro and C. D. Lin, "Imaging ultrafast molecular dynamics with laser induced electron diffraction," Nature **483**, 194-197 (2012).
5. R. S. Pillai, C. Boudoux, G. Labroille, N. Olivier, I. Veilleux, E. Farge, M. Joffre, and E. Beaurepaire, "Multiplexed two-photon microscopy of dynamic biological samples with shaped broadband pulses," Opt. Exp. **17**(15), 12741-12752 (2009).
6. T. Udem, R. Holzwarth, and T. W. Hänsch, "Optical frequency metrology," Nature **416**, 233–237 (2002).
7. T. Richter, E. Palushani, C. Schmidt-Langhorst, R. Ludwig, L. Molle, M. Nölle, and C. Schubert, "Transmission of single-channel 16-QAM data signals at terabaud symbol rates," J. Lightwave Technol. **30**(4), 504-511 (2012).
8. W. Ng, T. D. Rockwood, G. A. Sefler, and G. C. Valley, "Demonstration of a large stretch-ratio (M=41) photonic analog-to-digital converter with 8 ENOB for an input signal bandwidth of 10 GHz," IEEE J. Photon. Technol. Lett. **24**(14), 1185-1187 (2012).
9. D. Stevenson, B. Agate, X. Tsampoula, P. Fischer, C. T. A. Brown, W. Sibbett, A. Riches, F. Gunn-Moore, and K. Dholakia, "Femtosecond optical transfection of cells: viability and efficiency," Opt. Exp. **14**(16), 7125–7133 (2006).
10. P. A. Franken, A. E. Hill, C. W. Peters, and G. Weinreich, "Generation of optical harmonics," Phys. Rev. Lett. **7**(4), 118–119 (1961).
11. R. W. Boyd, *Nonlinear Optics*, 3rd ed. (Academic Press, 2008).

12. A. M. Weiner, “Femtosecond pulse shaping using spatial light modulators,” Rev. Sci. Instrum. **71**(5), 1929-1960 (2000).
13. Y. T. Mazurenko, S. E. Putilin, A. G. Spiro, A. G. Beliaev, V. E. Yashin, and S. A. Chizhov, “Ultrafast time-to-space conversion of phase by the method of spectral nonlinear optics,” Opt. Lett. **21**(21), 1753-1755 (1996).
14. P. C. Sun, Y. T. Mazurenko, and Y. Fainman, “Femtosecond pulse imaging: ultrafast optical oscilloscope,” J. Opt. Soc. Am. A **14**, 1159-1170 (1997).
15. A. M. Kan'an and A. M. Weiner, “Efficient time-to-space conversion of femtosecond optical pulses,” J. Opt. Soc. Am. B **15**, 1242-1245 (1998).
16. D. M. Marom, D. Panasenko, P. -C. Sun, and Y. Fainman, “Linear and nonlinear operation of a time-to-space processor,” J. Opt. Soc. Am. A **18**, 448-458 (2001).
17. D. M. Marom, D. Panasenko, P. -C. Sun, Y. T. Mazurenko and Y. Fainman, “Real-time spatial–temporal signal processing with optical nonlinearities,” IEEE J. Sel. Top. Quantum Electron. **7**(4), 683-693 (2001).
18. J.-H. Chung and A. M. Weiner, “Real-time detection of femtosecond optical pulse sequences via time-to-space conversion in the lightwave communications band,” J. Lightwave Technol. **21**(12), 3323–3333 (2003).
19. R. Essiambre and R. W. Tkach, "Capacity trends and limits of optical communications networks," Proc. IEEE **100**(5), 1035-1055 (2012).
20. P. Wizner and R. Essiambre, "Advanced optical modulation formats," Proc. IEEE **94**(5), 952-985 (2006).
21. H. Hu, F. Ye, A. K. Medhin, P. Guan, H. Takara, Y. Miyamoto, H.C.H. Mulvad, M. Galili, T. Morioka and L. K. Oxenløwe, " Single Source 5-dimensional (Space, Wavelength-, Time-, Polarization-, Quadrature-) 43 Tbit/s Data Transmission of 6 SDM × 6 WDM × 1.2 Tbit/s Nyquist-OTDM-PDM-QPSK," in *CLEO: 2014*, OSA Technical Digest (online) (Optical Society of America, 2014), paper JTh5B.10.
22. G. Valley, "Photonic analog-to-digital converters," Opt. Exp. **15**(5), 1955-1982 (2007).
23. D. Sinefeld, D. Shayovitz, O. Golani, and D. M. Marom, "Tunable WDM sampling pulse streams using a spatial phase modulator in a biased pulse shaper," Opt. Lett. **39**(3), 642-645 (2014).

24. E. M. Ip and J. M. Kahn, "Fiber Impairment Compensation Using Coherent Detection and Digital Signal Processing," J. Lightwave Technol. **28**(4), 502-519 (2010).

25. J. P. Sokoloff, P. R. Prucnal, I. Glesk, and M. Kane, "A Terahertz Optical Asymmetric Demultiplexer (TOAD)," IEEE Photon. Technol. Lett. **5**(7), 787-790 (1993).

26. H. Sotobayashi, C. Sawaguchi, Y. Koyamada, and W. Chujo, "Ultrafast walk-off-free nonlinear optical loop mirror by a simplified configuration for 320-Gbit/s time-division multiplexing signal demultiplexing," Opt. Lett. **27**(17), 1555-1557 (2002).

27. K.I. Kang, I. Glesk, T.G. Chang, P.R. Prucnal and R.K. Boncek, "Demonstration of all-optical Mach-Zehnder demultiplexer," Opt. Lett. **31**(9), 749-750 (1995).

28. T. Miyazaki and F. Kubota, “Simultaneous Demultiplexing and Clock Recovery for 160-Gb/s OTDM Signal Using a Symmetric Mach-Zehnder Switch in Electrooptic Feedback Loop,” IEEE Photon. Technol. Lett. **15**(7), 1008-1100 (2003).

29. K.-Y. Wang, K. G. Petrillo, M. A. Foster, and A. C. Foster, “Ultralow-power all-optical processing of high speed data signals in deposited silicon waveguides,” Opt. Exp. **20**(22), 24600-24606 (2012).

30. T. D. Vo, H. Hu, M. Galili, E. Palushani, J. Xu, L. K. Oxenløwe, S. J. Madden, D.-Y. Choi, D. A. P. Bulla, M. D. Pelusi, J. Schröder, B. Luther-Davies, and B. J. Eggleton, “Photonic chip based transmitter optimization and receiver demultiplexing of a 1.28 Tbit/s OTDM signal,” Opt. Exp. **18**(16), 17252-17261 (2010).

31. H. C. H. Mulvad, M. Galili, L. K. Oxenløwe, H. Hu, A. T. Clausen, J. B. Jensen, C.Peucheret, and P. Jeppesen, "Demonstration of 5.1 Tbit/s data capacity on a single-wavelength channel," Opt. Exp. **18**(2), 1438-1443 (2010).

32. M. T. Kauffman, W. C. Banyai, A. A. Godil, and D. M. Bloom, "Time-to-frequency converter for measuring picosecond optical pulses," Appl. Phys. Lett. **64**(3), 270-272 (1994).

33. E. Palushani, H. C. Mulvad, M. Galili, H. Hu, L. K. Oxenløwe, A. T. Clausen, and P. Jeppesen, "OTDM-to-WDM Conversion Based on Time-to-Frequency

Mapping by Time-Domain Optical Fourier Transformation," IEEE J. Sel. Top. Quantum Electron. **18**(2), 681-688 (2012).

34. L. Chuntonov, A. Fleischer and Z. Amitay, “Weak-field multiphoton femtosecond coherent control in the single-cycle regime,” Opt. Exp. **19**(7), 6865-6882 (2011).
35. R. Bartels, S. Backus, E. Zeek, L. Misoguti, G. Vdovin, I. P. Christov, M. M. Murnane and H. C. Kapetyn, “Shaped-pulse optimization of coherent emission of high-harmonic soft x-rays,” Nat. **406**, 164-166 (2000).
36. D. J. Kane and R. Trebino, “Single-shot measurement of the intensity and phase of an arbitrary ultrashort pulse by using frequency-resolved optical gating,” Opt. Lett. **18**(10), 823-825 (1993).
37. D. J. Kane, R. Trebino, K. W. DeLong, D. N. Fittinghoff, J. N. Sweetser, M. A. Krumbugel, and B. A. Richman, “Measuring ultrashort laser pulses in the time-frequency domain using frequency-resolved optical gating,” Rev. Sci. Instrum. **68**(9), 3277-3295 (1997).
38. L. Xu, E. Zeek, and R. Trebino, “Simulations of frequency-resolved optical gating for measuring very complex pulses,” J. Opt. Soc. Am. B **25**, 70-80 (2008).
39. P. O’Shea, M. Kimmel, X. Gu, and R. Trebino, “Highly simplified device for ultrashort-pulse measurement,” Opt. Lett. **26**(12), 932-934 (2001).
40. D. Meshulach, D. Yelin, and Y. Silberberg, “Real-time spatial–spectral interference measurements of ultrashort optical pulses,” J.Opt. Soc. Am. B **14**(8), 2095-2098 (1997).
41. C. Iaconis and I. A. Walmsley, “Spectral phase interferometry for direct electric-field reconstruction of ultrashort optical pulses,” Opt. Lett. **23**(10), 792-794 (1998).
42. P. Bowlan, P. Gabolde, A. Shreenath, K. McGresham, S. Akturk and R. Trebino, “Crossed-beam spectral interferometry: a simple, high-spectral-resolution method for completely characterizing complex ultrashort pulses in real time,” Opt. Exp. **14**(24), 11892-11900 (2006).
43. B. H. Kolner, “Space-Time Duality and the Theory of Temporal Imaging,” IEEE J. Quant. Electron. **30**(8), 1951-1963 (1994).
44. M. T. Kauffman, W. C. Banyai, A. A. Godil, and D. M. Bloom, “Time-to-frequency converter for measuring picosecond optical pulses,” Appl. Phys. Lett. **64**, 270-272 (1994).

45. M. A. Foster, R. Salem, D. F. Geraghty, A. C. Turner-Foster, M. Lipson and A. L. Gaeta, "Silicon-chip-based ultrafast optical oscilloscope," Nat. Photon. **456**, 81-85 (2008).
46. C. Dorrer, "Single-shot measurement of the electric field of optical waveforms by use of time magnification and heterodyning," Opt. Lett. **31**(4), 540-542 (2006).
47. N. K. Fontaine, R. P. Scott, L. Zhou, F. M. Soares, J. P. Heritage and S. J. B. Yoo, "Real-time full-field arbitrary optical waveform measurement," Nat. Photon. **4**, 248-254 (2010).
48. R. C. Eckardt, H. Masuda, Y. X. Fan, and R. L. Byer, "Absolute and Relative Nonlinear Optical Coefficients of KDP, KD*P, BaB_2O_4, LiO_3, MgO:$LiNbO_3$, and KTP Measured by Phase-Matched Second-Harmonic Generation," IEEE J. Quantum Electron. **26**(5), 922–933 (1990).
49. I. Shoji, T. Kondo, A. Kitamoto, M. Shirane, and R. Ito, "Absolute scale of second-order nonlinear-optical coefficients," J. Opt. Soc. Am. B **14**(9), 2268–2294 (1997).
50. D. Sinefeld, S. Ben-Ezra, C. R. Doerr, and D. M. Marom, "All-channel tunable optical dispersion compensator based on linear translation of a waveguide grating router," Opt. Lett. **36**(8), 1410-1412 (2011).
51. G. P. Agrawal, *Fiber-Optic Communications Systems*, 3rd ed. (John Wiley & Sons, 2002).

המרת זמן-מרחב עם רזולוציה ויעילות גבוהות של אותות מהירים

חיבור לשם קבלת תואר דוקטור לפילוסיפיה

מאת

דרור שיוביץ

הוגש לסנט האוניברסיטה העברית בירושלים

ספטמבר / 2014

המרת זמן-מרחב עם רזולוציה ויעילות גבוהות של אותות מהירים

חיבור לשם קבלת תואר דוקטור לפילוסיפיה

מאת

דרור שיוביץ

הוגש לסנט האוניברסיטה העברית בירושלים

ספטמבר / 2014

עבודה זו נעשתה בהדרכתו של:

דן מ. מרום

תקציר

פולסים אופטיים אולטרה-קצרים מצויים בשימוש נרחב בתחומים רבים ומגוונים במדעים ובטכנולוגיה. הודות לרזולוציה הזמנית הגבוהה שהם מספקים, פולסים קצרים מאפשרים חקר ומדידה של תופעות פיסיקליות, כימיות וביולוגיות יסודיות אשר מתרחשות על סקלות זמן של פיקו-שניות ופחות. בנוסף, פולסים אולטרה-קצרים מהווים כלי חיוני בתחומי התקשורת האופטית המהירה וטכנולוגיות לעיבוד אינפורמציה, כמו כן בייצור תעשייתי מתקדם ובפוטו-רפואה. בכל התחומים האלה מדידה ושליטה מדויקת על פולסים אופטיים אולטרה-קצרים היא עניין קריטי – התקדמות ביצירת פולסים עוד יותר קצרים חייבת להילווה בשיטות מדידה ושליטה חדשות.

מוגשת בתיזה הזאת עבודה על הפיתוח המתמשך של שיטת מדידה ושליטה על פולסים אולטרה-קצרים הקרויה המרת זמן-מרחב. שיטת המרת זמן-מרחב מבוססת על יצירת סכום-תדרים בין פולסים אולטרה-קצרים מפורקים ספקטראלית על מנת להעביר אינפורמציה מתחום הזמן לתחום המרחב, כלומר ליצור הדמייה מרחבית של פולס אולטרה-קצר. מיפוי מעטפת העוצמה והפאזה הזמנית של הפולס להדמייה מרחבית חצי-סטאטית מאפשר מדידה רזולוטיבית של הכמויות האלה ובכך מתגבר על הקושי הכרוך בגילוי אלקטרו-אופטי של פולסים אולטרה-קצרים בתחום הזמן. יתר על כן, האופי המפורק-ספקטאלית של המרת זמן-מרחב גורם לחלון ביצועים זמני רחב. תכונה זו מאפשרת העברה בו-זמנית של סידרת פולסים אולטרה-קצרים ליעדים נפרדים במרחב דרך אינטרקציה עם פולס ייחוס יחיד, מה שמהווה פעולת אי-ריבוב אופטי.

שני הפיתוחים העיקריים המוצגים בתיזה הם: א) ישימות מוגברת של שיטת המרת זמן-מרחב בתחום אי-ריבוב אופטי של ערוץ תקשורת אופטית מהירה על ידי הדגמת השיטה במוליך גל משטחי ולא ליניארי ו-ב) הדגמת איפיון שדה שלם (אמפליטודה ופאזה) של פולסים אולטרה-קצרים על ידי גילוי קוהרנטי אחרי המרת זמן-מרחב. יישומיות שיטת המרת זמן-מרחב לאי-ריבוב אופטי תלוייה בהפחתת צריכת העוצמה האופטית שלה. ניתן לעשות זאת על ידי ביצוע תהליך ההמרה עם גלים מונחים, בניגוד לשיטת תווך-חופשי אשר שימשה בעבר להמרת זמן-מרחב. שלושת המאמרים הראשונים בתיזה מתארים את הצעדים הראשונים לקראת המטרה הזאת, שהם הדגמת המרת זמן-מרחב ללא אור רקע עם אורכי גלים בלתי זהים ועם התאמת פאזה של אלומות המתקדמות יחדיו וגם הדגמת המרת זמן-מרחב בתוך מוליך גל משטחי ולא-ליניארי. איפיון שדה שלם של פולסים אולטרה-קצרים מתאפשר בגלל צרות הסרט הספקטראלי של אות סכום-התדרים שיוצא, תכונה שהיא עובדה יוצאת של הגיאומטריה הייחודית של גלי הפולס הנמדד ופולס הייחוס המפורקים ספקטראלית בכיוונים הפוכים. אפשר לערבב את האות צר הסרט עם אוסילטור מקומי שהוא גם צר סרט, וכך לבצע מדידה אינטרפרומטרית של האמפליטודה והפאזה של הפולס האולטרה-קצר. מתואר בשני המאמרים הסופיים המוגשים כאן הדגמת מדידת שדה שלם של פולסים עם שיפוע תדר ליניארי על ידי המרת זמן-מרחב וגילוי קוהרנטי רגעי של רכבת פולסים אולטרה-קצרים עם מודולציית פאזה. במבט כולל, העבודה המוגשת בתיזה הזאת השיגה עלייה בשימושיות של המרת זמן-

מרחב בתור טכניקת מדידה ושליטה על פולסים אופטיים אולטרה-קצרים, עם יישומים אפשריים בתקשורת אופטית ועיבוד אינפורמצייה וגם בתחום מדידת פולסים אולטרה-קצרים.